MINISTÉRIO DA CIÊNCIA, TECNOLOGIA E INOVAÇÃO
INSTITUTO NACIONAL DE PESQUISAS ESPACIAIS

sid.inpe.br/mtc-m21d/2023/02.22.19.12-TDI

IMPLEMENTATION OF SIMULATION PROBE AND ANALYSIS ON THE ELECTRODYNAMICS COUPLING MODELLING BETWEEN THE SOLAR WIND AND THE EARTH'S MAGNETOSPHERE: TWO MAGNETOHYDRODYNAMICS TYPIC CASES

Randall Hell Vargas Pradinett

Master's Dissertation of the Graduate Course in Space Geophysics, guided by Drs. Odim Mendes Junior, and Müller Moreira Souza Lopes, approved in February 16, 2023.

URL of the original document:
<http://urlib.net/8JMKD3MGP3W34T/48JPBN2>

INPE
São José dos Campos
2023

PUBLISHED BY:

Instituto Nacional de Pesquisas Espaciais - INPE
Coordenação de Ensino, Pesquisa e Extensão (COEPE)
Divisão de Biblioteca (DIBIB)
CEP 12.227-010
São José dos Campos - SP - Brasil
Tel.:(012) 3208-6923/7348
E-mail: pubtc@inpe.br

MINISTÉRIO DA CIÊNCIA, TECNOLOGIA E INOVAÇÃO
INSTITUTO NACIONAL DE PESQUISAS ESPACIAIS

sid.inpe.br/mtc-m21d/2023/02.22.19.12-TDI

IMPLEMENTATION OF SIMULATION PROBE AND ANALYSIS ON THE ELECTRODYNAMICS COUPLING MODELLING BETWEEN THE SOLAR WIND AND THE EARTH'S MAGNETOSPHERE: TWO MAGNETOHYDRODYNAMICS TYPIC CASES

Randall Hell Vargas Pradinett

Master's Dissertation of the Graduate Course in Space Geophysics, guided by Drs. Odim Mendes Junior, and Müller Moreira Souza Lopes, approved in February 16, 2023.

URL of the original document:
<http://urlib.net/8JMKD3MGP3W34T/48JPBN2>

INPE
São José dos Campos
2023

Cataloging in Publication Data

Pradinett, Randall Hell Vargas.

P882i Implementation of simulation probe and analysis on the electrodynamics coupling modelling between the solar wind and the Earth's magnetosphere: two magnetohydrodynamics typic cases / Randall Hell Vargas Pradinett. – São José dos Campos : INPE, 2023.

xxvi + 105 p. ; (sid.inpe.br/mtc-m21d/2023/02.22.19.12-TDI)

Dissertation (Master in Space Geophysics) – Instituto Nacional de Pesquisas Espaciais, São José dos Campos, 2023.

Guiding : Drs. Odim Mendes Junior, and Müller Moreira Souza Lopes.

1. Magnetohydrodynamics. 2. Geomagnetic disturbance regimes. 3. HILDCAA. 4. Adaptive mesh refinement. 5. Simulation probe. I.Title.

CDU 550.3:537.84

MINISTÉRIO DA CIÊNCIA, TECNOLOGIA E INOVAÇÕES

INSTITUTO NACIONAL DE PESQUISAS ESPACIAIS
Serviço de Pós-Graduação - SEPGR

DEFESA FINAL DE DISSERTAÇÃO DE RANDALL HELL VARGAS PRADINETT REG. 199307/2020, BANCA Nº 010/2023

No dia 16 de fevereiro de 2023, por teleconferência, o(a) aluno(a) mencionado(a) acima defendeu seu trabalho final (apresentação oral seguida de arguição) perante uma Banca Examinadora, cujos membros estão listados abaixo. O(A) aluno(a) foi APROVADO(A) pela Banca Examinadora, por unanimidade, em cumprimento ao requisito exigido para obtenção do Título de Mestre em Geofísica Espacial/Ciências do Ambiente Solar-Terrestre, com a exigência de que o trabalho final a ser publicado deverá incorporar as correções sugeridas pela Banca Examinadora, com revisão pelo(s) orientador(es).

Título: "Implementation of simulation probe and analysis on the electrodynamics coupling modelling between the solar wind and the Earth's magnetosphere: two magnetohydrodynamics typic cases."

Membros da banca:

Dr. Marlos Rockenbach da Silva – Presidente – INPE
Dr. Odim Mendes Junior – Orientador – INPE
Dr. Müller Moreira Souza Lopes – Orientador – UNESP/Presidente Prudente
Dr. Andrés Reinaldo Rodriguez Papa – Membro Externo – Observatório Nacional - RJ

Documento assinado eletronicamente por **Odim Mendes Júnior**, **Pesquisador**, em 17/02/2023, às 15:45 (horário oficial de Brasília), com fundamento no § 3º do art. 4º do Decreto nº 10.543, de 13 de novembro de 2020.

Documento assinado eletronicamente por **Marlos Rockenbach da Silva**, **Pesquisador**, em 17/02/2023, às 16:03 (horário oficial de Brasília), com fundamento no § 3º do art. 4º do Decreto nº 10.543, de 13 de novembro de 2020.

Documento assinado eletronicamente por **Andrés Reinaldo Rodriguez Papa**, **Coordenador de Geofísica**, em 24/02/2023, às 09:33 (horário oficial de Brasília), com fundamento no § 3º do art. 4º do Decreto nº 10.543, de 13 de novembro de 2020.

Documento assinado eletronicamente por **Muller MoReira souza lopes (E)**, **Usuário Externo**, em 28/02/2023, às 09:36 (horário oficial de Brasília), com fundamento no § 3º do art. 4º do Decreto nº 10.543, de 13 de novembro de 2020.

A autenticidade deste documento pode ser conferida no site https://sei.mcti.gov.br/verifica.html, informando o código verificador **10793883** e o código CRC **9D1EA26B**.

Referência: Processo nº 01340.000805/2023-60 SEI nº 10793883

Once we accept our limits, we go beyond them.

ALBERT EINSTEIN

*To my parents **Hell** and **Elisa** for their teaching and unconditional support*

ACKNOWLEDGEMENTS

I thank the National Institute for Space Research (INPE) and the Graduation program in Space Geophysics (GES) for the necessary structure and facilities to accomplish this work.

This thesis was supported by CNPq (Master's scholarship, process number 130925/2020-9), a financial agency to whom I thank.

I thank my supervisors, Dr. Odim Mendes and Dr. Müller Moreira, for suggesting and planning this project and for the many fruitful scientific discussions, suggestions, opportunities, material, and patience that allowed this work to be developed.

I thank Dr. Ralf Deiterding and Dr. Margarete Oliveira Domingues, the principal AMROC-framework coordinators, for the access, permission to contribute, and use of AMROC, mainly MHD resources.

I thank the projects developed by INPE concerning the Processes SEI 01340.003098/20221-00 (TAP 7608799), coordinated by Dr. Odim, DIHPA/CGCE, and SEI 01340.003199/2021-72 (TAP 8605363), coordinated by Dr. Margarete, COPDT/CGPI, which rules the institutional work that provides bases to my dissertation.

I also thank the referred responsible teams and data available from the international repositories (World Data Center-C, Tokyo: https://wdc.kugi.kyoto-u.ac.jp/wdc/Sec3.html; and OMNI Web Service, NASA: https://omniweb.gsfc.nasa.gov/form/omni_min.html).

ABSTRACT

Physical structure researches related to the space sciences presents several challenges due to an extensive range of phenomena. Particularly for Space Weather programs, magnetohydrodynamics modellings are expected to simulate magnetosphere phenomena driven by the interplanetary medium conditions, mainly characterizing those electrodynamics phenomena that can interfere with or even damage infrastructures and services to society. As the main goal, this work aims to analyze the solar wind-magnetosphere electrodynamics coupling under a geomagnetically moderate to the weak regime during HILDCAAs events. Such physical conditions characterize a challenge for simulations due to subtle features existing in the processes. Developed by the INPE team, the magnetohydrodynamics code of the AMROC framework will be used as the modelling tool. For this study, also contributing to code improvement, a probe resource in two and three dimensions has been developed and implemented. The efforts aim to take advantage of the framework characteristics, such as the based-wavelet adaptive mesh refinement and an implemented free divergence technique, in the future. For this study, tests were performed using a simulation probe and applications to simulate a peculiar condition of the magnetosphere.

Keywords: Magnetohydrodynamics. Geomagnetic disturbance regimes. HILDCAA. Adaptive mesh refinement. Simulation probe.

IMPLEMENTAÇÃO DE SONDA DE SIMULAÇÃO E ANÁLISE NA MODELAGEM DO ACOPLAMENTO ELETRODINÂMICO ENTRE O VENTO SOLAR E A MAGNETOSFERA TERRESTRE: DOIS CASOS TÍPICOS DE MAGNETOHIDRODINÂMICA

RESUMO

As pesquisas de estruturas físicas relacionadas às ciências espaciais apresentam vários desafios devido a uma extensa gama de fenômenos. Particularmente para programas de Clima Espacial, espera-se que as modelagens magneto-hidrodinâmicas simulem os fenômenos da magnetosfera regulados pelas condições do meio interplanetário, caracterizando principalmente aqueles fenômenos eletrodinâmicos que podem interferir ou mesmo danificar infraestruturas e serviços à sociedade. Como objetivo principal, este trabalho visa analisar o acoplamento eletrodinâmico vento solar-magnetosfera sob um regimes geomagnéticos de moderado a fraco durante eventos HILDCAAs. Tais condições físicas caracterizam um desafio para as simulações devido às sutilezas existentes nos processos. Para este estudo, também contribuindo para a melhoria do código, foi desenvolvido e implementado um recurso de sonda em duas e três dimensões. Os esforços visam tirar proveito das características do framework, como o refinamento de malha adaptativa baseada em wavelets e uma técnica de divergência livre implementada, no futuro. Para este estudo foram realizados testes sobre o uso de uma sonda de simulação e aplicações para simular uma condição peculiar da magnetosfera.

Palavras-chave: Magneto-hidrodinâmica. Regimes de perturbação geomagnética. HILDCAA. Refinamento de malha adaptativo. Sonda de simulação.

LIST OF FIGURES

Page

LIST OF TABLES

Page

LIST OF ABBREVIATIONS

AE	–	Auroral Electrojet
AL	–	Auroral Lower
AMR	–	Adaptive Mesh Refinement
AMROC	–	Adaptive Mesh Refinement in Object-oriented C++
AP3M	–	Adaptive Particle Mesh
ART	–	Adaptive Refinement Tree
AU	–	Auroral Upper
ATHENA	–	Astrophysical magnetohydrodynamics C++
BATS-R-US	–	Block-Adaptive-Tree Solar-Wind Roe-Type Upwind Scheme
CRCM	–	Comprehensive Ring Current Model
CT	–	Constrained Transport
Dst	–	Disturbed Storm Time Index
EGLM	–	Extensive Generalised Lagrangian Multiplier
FAC	–	Field Aligned Current
GAMERA	–	The Grid Agnostic MHD for Extended Research Applications
GEM	–	Geospace Environment Modeling
GLM	–	Generalised Lagrangian Multiplier
HDF	–	Hierarchical Data Format
HILDCAA	–	High Intensity Long Duration Continuous Auroral Electroject Activity
HLLC	–	Harten–Lax–van Leer Contact
HLLD	–	Harten–Lax–van Leer Discontinuities
HLLE	–	Harten-Lax-van Leer-Einfeldt
IGLM	–	Ideal Generalised Lagrangian Multiplier
IMF	–	Interplanetary Magnetic Field
KHI	–	Kelvin-Helmholtz instability
LFM	–	Lyon Fedder Mobarry
MHD	–	Magnetohydrodynamic model
MPI	–	Message Passing Interface
NBZ	–	Northward Interplantary Magnetic Field currents
RAMSES	–	Adaptive Mesh Refinement for self-gravitating magnetized fluid flows
SCI	–	Shock-Cloud Iteration
SAMR	–	Structured Adaptive Mesh Refinement
SWMF	–	Space Weather Modeling Framework
TVD	–	Total Variation Diminish
ULF	–	Ultra low frequency
VTK	–	Visualization Toolkit

LIST OF SYMBOLS

$\mathbf{H}$	–	The magnitude of the magnetic field projected in the horizontal plane
r_E	–	Earth radii
ρ	–	single fluid mass density
β	–	beta plasma parameter
$\mathbf{B}$	–	magnetic field
p	–	plasma pressure
M_A	–	Alfvén mach number
V_u	–	upstream plasma velocity
c_A	–	Alfvén velocity
M_{ms}	–	magnetosonic Mach number
c_f	–	fast magnetosonic velocity
M_c	–	critical Mach number
E	–	electric field
u_{SW}	–	solar wind velocity
B_{SW}	–	solar wind magnetic field
L	–	long of the diffusion region
l	–	width of the diffusion region
u_i	–	inflow velocity
B_i	–	inflow magnetic field
u_o	–	outflow velocity
B_o	–	outflow magnetic field
S	–	Poynting flux
H	–	magnetic field strength
W	–	kinetic energy
σ	–	conductivity
R_m	–	magnetic Reynolds number
$\mathbf{a}$	–	acceleration
$\mathbf{g}$	–	gravity field
$\mathbf{v}$	–	velocity space coordinates
$\mathbf{J}$	–	current density
$\mathbf{B_d}$	–	dipole magnetic field of the Earth
Φ	–	viscosity
$\mathbf{I}$	–	identity matrix
$\mathcal{E}$	–	plasma internal energy
η	–	resistivity
D	–	diffusion term
ξ	–	distance to the origin
γ	–	adiabatic index

CONTENTS

Page

1 INTRODUCTION

In a general sense, solar-terrestrial physics is primarily concerned with the interaction of energetic electrically charged particles with the electric and magnetic field since the solar medium, through interplanetary space, and in the terrestrial environment.

This enchained-processes scenario is very complicated to understand, which requires collecting experimental measurements, developing theoretical studies, and the beneficial computation simulation results. Those research procedures can be used under different circumstances that compose the basis for the most diverse investigations. Throughout this half of the century, numerous technological challenges have arisen and determined deep research concerning the Space phenomena and interactions with day-by-day needs. By a particular approach explained later, this work intends to contribute to resources and knowledge in the multidisciplinary areas of Space Electrodynamics and Space Weather.

As an initial comprehensive view, the following description summarises the space environment. Due to the energy released by the nuclear reaction in the core, the other outer layers transfer energy and support material transportation in the Sun, involving plasma occurrences, electrical currents generations, and magnetic field manifestations. The more external layers emit electromagnetic radiation, corpuscular radiations, plasma structures, and an elongated solar wind magnetic field towards the interplanetary space from diverse and complicated processes (KIVELSON; RUSSELL, 1995).

Permeated by a geomagnetic field produced by an interior dynamo, the Earth's atmosphere is ionized by the radiation incidences, in a situation that propitiates a creation of a region filled with plasma, designated electrodynamics as the Magnetosphere-Ionosphere system. The magnetosphere is a region surrounding the Earth that avoids the direct presence of the solar wind's plasma. At the same time, the Ionosphere, about 70 to $2,000$ km, is the region having the highest ionized particle density.

The interplanetary magnetic field (IMF) interplays with the geomagnetic field. When fields present orientations in opposition or almost it, a merging process of those magnetic fields, involving particle fluxes, occurs and defines a geometrical location at the magnetosphere frontal solar side. Otherwise, a viscous interaction occurs surrounding the magnetosphere's outer boundary layer, the magnetopause, involving laminar flows and a displaced magnetic reconnection at the flanks beyond the magnetic poles.

Thus, the characteristic of the IMF is a significant parameter controlling the electrodynamics coupling between the solar plasma and the Earth, and as a consequence, the own magnetosphere dynamics (BAUMJOHANN; TREUMANN, 1996).

In the vicinity of the Earth, most of these charged particles derive their energy ultimately from the Sun or the interaction of the solar wind with the Earth's magnetosphere (KIVELSON; RUSSELL, 1995). In interplanetary space, the Earth's magnetic field and plasma environment interact with the supersonic solar wind flow, resulting from the steady outflow of the ionized solar atmosphere. As a result, complex regions are formed around the planet.

Most studies of magnetospheric dynamics have concentrated on the magnetic configuration when the IMF has a southward orientation and intense magnitude since the magnetosphere's most dynamic events, called magnetospheric storms and substorms, are associated with these conditions. Nevertheless, the IMF that presents a northward component deserves the same attention from observers. The same idea is valid for studies attempting to model the magnetospheric configuration when efforts explore conditions conducting to strong or severe events (OGINO et al., 1992).

A lack of studies seems to occur for weak or even moderate interplanetary causes because they do not conduct significant geoeffective processes. However, these weak or moderate disturbance-period characterizations can aid a better understanding of the physical principles involved due to subtle and complicated transitions in the magnetosphere.

Besides the valuable theoretical studies and experimental result interpretations, computational simulations add a complementary, powerful way to unravel the intimacy of processes, even under necessary restrictions dictate by the computing technology level, the numeric schemes available, and the capacity to propose realistic physical-mathematical representation. The first global magnetohydrodynamic (MHD) model of the magnetosphere was developed by (LEBOEUF et al., 1978). They used a particle MHD code and modeled the magnetosphere in two dimensions for both northward and southward IMF. For the northward case, they found a closed teardrop-shaped magnetosphere. Also, they did not represent a three-dimensional simulation for the northward IMF case. During periods of northward interplanetary magnetic field (IMF), an additional large-scale stable Field Aligned Current (FAC) system that is distinctive to the so-called *region 1* and *region 2* system develops at higher latitude poleward of the *region 1* system and has been denoted as the northward IMF B_z (NBZ) FAC configuration by (IIJIMA et al., 1984), and (IIJIMA;

SHIBAJI, 1987).

In this context, energy and momentum are transported from the solar wind to the magnetosphere by various interaction processes. The large-scale transport of plasma in the magnetosphere is equivalent to the existence of a global electric field. The process driving the magnetospheric convection also generates the FAC, as mentioned in Tanaka (1995), which shear the magnetic field and transmits magnetospheric perpendicular momentum to the polar ionosphere.

In general, most of the physics models of the Earth's magnetosphere can be described using magnetohydrodynamic (MHD) equations. First, space plasmas contain a great variety of phenomena and scales, which vary from the order of the fraction of the Earth's radius to the order of Sun-Earth distance. Second, simulation of the MHD equations represents usually a tremendous computational challenge cost because it requires accurate results due to the instabilities it involves. Finally, adaptive mesh refinement has a fundamental role in improving the results obtained in this kind of challenge.

The idea of adaptive multiresolution was introduced by Harten (1994), recently this method was compared by Deiterding et al. (2016) and integrated by Deiterding and Domingues (2017) into the Adaptive Mesh Refinement in Object-oriented C++ (AMROC) framework. This framework uses a message-passing interface (MPI) to perform parallel computations in a patch-structured adaptive mesh refinement for finite volumes methods. Also, AMROC has excellent computational performance. Currently, some frameworks have those kinds of qualities such as *ATHENA* and *RAMSES*. The first one is an astrophysical MHD flow that uses the Adaptive Mesh Refinement framework and Constrained Transport (CT) to deal with the divergence problem of the magnetic field. The current implementation allows solving the Euler equations in the presence of self-gravity and cooling treated as additional source terms in the momentum and energy equations (FROMANG et al., 2006). The second one is a new code for astrophysical MHD that uses the Adaptive Mesh Refinement framework and the Constrained Transport (CT) technique to enforce the divergence-free constraint on the magnetic field (STONE et al., 2008). The current version supports the following physics: compressible hydrodynamics and MHD in 1D, 2D, and 3D; special and general relativistic hydrodynamics. Both are written in C++ and use parallel architectures when linked adequately to the MPI library.

A proper representation faces challenges to simulate complete behaviors inside the solar wind-magnetosphere-ionosphere system because of the initial and boundary

conditions. On another side, to get a better simulation of currents that appear as a consequence of the IMF is necessary to represent the inner boundary layer concerning the Ionosphere adequately. Additionally, computational numeric problems must be overcome, such as the divergence of the magnetic field. Besides that, dealing with different behavior conditions for the IMF creates motivational cases of studies. The southward or northward IMF orientations will get different magnetosphere configurations, magnetic reconnection, and ionospheric currents, and even the position of the bow shock, magnetopause, and magnetosphere must be different with this variation. Also, a condition exists when the IMF is alternating between southward and northward continuously in time; consequently, complicated configurations and processes must appear. Finally, this work aims to deal with those study cases taking satellite values in the solar wind close to the Earth as input and implementing an artificial probe, i.e. simulation probe, to know conservative variables or transient modifications in different areas of the magnetosphere.

In this context, the general goal of this work is:

- Implement a simulation probe and analyse the magnetosphere behaviour for the solar wind-magnetosphere electrodynamics under a moderate-to-weak geomagnetic disturbance regime using the AMROC (MHD2D) framework.

The specific goals are:

- Examine two typical electrodynamical coupling processes producing moderate to weak geomagnetic disturbances.
- Collaborate in the structuring of the AMROC-MHD model by implementing a 3D probe resource aiming at the use of a future 3D code.
- Produce time series in the magnetosphere environment using AMROC.

The results of this work are to contribute to a better understanding of nuances of the magnetosphere electrodynamics under interplanetary causes of weak-moderate geomagnetic disturbances. At the same time, the efforts collaborate with the implementations and tests of the AMROC framework developed at INPE.

This work follows, as an outline, this organization. As seen, Chapter 1 contains the general lines involving the study background and the goals. Chapter 2 describes the

physical structure of Earth's magnetosphere. Chapter 3 presents the physical aspects of the electrodynamics coupling between the solar-wind plasma and the magnetosphere. Chapter 4 takes the magnetohydrodynamics formalism, the AMROC-MHD framework to be used for simulation, and the magnetosphere simulation approach. Chapter 5 discusses the measuring probe 2D and 3D implementations for use in the AMROC simulations and present some verification tests. Chapter 6 discusses the simulations of the magnetosphere in 2 dimensions. The conclusions are presented in Chapter 7. Additionally, *Appendix A* mentions other MHD codes besides AMROC to contextualize the latter. In order to show the contributions in the development of the three dimensional magnetospheric modelling, the *Appendix B* shows the discretization of the ionosphere potential and also the computation of the derivatives of the conductances required by the development of the magnetosphere-ionosphere coupling model proposed by (GOODMAN, 1995) and described in the *Appendix C*. This coupling process will be used as internal boundary conditions for the future 3D magnetospheric simulations. *Appendix D* presents the probe 2D data series concerning the complete intervals of data simulation. At last, *Appendix E* describes the geomagnetic disturbance regimes based on the low latitude measurements on the ground.

2 THE EARTH'S MAGNETOSPHERE

This chapter describes the essential regions and features concerning the Earth's magnetosphere and, even with some limitations, the coupling to the ionosphere.

In that context, Figure 2.1 shows a cross-section of the magnetosphere in the noon-midnight meridian, with the north in relation to the ecliptic plane, at the top and the Sun on the left. The regions of the magnetosphere and other related locations are labeled. In addition, the dipole region of the Earth's magnetosphere is called the inner magnetosphere (MOLDWIN, 2008). On the nightside at about geosynchronous orbit (6.6 r_E), the magnetic field lines become stretched into an extended tail-like configuration. The interaction of Earth's magnetic field with the solar wind is re-

Figure 2.1 - Structure of the Earth's magnetosphere.

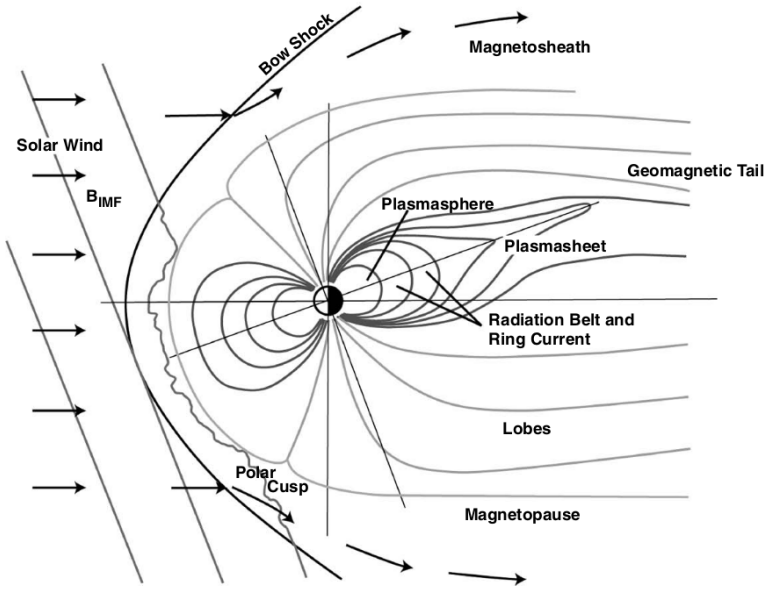

A noon-midnight cross-section of Earth's magnetosphere.
SOURCE: Adapted from Moldwin (2008).

sponsible for the distortion of its dipole field. The non-dipolar regions are called the outer magnetosphere.

2.1 Solar wind

Initially, it is convenient to consider the solar wind, because it acts as a changing forcing driver upon the Earth's environment. The Sun emits highly conducting plasma into interplanetary space as a result of the supersonic expansion of the solar corona. This plasma is called the solar wind. It flows with a supersonic speed of about 400Kms^{-1} and consists mainly of electrons and protons, with an admixture of 5% helium ions. Because of the high conductivity, the solar magnetic field is frozen in the plasma and drawn outward by the expansion of the solar wind. Typical values for electron density and temperature in the solar wind near the Earth are 5cm^{-3} and 10^5K respectively. The interplanetary magnetic field strength is of the order of $5 - 10$nT near the Earth's orbit (KIVELSON; RUSSELL, 1995).

2.2 Magnetosphere

The shocked solar wind plasma in the frontal adjacent region to Earth cannot easily penetrate the terrestrial magnetic field but is mostly deflected around it. This is a consequence of the fact that the interplanetary magnetic field lines cannot penetrate the terrestrial field lines and that the solar wind particles cannot leave the interplanetary field lines due to the aforementioned frozen-in characteristic of a highly conducting plasma. The boundary separating the two different regions is called magnetopause and the cavity generated by the terrestrial field has been named magnetosphere. The kinetic pressure of the solar wind plasma distorts the outer part of the terrestrial dipolar field. On the dayside, it compresses the field, while the nightside magnetic field is stretched out into a long magnetotail that reaches far beyond lunar orbit (BAUMJOHANN; TREUMANN, 1996).

2.3 Bow shock

The supersonic solar wind incident upon an obstacle, the Earth's magnetosphere, creates a shock region involving the planet. Because Earth's bowshock is the closest space shock to the Earth its importance is vital considering the position and shape of planetary bowshocks becomes rather important. The position and shape of a bowshock are determined by the interaction of the solar wind with the planetary magnetosphere (SPREITER et al., 1966). In particular, the solar wind is stopped where its ramp (transition from the upstream to the downstream state) pressure ρu_{SW}^2 is balanced by the planetary magnetic field pressure $\frac{B^2}{8\pi}$. Schematically planetary bowshock of a magnetized planet and the magnetopause (marked r_0), that separates the planet's magnetosphere from the solar wind with solar origin plasma, are shown

in Figure 2.2. Another parameter used for shock classification is the kinetic-to-

Figure 2.2 - Planetary Bowshock position.

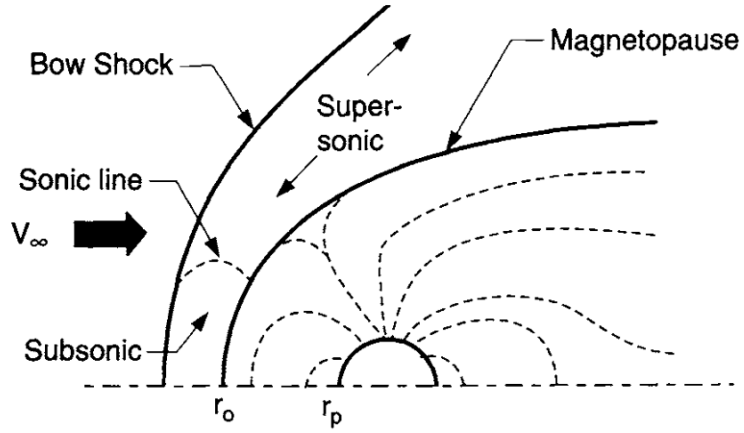

The magnetopause separates the solar wind particles from those that belong to the magnetosphere.

SOURCE: Spreiter et al. (1966).

magnetic pressure ratio $\beta = \frac{2\mu_0 p}{B^2}$. The most important shock parameter is its Mach number, either Alfvén $M_A = \frac{V_u}{c_A}$ where V_u is the upstream plasma velocity and c_A is the Alfvén velocity, or magnetosonic $M_{ms} = \frac{V_u}{c_f}$ where c_f is the fast magnetosonic velocity. Theory predicts that the shock structure should change drastically when the downstream plasma velocity exceeds the downstream sound velocity (KENNEL, 1988). This happens at some critical M_c. Accordingly, shocks with $M_{ms} < M_c$ are called subcritical and those with $M_{ms} > M_c$ are supercritical.

2.4 Magnetosheat

The solar wind impinges on the Earth's dipolar magnetic field, it cannot simply penetrate it but is slowed down and, to a large extent, deflected around it. Since the solar wind hits the obstacle with supersonic speed, a bow shock wave is generated, where the plasma is slowed down and a substantial fraction of the particles' kinetic theory is converted into thermal energy. The region of thermalized subsonic plasma behind the bow shock towards the Earth is called the magnetosheath. Its plasma is denser and hotter than the solar wind plasma and the magnetic field strength has higher values in this region (BAUMJOHANN; TREUMANN, 1996).

2.5 Plasma in the Earth's middle and inner magnetosphere

It is known that three major plasma regions exist in the near part of the Earth's magnetic tail. In general, there is no precise definition of these regions, but Eastman et al. (1985) define them as:

- **Tail Lobes:** Plasma densities are low, generally less than 0.1cm^{-3} and sometimes below the level of detectability. Ion and electron spectra are very soft, with very few particles in the $5 - 50\text{keV}$ range. Cold ions are often observed flowing away from the Earth, and their composition often suggests an ionospheric origin. There is strong evidence that the tail lobe normally lies on open magnetic field lines (KIVELSON; RUSSELL, 1995).

- **Plasma-Sheet Boundary Layer:** Ions in this region typically exhibit flow velocities of hundreds of kilometers per second, principally parallel to or antiparallel to the local magnetic field. Frequently, counterstreaming ion beams are observed, with one beam traveling earthward, and the other traveling tailward along the field line. Densities typically are of the order of 0.1cm^{-3}, and thermal energies tend to be smaller than the flow energies (KIVELSON; RUSSELL, 1995).

- **Plasma Sheet:** This region, often referred to as the central plasma sheet to emphasize its distinctness from the plasma sheet boundary layer, consists of hot (kilovolt) particles that have nearly symmetric velocity distributions. Number densities typically are $0.1 - 1\text{cm}^{-3}$, a little bit higher than that plasma sheet boundary layer (PSBL). Flow velocities are very small compared with the ion thermal velocity. In this context, the term plasma sheet describes both electrons and ions, appending the word electron or ion when discussing only one species of plasma (KIVELSON; RUSSELL, 1995). The ion temperature in the plasma sheet is almost invariably about seven times the electron temperature (BAUMJOHANN; TREUMANN, 1996).

Those structures are shown in Figure 2.3.

2.6 Another structures

Another plasma region is the plasmasphere which consists mostly of hydrogen and helium, but also an appreciable amount of oxygen, that has just enough energy to escape from the Earth's ionosphere. As plasma drifts up the magnetic field line

Figure 2.3 - Plasma regions in the middle and inner magnetosphere.

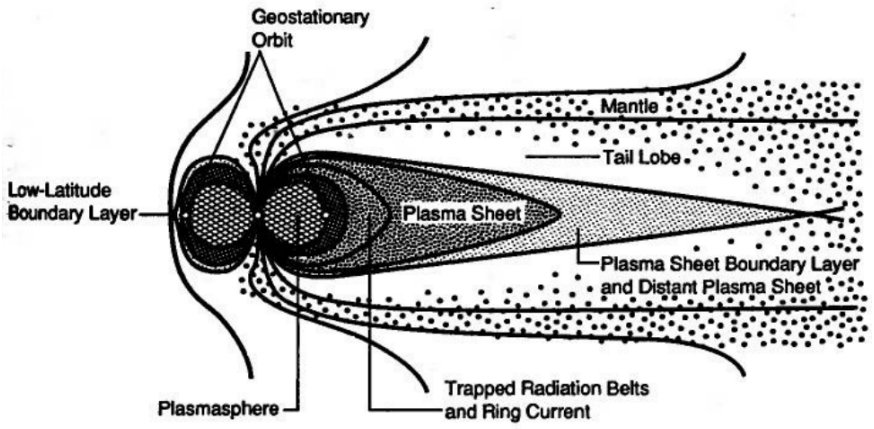

Plasma regions of the Earth's magnetosphere as viewed in the noon-midnight meridian plane.

SOURCE: Kivelson and Russell (1995).

from below, it becomes trapped and co-rotates with Earth. There is often a very sharp boundary to the dense plasmasphere called the plasmapause (BAUMJOHANN; TREUMANN, 1996). Plasma density frequency drops an order of magnitude within a very short radial distance (less than 0.5 r_E). Often with the plasmasphere are the Van Allen radiation belts and the ring current. These two regions are characterized by high energy particles that are trapped in Earth's magnetosphere (KIVELSON; RUSSELL, 1995).

The ring current is made up of particles with a peak energy of about 200 KeV, while the radiation belts consist of particles with energies extending into the relativistic regime. Relativistic particles have velocities near the speed of light and carry a tremendous amount of kinetic energy. The ring current is so named because its charged particles produce an electric current that encircles Earth (KIVELSON; RUSSELL, 1995). Figure 2.4 is a schematic of the magnetosphere showing both the noon–midnight meridian and the equatorial plane. The solid arrows indicate the directions of the different currents flowing in the magnetosphere. Because of the shape and strength of Earth's dipole magnetic field region, energetic ions flow from midnight to dusk side, and energetic electrons flow in the opposite direction. This difference in flow directions of positively charged ions and negatively charged electrons gives rise to an electric current, a ring current that circles Earth.

This ring current in turn gives rise to a magnetic field that points in the opposite direction to the horizontal field of the Earth's magnetic field (KIVELSON; RUSSELL, 1995). Therefore, the ring current decreases the strength of Earth's magnetic field as measured on the surface. In particular, instruments near the equator constantly measure the strength of the magnetic field. When the ring current intensifies suddenly appear a rapid decrease in magnetic field strength. A magnetic index, called the Disturbed Storm Time Index (Dst), measures the deviation or change in Earth's magnetic field from its normal quiet time value, the strength of Earth's internal magnetic field. If this index goes negative (indicating a decrease in Earth's field), it is due to intensification or increase in the strength of the ring current (KIVELSON; RUSSELL, 1995). In addition, in Figure 2.4 there are other currents, called

Figure 2.4 - Earth's magnetosphere showing the equatorial and noon-midnight meridional planes.

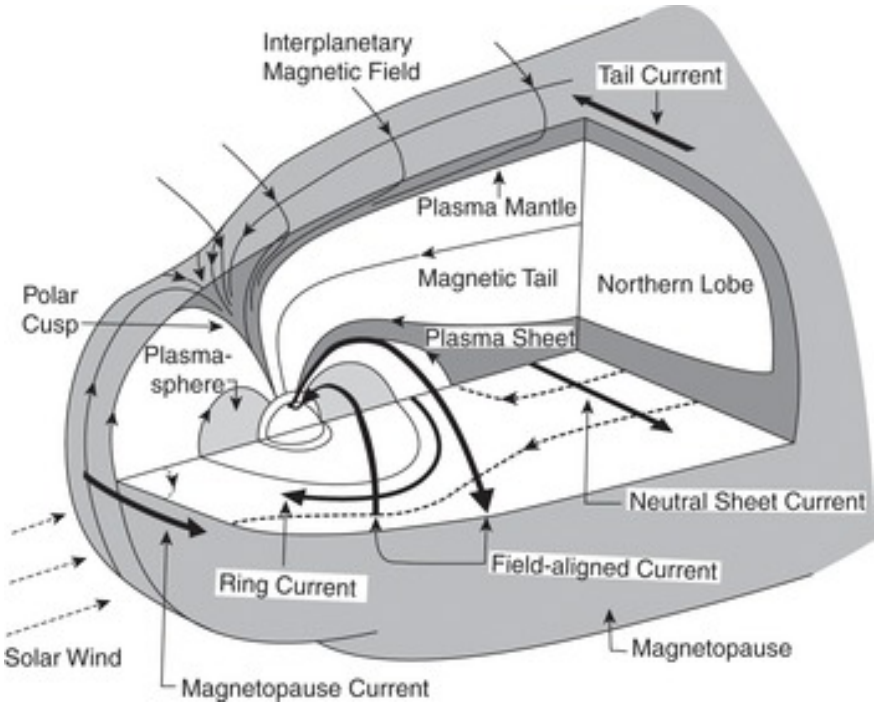

The electric current flowing in the magnetosphere is shown as dark arrows.
SOURCE: Russell and Luhmann (1997).

field-aligned currents, that connect the ring current and plasma sheet to the high-latitude ionosphere. These currents play a major role in aurora and other space weather phenomena.

3 THE ELECTRODYNAMICS COUPLING PROCESS ASPECTS

Concerning the effects of the solar-wind plasma upon the Earth's magnetosphere, several electrodynamical processes can be considered. A significant phenomenon is a magnetic reconnection triggered by the predominance of the southward IMF orientation (taking into account the GSM coordination system (KIVELSON; RUSSELL, 1995)). Otherwise, a laminar flow regime is established in the magnetosphere flanks, involving sometimes the remarkable presence of plasma instabilities. Indeed, both phenomena affect magnetospheric dynamics. General aspects complicate the physics of the magnetosphere such as the solar plasmas acting like a fluid, their own magnetic reconnection, frozen flux, magnetic diffusion, and geomagnetic disturbances in all extensions of the magnetosphere. Some details are presented as follows.

3.1 Magnetic reconnection and magnetospheric dynamics

To allow a discussion, it is assumed initially that the interplanetary magnetic field is directed predominantly southward, as illustrated in Figure 3.1. The magnetic field driven by the solar-wind flow against the front of the magnetosphere will be approximately anti-parallel to the geomagnetic field on the other side of the magnetopause. Suppose that a magnetic x-line forms there and reconnection occurs between the field lines labeled 1 and $1'$ (KIVELSON; RUSSELL, 1995). Then, instead of a purely geomagnetic-field line with both ends attached to the Earth and an interplanetary field line with both ends on the Sun or at least stretching far from the Earth obtaining two field lines of a new type. These new field lines each have one end attached to the Earth, one near the North Pole and one near the South Pole, and the other end stretching out into interplanetary space (KIVELSON; RUSSELL, 1995).

The solar-wind flow will pull the solar-wind portion of the field line antisunward, or, to put it another way, the plasma on the flux tube will sense an electric field $E = u_{SW} \times B_{SW}$. In a steady state, the electric field must be sensed all along these now open flux tubes, as field lines are equipotentials. At the ionospheric end of the field line, this electric field, which is directed from dawn toward dusk, drives flow from noon toward midnight, as observed. Thus the field line moves successively through the numbered locations in Figure 3.1, and this process naturally draws out flux tubes to form geotail (KIVELSON; RUSSELL, 1995). If this process went on indefinitely without some method of returning magnetic flux to a closed state labeled 6 and 6' of Figure 3.1, the entire geomagnetic field would soon be connected with the interplanetary field.

Figure 3.1 - Magnetic reconnection and magnetospheric dynamics.

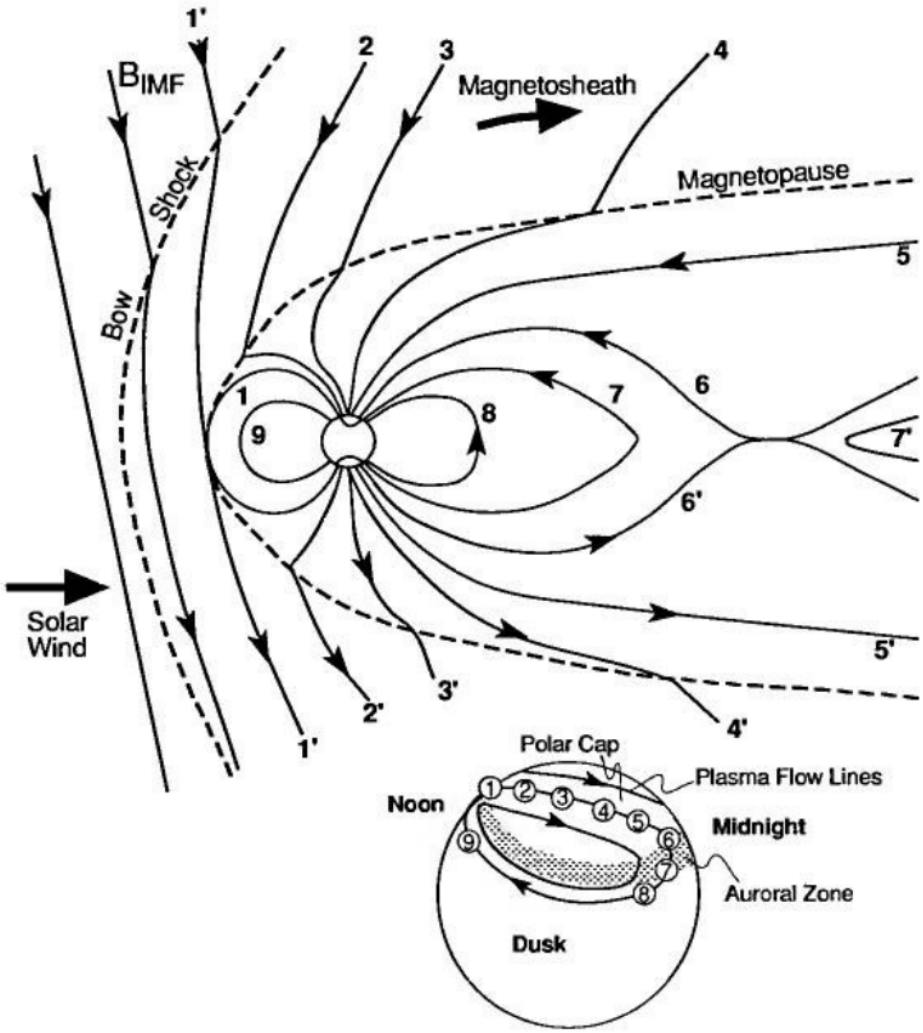

Flow of plasma within the magnetosphere (convection) driven by magnetic reconnection. The numbered field lines show the succession of configurations a geomagnetic field line assumes after reconnection with a southward IMF.

SOURCE: Kivelson and Russell (1995).

The return of flux is achieved by reconnection at another x-line in the tail. Here, two open lines, one from the northern tail lobe and the other from the south, reconnect to form a newly closed geomagnetic field line and a new, purely interplanetary field line. The new interplanetary flux tube contains some plasma of terrestrial origin and is distorted and stressed; it continues flowing to the right and ultimately rejoins the solar wind flow. The new geomagnetic field line is also stressed and attempts both to flow and to relax earthward, though this may be hindered by the pressure of the

plasma contained in the flux tube. The flow circuit is finally closed when the newly closed field lines flow around either the dawn or dusk side of the Earth back to the dayside (BISKAMP, 1994). The inset in Figure 3.1 shows the flow of the end of the field line in the northern ionosphere and shows how to the return flow occurs at lower latitudes.

This description is grossly oversimplified. In practice, the entire pattern is inherently non-steady (which can give rise to inductive electric fields that do not map along field lines), and although in a time-average sense, the reconnection rates at the magnetopause and in the tail must equal, on an instantaneous basis they probably rarely are (DUNGEY, 1961). It would be fair to say that magnetospheric physics is largely about understanding the dynamics and transport associated with this flow.

Although magnetic reconnection is the dominant means of momentum coupling to the solar wind, some sort of viscous interaction probably does account for some small fraction of momentum transfer, perhaps $10 - 20$ percent on average. Nevertheless, Dungey (1961)'s picture of an open magnetosphere provides a framework to which details may be added; it demonstrates the fundamental role that magnetic reconnection plays in magnetospheric physics.

3.2 Fluid description of magnetic reconnection

As mentioned in Kivelson and Russell (1995), the magnetic reconnection can be represented using an MHD fluid description. The models can be approximated by a time-stationary and two-dimensional representation. The main concern will be to establish that reconnection can proceed fast enough for it to have an effect on space plasma systems. Here, we consider the plasma far from the diffusion region as indicated in Figure 3.2. The diffusion region, shown shaded, is $2L$ long and $2l$ wide, where $L >> l$. For sake of simplicity, it is assumed that the inflow and outflow regions (parameters that are identified by subscripts i and o) are symmetrical. This is appropriate for the reconnection tail, where the inflowing plasma comes from the northern and southern lobes. At the magnetopause, the two inflow regions are quite different. As before, the electric field E is spatially uniform and points out of the page, so that:

$$E = u_i B_i = u_o B_o \tag{3.1}$$

The flow is incompressible, that is, $\rho_i = \rho_o = \rho$, then conservation of mass gives

$$u_i L = u_o l \,. \tag{3.2}$$

Figure 3.2 - Reconnection geometry.

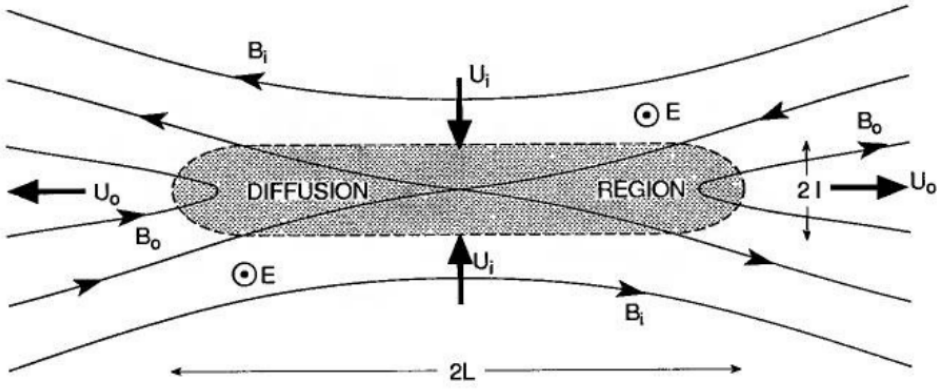

All the reconnecting plasma flows through the shaded diffusion region as a consequence, very slow reconnection results.

SOURCE: Kivelson and Russell (1995).

So, the kinetic energy gained by the outflowing plasma with the electromagnetic energy flowing into the diffusion regions. The electromagnetic energy inflow rate per unit area is given by the Poynting flux:

$$S = E \times H = \frac{EB_i}{\mu} = \frac{u_i B_i^2}{\mu_0} \,. \tag{3.3}$$

The mechanical energy out is given by the gain in kinetic energy of the outflowing plasma. The mass flowing in per unit area per unit time, ρu_i, is accelerated to speed ρu_o, so that the rate of energy gain per unit area in the incident flow is

$$W = \frac{1}{2}\rho u_i (u_o^2 - u_i^2) \,. \tag{3.4}$$

Equating the energy rates in 3.3 and 3.4, and using $u_o >> u_i$, which follows from 3.2, gives

$$\frac{u_i B_i^2}{\mu_0} = \frac{1}{2}\rho u_i u_o^2 \,, \tag{3.5}$$

Finally gets:

$$u_o^2 = \frac{2B_i^2}{\mu_o \rho} = 2c_{Ai}^2 \,, \tag{3.6}$$

where c_{Ai} is the Alfvén velocity in the inflow region. From the magnetic annihilation, the calculation is obtained $l = \frac{1}{\mu_0 \sigma u}$, the thickness of the diffusion region. Combining

3.2 and 3.6 gives an expression for the inflow speed:

$$u_i^2 = 2^{\frac{1}{2}} \frac{c_{Ai}}{\mu_o \sigma L} \tag{3.7}$$

$$u_i = c_{Ai} (\frac{2^{\frac{1}{2}}}{R_m})^{\frac{1}{2}} \tag{3.8}$$

where $R_m = \mu_o \sigma c_{Ai} L$. What this means is that in all solar-system plasmas for which R_m is very large, the inflow into the reconnection site, which corresponds to the reconnection rate, is very, very slow. Using, for instance, typical solar-corona parameters, a solar flare would take tens of days to grow, rather than a few minutes as observed.

However, a few years later, PETSCHECK (1964) solved the rate problem by realizing that most of the plasma involved in the reconnection process does not need to flow through the diffusion region in order to be accelerated. Instead, it can be accelerated in the region where MHD is still valid, the so-called convection region. The acceleration occurs as the plasma passes through shock waves that are connected to the diffusion region and that remain fixed in space, that is, they stand in the flow. This process removes the bottleneck caused by requiring that all the plasma come within a length l of the midplane, and so a much larger inflow rate can be accommodated (KIVELSON; RUSSELL, 1995).

3.3 Frozen flux and magnetic diffusion

To study plasmas, frozen flux, and magnetic diffusion concepts are significant phenomena involved with interplanetary and planetary magnetized plasma manifestation (BAUMJOHANN; TREUMANN, 1996). Initially, someone can consider the electromagnetic field equations, which describe the behavior of magnetic and electric fields as:

$$\nabla \cdot \mathbf{B} = 0 \qquad \text{(Gauss' law - Magnetism)}\,, \tag{3.9}$$

$$\nabla \times \mathbf{E} = -\frac{\partial \mathbf{B}}{\partial t} \qquad \text{(Faraday's law)}\,, \tag{3.10}$$

$$\nabla \times \mathbf{B} = \mu_0 \mathbf{J} \qquad \text{(Ampere's law)}\,, \tag{3.11}$$

and

$$\nabla \cdot \mathbf{E} = \frac{\rho_c}{\epsilon_0} \qquad \text{(Gauss' law)} \tag{3.12}$$

where $\mathbf{J}$ is the current density, ρ_c is the charge density, and μ_0 is the magnetic constant permeability, along with the Maxwell equations, the system of equations is

also completed with the Ohm's law:

$$\mathbf{J} = \sigma(\mathbf{E} + \mathbf{u} \times \mathbf{B}) \tag{3.13}$$

where σ is the conductivity.

Using Equation 3.13 to eliminate the electric field from Equation 3.10 obtaining:

$$\frac{\partial \mathbf{B}}{\partial t} = \nabla \times (\mathbf{u} \times \mathbf{B} - \frac{\mathbf{J}}{\sigma}) \tag{3.14}$$

Using Equation 3.11 and Equation 3.9 obtaining:

$$\frac{\partial \mathbf{B}}{\partial t} = \nabla \times (\mathbf{u} \times \mathbf{B}) + \frac{1}{\mu_0 \sigma} \nabla^2 \mathbf{B} \tag{3.15}$$

The magnetic field at a point in a plasma can be changed by the motion of the plasma described in the first term on the right-hand side. It can also be changed by diffusion due to the second term on the right-hand side.

Assuming the plasma to be at rest and dropping the first term on the right-hand side of Equation 3.15, it becomes a diffusion equation for the magnetic field

$$\frac{\partial \mathbf{B}}{\partial t} = D_m \nabla^2 \mathbf{B}\,, \tag{3.16}$$

with the *magnetic diffusion coefficient* given by

$$D_m = \frac{1}{\mu_0 \sigma} \tag{3.17}$$

Under the influence of finite resistance in the plasma, the magnetic field tends to diffuse across the plasma and to smooth out any local inhomogeneities (BAUMJOHANN; TREUMANN, 1996). In contrast, in cases where the magnetic diffusion is negligible refers to *froze-in magnetic flux*. In collisionless plasmas with infinite conductivity, Equation 3.15 reduces to

$$\frac{\partial \mathbf{B}}{\partial t} = \nabla \times (\mathbf{u} \times \mathbf{B})\,. \tag{3.18}$$

The equation mentioned above implies that any field changes are such if the magnetic field lines are constrained to move with the plasma (BAUMJOHANN; TREUMANN, 1996).

Using Equation 3.10 in Equation 3.18, will yield the *frozen-in flux theorem*:

$$\mathbf{E} + \mathbf{u} \times \mathbf{B} = 0 \tag{3.19}$$

This equation shows that in an infinitely conducting plasma, there are no electric fields in the frame moving with the plasma. Electric fields can only result from a Lorentz transformation. Moreover, this equation contains another important point. Since the cross-product between any velocity component parallel to the magnetic field and the field itself is zero. As a consequence, any component of the electric field parallel to the magnetic field must vanish in an infinitely conducting plasma.

3.4 Magnetic activity

A very useful, auxiliary procedure to study the interaction between the solar plasmas and the magnetosphere-ionosphere system is the monitoring and evaluating of geomagnetic disturbances. Magnetic activity at the Earth's surface is usually produced by electric currents in the magnetosphere and ionosphere. Magnetic measurements at many locations provide one means of remotely sensing these currents and recording how they change with time. Because it is relatively inexpensive to make magnetic measurements, and because they are unaffected by weather, they provide an ideal way of routinely monitoring these currents (KIVELSON; RUSSELL, 1995). Useful reviews of magnetic indices include those by Baumjohann and Treumann (1996) and Mayaud (1980).

Figure 3.3 includes various currents, for example, the magnetopause current, the tail current, and the ring current. Additional currents illustrated include the *partial current*, which flows near the equatorial plane principally near dusk, closing through the ionosphere, to which it is linked by field-aligned currents, and the *substorm current wedge*, a diversion of the tail current that also links into the ionosphere through field-aligned currents.

The ionospheric portions of these current systems flow in enhanced-conductivity channels at high latitudes and are called the *auroral electrojets*. Sheets of field-aligned currents centered near dawn and dusk are referred to as *region-1* and *region-2* currents. The higher latitude region-1 currents flow into the ionosphere from the dawn sector and out at dusk.

The lower latitude region-2 currents have the opposite polarities. It is remarkable to know that are not shown polar-cusp currents, polar-cap closure of the electrojets,

Figure 3.3 - Current systems.

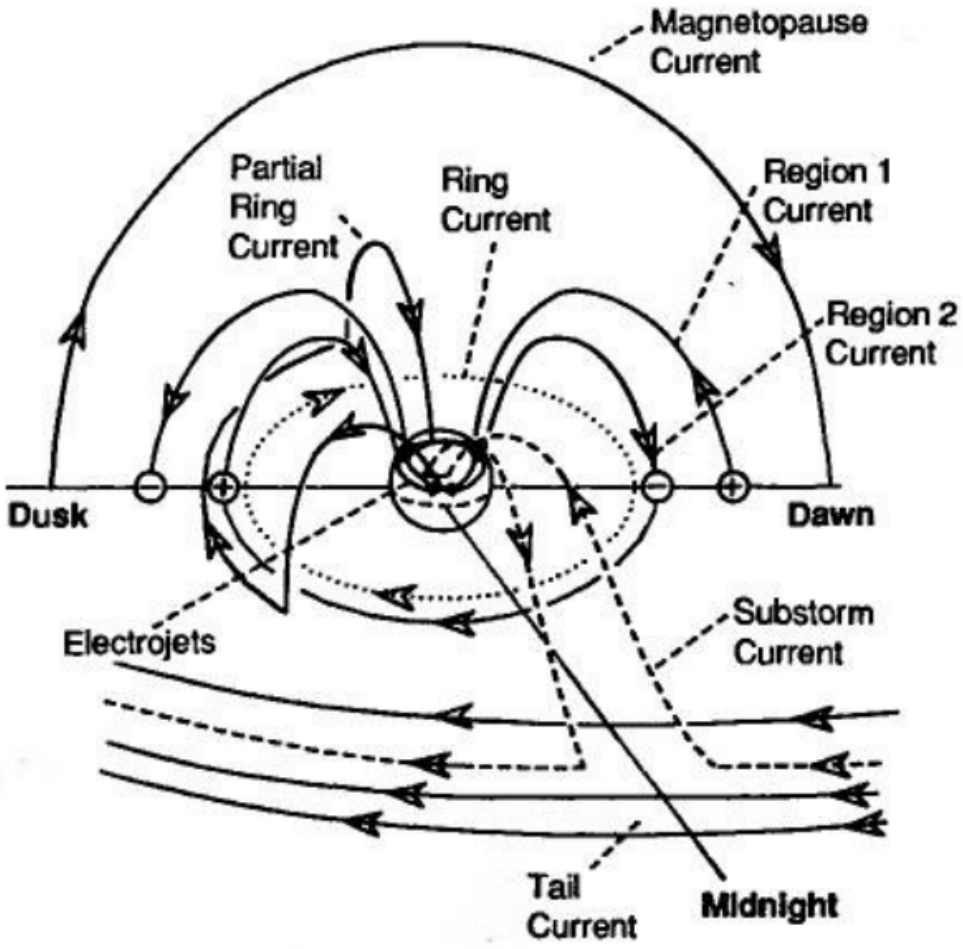

Schematic representation of current system linking magnetospheric and ionospheric currents.

SOURCE: Kivelson and Russell (1995).

and currents associated with IMF effects.

3.4.1 Geomagnetic substorms

The most frequent type of geomagnetic activity is referred to as a *magnetospheric substorm*. A substorm is the ordered sequence of events that occurs in the magnetosphere and ionosphere when the IMF turns southward and increases energy flows from the solar wind into the magnetosphere (MCPHERRON, 1970; AKASOFU, 1968). The most obvious manifestation of a substorm is the aurora (ROSTOKER, 1972). Dur-

ing a substorm, quiet auroral arcs suddenly explode into brilliance. They become intensely active and colored. Over a period of about an hour, they develop through an ordered sequence that depends on time and location. Magnetic disturbance also accompanies the aurora. On the surface beneath the aurora, a magnetometer will record intense disturbances caused by electric currents in the ionosphere.

In addition, the form of these magnetic disturbances as a superposition of the perturbations recorded in the **H** component at a number of auroral-zone observatories. Also, stations located in the afternoon-to-evening sector record positive disturbances, whereas stations near and past midnight record negative disturbances relative to the field measured on quiet days (KIVELSON; RUSSELL, 1995). So, applying the right-hand rule to currents assumed to overhead lead to the conclusion that the currents are respectively eastward and westward toward midnight. These currents are called *electrojets* because the currents flow in concentrated channels of high conductivity produced at $120km$ by the particles that generate the auroral light. Typical disturbances have amplitudes in the range of $200 - 2000$nT, and duration of $1 - 3$h. Figure 3.4 illustrates the three substorm phases: growth, expansion, and recovery in terms of the AU and AL indices. The AU and AL are envelopes of the superposed **H**-component traces from a worldwide chain of auroral-zone magnetometers underneath the electrojets. In addition, the beginning and end of an isolated substorm are defined by the departure and return of both those indices to background levels defined by the quiet-day variations. Finally, the growth phase is then the initial interval of slowly growing AU and AL (KIVELSON; RUSSELL, 1995).

The magnetosphere undergoes a distinct sequence of changes in its magnetic field and plasma, associated with the changes in the auroral current systems. The IMF turns southward. The dayside magnetopause is eroded, and the associated magnetic flux is transported to the tail lobes. The plasma sheet thins and the tail current moves earthward. A connected pair of X- and O-type neutral lines form in the near-Earth plasma sheet.

Magnetic reconnection at this X-line forms a bubble of plasma in the plasma sheet. This bubble is disconnected and pulled out of the center of the tail. The extra flux in the lobes reconnects earthward of the bubble and convects back to the dayside (KIVELSON; RUSSELL, 1995). Particles energized at the X-line are injected into the inner magnetosphere and drift in the radiation belts. Eventually, the near-Earth portion of the X-line moves tailward, establishing a distant X-line. These events constitute the three phases of a substorm as seen in the magnetosphere substorm.

Figure 3.4 - Substorm phases.

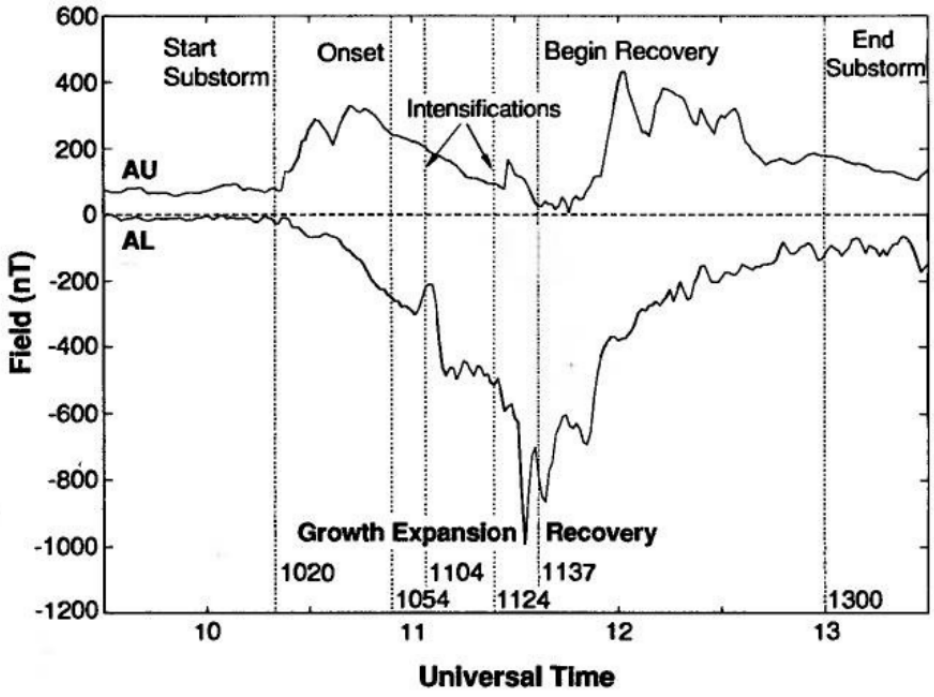

AU and AL indices for a particular substorm. The three phases of this substorm (growth, expansion, and recovery) can be identified by examination of the slope of the AL index.

SOURCE: McPherron and Manka (1985).

3.4.2 Geomagnetic storms

As mentioned in Kivelson and Russell (1995), while an isolated substorm is created by a brief (30-60min) pulse of southward IMF; when the IMF remains southward for longer times, the activity becomes more complex. Although there is a series of overlapping auroral-zone activation, there are also injections of particles into the inner magnetosphere. The injected particles drift in a ring around the Earth. Protons drift westward, and electrons eastward, creating a westward current called the *ring current*.

Some particles from each activation are accelerated by drift across the enhanced magnetospheric electric field. The stronger the electric field, the greater their energy, and the closer the ring current is to the Earth (KIVELSON; RUSSELL, 1995). In addition, particles are accelerated out of the ionosphere into the equatorial plane, so that heavy ions such as oxygen become important in the ring current. The ring

current causes large decreases in the **H** component over most of the Earth's surface. This effect is known as a *geomagnetic storm*.

As long as the injection of particles continues, the ring current will grow toward some asymptotic value in which the rate of injection equals the rate of loss. The time during which the ring current is growing is called the *main phase* of the magnetic storm. However, as soon as the IMF weakens, or turns northward, the ring current stops growing, and the ground perturbations begin to decrease. The ground perturbations decrease principally because particles are lost from the ring current. Thus, the perturbation decrease on the ground is depicted using the DST index in Section 6.2, Section 6.3, and Section 6.4.

The rate of dayside reconnection decreases and the convection boundaries move to larger radial distances (KIVELSON; RUSSELL, 1995). The ionosphere begins to refill flux tubes within the new boundary. As the cold ionospheric plasma encounters the ring-current plasma, ion-cyclotron waves begin to grow, and these waves scatter the ring-current protons into the loss cone. Other ring-current ions charge-exchange with the cold neutral hydrogen. The ring current ions become energetic neutral atoms and are lost to the atmosphere or outer space. The low-energy ions that replace them contribute little current, and so the strength of the ring current decreases with time. This is the *recovery phase* of the storm. Many storm recoveries occur in at least two stages. The first stage results from the rapid loss of oxygen ions, and the second stage is from the slower loss of protons.

Some geomagnetic storms are preceded by an initial phase of enhanced **H** component in ground magnetometer records. This effect is unrelated to the ring current and is caused by an enhancement of the magnetopause current. Many magnetic storms follow solar flares or coronal mass ejection (KIVELSON; RUSSELL, 1995). In either case, a high-speed parcel of the Sun's atmosphere sweeps through slower solar wind, compressing and distorting the magnetic field ahead of it. That parcel of gas then encounters the Earth's field and compresses it, enhancing the magnetopause currents and thereby producing positive perturbations in **H** at the Earth's surface.

This compression of the field is called a *sudden impulse*. In many storms, this phase will last for 4-16h, as long as the IMF is northward. Eventually, the IMF will turn southward, and there will be a sequence of substorms and also the production of a geomagnetic storm. The **H** component that results from the superposition of the enhanced magnetopause current (positive $\triangle H$) and the ring current perturbation (negative $\triangle H$) is negative, even though the solar-wind dynamic pressure may remain

elevated for some time.

3.5 Plasma conductivity

As mentioned in Baumjohann and Treumann (1996), plasma in the ionosphere is partially ionized, and also considering the strong magnetic field in it, with these facts is necessary to add the collisional term to the equation of motion, calculated as:

$$m\frac{d\mathbf{v}}{dt} = q(\mathbf{E} + \mathbf{v} \times \mathbf{B}) - m\nu_c(\mathbf{v} - \mathbf{u}) \tag{3.20}$$

where E is the electric field, v is the charged particle velocity, B magnetic field, ν_c is the collisional term, and u is the velocity of the collisional partners.

Considering the Ohm's law $\mathbf{J} = \sigma(\mathbf{E} + \mathbf{v} \times \mathbf{B})$ where σ is the conductivity and J is the current density, and the magnetized case where the plasma may move with velocity v across the magnetic field B and in steady state the equation of motion turns out:

$$\mathbf{E} + \mathbf{v}_e \times \mathbf{B} = -\frac{m_e\nu_c}{e}\mathbf{v}_e \tag{3.21}$$

Define the Equation 3.21 in terms of the conductivity, which will yield:

$$\mathbf{J} = \sigma\mathbf{E} - \frac{\sigma}{n_e e}\mathbf{J} \times \mathbf{B} \tag{3.22}$$

Consider the magnetic field aligned with z axis, so $\mathbf{B} = B\hat{e}_z$ and consider the $\omega_e = \frac{eB}{m}$ to get:

$$J_x = \sigma E_x + \frac{\omega_e}{\nu_c}J_y \tag{3.23}$$

$$J_y = \sigma E_y - \frac{\omega_e}{\nu_c}J_x \tag{3.24}$$

$$J_z = \sigma E_z \tag{3.25}$$

Combining Equation 3.23 and Equation 3.24 to eliminate J_y from the first and J_x from the second equation yields:

$$J_x = \frac{\nu_c^2}{\nu_c^2 + \omega_e^2}\sigma E_x + \frac{\omega\nu_c}{\nu_c^2 + \omega_e^2}\sigma E_y \tag{3.26}$$

$$J_y = \frac{\nu_c^2}{\nu_c^2 + \omega_e^2}\sigma E_y - \frac{\omega\nu_c}{\nu_c^2 + \omega_e^2}\sigma E_x \tag{3.27}$$

$$J_z = \sigma E_z \tag{3.28}$$

This set of equations can be written in dyadic notation, as follows:

$$\mathbf{J} = \sigma \cdot \mathbf{E} \tag{3.29}$$

For a magnetic field line aligned with the z direction, the conductivity becomes:

$$\sigma = \begin{pmatrix} \sigma_P & -\sigma_H & 0 \\ \sigma_H & \sigma_P & 0 \\ 0 & 0 & \sigma_\parallel \end{pmatrix} \tag{3.30}$$

where σ_P, σ_H, and $\sigma_\parallel$ are refers to Pedersen conductivity, Hall conductivity, and Parallel conductivity.

$$\sigma_P = \frac{\nu_c^2}{\nu_c^2 + \omega_e^2}\sigma \tag{3.31}$$

$$\sigma_H = -\frac{\omega_e \nu_c}{\nu_c^2 + \omega_e^2}\sigma \tag{3.32}$$

$$\sigma_\parallel = \sigma = \frac{n_e e^2}{m_e \nu_c} \tag{3.33}$$

Finally, the magnetic field has an arbitrary angle to the axes x and y. The dyadic Equation 3.29 becomes:

$$\mathbf{J} = \sigma_\parallel \mathbf{E}_\parallel + \sigma_P \mathbf{E}_\perp - \sigma_H \frac{\mathbf{E}_\perp \times \mathbf{B}}{B} \tag{3.34}$$

(BAUMJOHANN; TREUMANN, 1996) determines the Pedersen conductivity which governs *Pedersen current* in the direction of the electric field $E_\perp$, determines Hall conductivity which governs *Hall current* in the direction perpendicular to both the electric and magnetic field, in the $-E \times B$ direction. And also defines the parallel conductivity which governs the magnetic *Field-aligned current* driven by the parallel electric field component $E_\parallel$.

In particular, the *Field-aligned current* flows parallel to the magnetic field into and out of the Ionosphere, besides that, the *Pedersen current* flows perpendicular to the magnetic fields and parallel to the ionospheric convection field. Finally, *Hall current* flow perpendicular to both the magnetic field and the electric field. Those currents

are shown in Figure 3.5. At high latitudes, where the field lines are nearly vertical,

Figure 3.5 - Birkeland Currents.

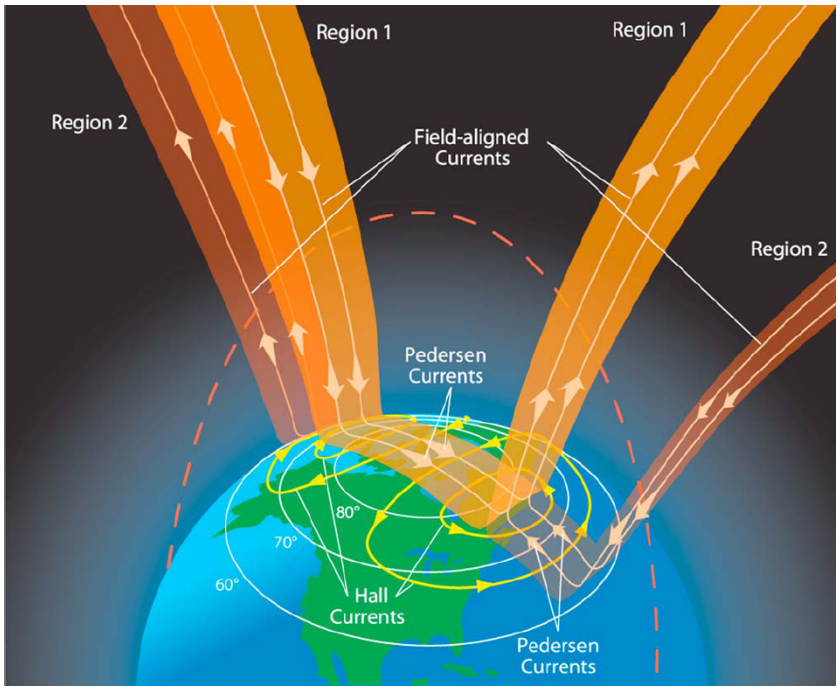

SOURCE: Potemra (1983).

the horizontal electric field becomes almost *height-independent* Baumjohann and Treumann (1996) producing *height-integrated* quantities, as follows:

$$\Sigma_P = \int \sigma_P dz \tag{3.35}$$

$$\Sigma_H = \int \sigma_H dz \tag{3.36}$$

$$J_\perp = \int j_\perp dz \tag{3.37}$$

The height-integrated conductivities or *conductances* and the height-integrated horizontal current density are related through the height-integrated version of Ohm's law, as follows:

$$\mathbf{J}_\perp = \Sigma_P \mathbf{E}_\perp - \Sigma_H \frac{(\mathbf{E}_\perp \times \mathbf{B})}{B} \tag{3.38}$$

The neutral wind is important at low and mid-latitudes, but at high latitudes is much weaker than the motion due to the convection electric field Baumjohann and Treumann (1996), as a consequence, the neutral wind is neglected from Equation 3.38.

The field-aligned current should be computed under the assumption that the total current flow must be continuous, using the divergence of the height-integrated horizontal current, as follows:

$$J_{\parallel} = \nabla_{\perp} \cdot \mathbf{J}_{\perp} \tag{3.39}$$

where $\nabla_{\perp}$ denotes the vector derivative in the horizontal plane, using Equation 3.38 in Equation 3.39 to becomes:

$$J_{\parallel} = (\nabla_{\perp}\Sigma_P) \cdot \mathbf{E}_{\perp} - (\nabla_{\perp}\Sigma_H) \cdot \frac{(\mathbf{E}_{\perp} \times \mathbf{B})}{B} + \Sigma_P(\nabla_{\perp} \cdot \mathbf{E}_{\perp}) \tag{3.40}$$

The *field-aligned currents* are generated at gradients of the Pedersen conductance along the electric field direction, at a gradient of the Hall conductance which is aligned perpendicular to the horizontal electric field, and in regions where the divergence of the electric field is non-zero (BAUMJOHANN; TREUMANN, 1996).

Ionospheric currents may heat the atmosphere by Ohmic dissipation or *Joule Heating*. The Joule Heating is proportional to the current flowing parallel to the electric field (BAUMJOHANN; TREUMANN, 1996). The height-integrated Joule heating rate can be written as:

$$Q_J = \mathbf{J}_{\perp} \cdot \mathbf{E}_{\perp} \tag{3.41}$$

Since the Hall currents flow perpendicular to the electric field, they do not contribute to Ohmic dissipation, as a consequence Equation 3.41 becomes:

$$Q_J = \Sigma_P E_{\perp}^2 \tag{3.42}$$

4 THE MAGNETOHYDRODYNAMICS MODELLING

This chapter presents the formalisms of the magnetohydrodynamics (MHD) model applied in order to describe the dynamo of the space electrodynamics phenomena studied in this work. Furthermore, there is a brief description of the solver, developed in Moreira Lopez (2019), for the MHD equations implemented into the AMROC framework. Then, the formulation and the configuration of the magnetosphere simulation for 2D are described. Lastly, this chapter introduces a probing tool for the AMROC framework, developed in this work, in order to collect and register data at points of interest during the magnetosphere simulations.

4.1 Magnetohydrodynamic model

In the context of studying the space plasma in the near-Earth region, the MHD model is a suitable choice to describe its phenomena. Briefly, this model describes the plasma dynamo as a single and magnetized fluid. This formulation prioritizes the macroscopic effects of the plasma physics while neglecting microscopic effects, in order to build a simulate a computationally simpler model that can be solved under reasonable CPU times. This choice can also be justified considering the very large scale of the phenomena of interest in magnetosphere studies.

In particular, this work presents two formulations for the MHD equations: the ideal MHD and a resistive MHD model. These formulations differ by the treatment over the dissipation of magnetic field lines, so the ideal model neglects this phenomenon and consequently has frozen magnetic field lines, while the resistive model is capable of representing magnetic reconnection phenomena.

4.1.1 Ideal MHD

As mentioned by Baumjohann and Treumann (1996), the ideal MHD is the simplest representation of the plasma as a conductivity fluid. This formulation is an adiabatic process that neglects dissipative effects such as resistivity, viscosity, and heat flux.

Hence, with the ideal MHD formulation, the plasma conserves the physical properties of mass, momentum, energy, helicity, and the magnetic field topology due to the absence of such dissipation. Taking into consideration these assumptions, the following equations are formulated, as described in (BAUMJOHANN; TREUMANN, 1996):

$$\frac{\partial \rho}{\partial t} + \nabla \cdot (\rho \mathbf{u}) = \mathbf{0}\,, \tag{4.1}$$

$$\frac{\partial(\rho\mathbf{u})}{\partial t} + \nabla \cdot \left[\rho\mathbf{u}\mathbf{u} + \left(p + \frac{\mathbf{B}\cdot\mathbf{B}}{2}\right)\mathbb{I} - \mathbf{B}\mathbf{B}\right] = \mathbf{0}\,, \tag{4.2}$$

$$\frac{\partial\mathcal{E}}{\partial t} + \nabla \cdot \left[\left(\mathcal{E} + p + \frac{\mathbf{B}\cdot\mathbf{B}}{2}\right)\mathbf{u} - (\mathbf{u}\cdot\mathbf{B})\mathbf{B}\right] = \mathbf{0}\,, \tag{4.3}$$

$$\frac{\partial\mathbf{B}}{\partial t} + \nabla \cdot [\mathbf{u}\mathbf{B} - \mathbf{B}\mathbf{u}] = \mathbf{0}\,, \tag{4.4}$$

where this system is completed with the internal energy equation, given by the combination of the hydrodynamic and magnetic energies:

$$\mathcal{E} = \frac{p}{\gamma - 1} + \rho\frac{\mathbf{u}\cdot\mathbf{u}}{2} + \frac{\mathbf{B}\cdot\mathbf{B}}{2}\,, \tag{4.5}$$

so that γ is the polytropic index.

This formulation, called *conservative form*, describes the evolution of physical quantities, that in the absence of dissipative effects, should be conserved.

It is worth mentioning that considering the MHD model presented in this Chapter 4, can be obtained using the conservative variables $\mathbf{q}(\mathbf{r}, t) = (\rho, \rho\mathbf{u}, \mathcal{E}, \mathbf{B}_\perp)$ as presented in equations 4.1 which comes after take the Boltzmann's moments.

Moreover, the numerical methods for the simulation of the MHD model require the eigenvalues associated with each spatial derivative of the system, in other words, require the system in an advection equation. However, the terms of the conservative MHD equations can not be expressed in this formulation. Thus, the system of equations is rewritten in the primitive formulation. The primitive formulation describes the MHD equations based on the vector of variables $\mathbf{w} = (\rho, p, u_x, u_y, u_z, B_x, B_y, B_z)$.

The system of equations that governs the MHD model using primitive variables is obtained by reordering the terms of the conservative formulation, except for the energy equation. Under the fact mentioned before, this work used primitive variables as initial and boundary conditions.

4.1.2 Resistive MHD

As mentioned by Baumjohann and Treumann (1996), the resistive MHD is a more realistic description of the plasma that is get by considering the resistive effects obtained in the energy and induction equation. The diffusion of the magnetic field lines presented in this resistive model grants a new range of phenomena that is not possible to explain with the ideal MHD.

Despite the great approximation reached with this approach, the resistive MHD increases both theoretical and computational efforts to research plasma, as a consequence, the resistive formulation is applied when its effects are significant, for example, to get magnetic reconnection.

The importance of the resistive effects is governed by the magnetic Reynolds number R_m defined by:

$$R_m := \frac{\mathcal{U}\mathcal{L}}{\eta}\,, \tag{4.6}$$

where $\mathcal{U}$, $\mathcal{L}$, and η are the typical velocity, the characteristic length scale of the flow, and the resistivity. The magnetic Reynolds number is a dimensionless number that represents the ratio between the magnitude of the advective and diffusive effects. As a consequence, a low magnetic Reynolds number ($R_m << 1$) represents a medium governed by the resistive effects. In contrast, a high magnetic Reynolds number ($R_m >> 1$) implies a medium dominated by the advective effects, which is prevalent in most of the space environment.

Thus, the resistive MHD model is governed by the following equations in the conservative form:

$$\frac{\partial \rho}{\partial t} + \nabla \cdot (\rho \mathbf{u}) = \mathbf{0}\,, \tag{4.7}$$

$$\frac{\partial (\rho \mathbf{u})}{\partial t} + \nabla \cdot \left[\rho \mathbf{u}\mathbf{u} + \left(p + \frac{\mathbf{B}\cdot\mathbf{B}}{2}\right)\mathbb{I} - \mathbf{B}\mathbf{B}\right] = \mathbf{0} \tag{4.8}$$

$$\frac{\partial \mathcal{E}}{\partial t} + \nabla \cdot \left[\left(\mathcal{E} + p + \frac{\mathbf{B}\cdot\mathbf{B}}{2}\right)\mathbf{u} - (\mathbf{u}\cdot\mathbf{B})\mathbf{B} + (\eta \mathbf{J}) \times \mathbf{B}\right] = \mathbf{0}\,, \tag{4.9}$$

$$\frac{\partial \mathbf{B}}{\partial t} + \nabla \cdot [\mathbf{u}\mathbf{B} - \mathbf{B}\mathbf{u} + \eta((\nabla \mathbf{B})^T - \nabla \mathbf{B})] = \mathbf{0} \tag{4.10}$$

4.2 AMROC framework: module MHD

The framework AMROC (Adaptive Mesh Refinement in Object-oriented C++) was conceived as a platform to perform the numerical simulation of partial differential equations using the finite volumes methods, while applying high-performance strategies, such as adaptive grids and parallel programming using the Message Passing Interface (MPI) protocol (DEITERDING et al., 2016).

For that, it implements a special version of the Structured Adaptive Mesh Refinement (SAMR) algorithm proposed in Berger and Colella (1989) using object-oriented programming in the C++ language alongside some FORTRAN routines for grid operations to improve its computational performance (DEITERDING et al.,

2016).

This framework is available on the webpage http://amroc.sourceforge.net/index.htm, which contains the installation, compilation, and running guides. It consists of about 46 thousand lines of code in the C++ language and more than 6 thousand lines for visualization and data conversion routines, including running scripts to convert the output HDF (Hierarchical Data Format) files into binary VTK (Visualization Toolkit) files used for the data visualization in software such as VisIt Childs et al. (2012), available in https://visit-dav.github.io/visit-website/releases-as-tables/, and ParaView Ahrens et al. (2005), available in https://www.paraview.org/download/.

In particular, the adaptive strategy implemented in the AMROC consists in applying a numerical operator over the studied solution after every time step in order to flag cells of the discretized domain that match some criteria, such as steep gradients. Then, the SAMR algorithm is capable of clustering these flagged cells into regions of interest that will be overlayed by a more refined subgrid. This approach allows the computational efforts, consequently the accuracy of the solution, to be more concentrated in these regions of interest. Consequently, solutions with higher precision can be obtained under a reasonable CPU time, which most would not be feasible for a simulation of higher precision in the entire computational domain.

In recent years, from the collaboration of the INPE team with the AMROC's creator, the framework was further extended to support wavelet-based operations, based on the adaptive multiresolution method proposed in Harten (1994), to perform the flagging of the grid elements alongside with the grid operations between different refinement levels (DOMINGUES et al., 2019b).

In its conception, the AMROC framework presents a generic procedure to solve a hyperbolic system of partial differential equations using the mentioned strategies. Then, this generic solver is integrated with a particular set of equations by its module. Recently, the framework was updated to perform MHD simulations using the ideal and resistive model (DOMINGUES et al., 2019a; Moreira Lopez, 2019). Later, in Péron et al. (2021), this implementation is further detailed alongside with early results of the 2D magnetosphere simulations using a dataset collected via satellite as the Solar wind.

These simulations, besides their high processing and storage demands, have an inherent challenge concerning the formation of magnetic monopoles, appearing as di-

vergence components in the magnetic field, due to numerical errors that occur during the simulations (BRACKBILL; BARNES, 1980). This non-physical behavior must be treated using a numerical strategy that eliminates or mitigates the propagation of these divergence components.

Several numerical strategies were developed to handle this divergence problem, but the best solution is still an open problem (FENG, 2019), for instance, comparative studies among some popular techniques were presented in Hopkins (2016) and Miyoshi and Kusano (2005).

The MHD module from AMROC implements several strategies to solve the divergence problem. These strategies are all based on the Generalized Lagrange Multiplier (GLM) formulation using a parabolic-hyperbolic correction, originally proposed in Munz et al. (2000) for Maxwell Equations, and adapted for MHD in Dedner et al. (2002). Currently, the MHD module can perform the parabolic-hyperbolic correction using the traditional GLM strategy (DEDNER et al., 2002); the Extended GLM (EGLM) strategy, which combines the GLM methodology with Powell's 8-wave source terms (POWELL et al., 1999); and the GLM triple-correction proposed by Moreira Lopez (2019), which combines the parabolic-hyperbolic and elliptic operators of the GLM approaches presented in Dedner et al. (2002). In parallel to this work, our research group is currently working on the implementation of the Ideal GLM (IGLM) strategy proposed by Derigs and Winters (2018), which is focused on treating the problem's entropy to enforce its thermodynamics consistency. From the perspective of a user, the AMROC framework is divided into two main folders, the implementation and compilation folders, as presented in Figure 4.1. In addition, the AMROC framework contains other folders that are relevant for installation procedures and data structures, but they are omitted here.

The implementation folder, which is downloaded from the repository, contains the AMROC source code and includes both the generic solver and the modules. On the other hand, the compilation folder contains scripts and executables and is constructed during the AMROC installation process.

The implementation module contains the generic SAMR solver in the folder *amr*, while macros and data structures are defined in the *hds* folder, omitted in the diagram of Figure 4.1. Alongside these folders, the modules for each particular physical problem are presented at the same level. In this diagram, only the *mhd* module is being shown, while the others such as *lbm*, for Lattice-Boltzmann methods, are omitted.

Figure 4.1 - AMROC folder hierarchy.

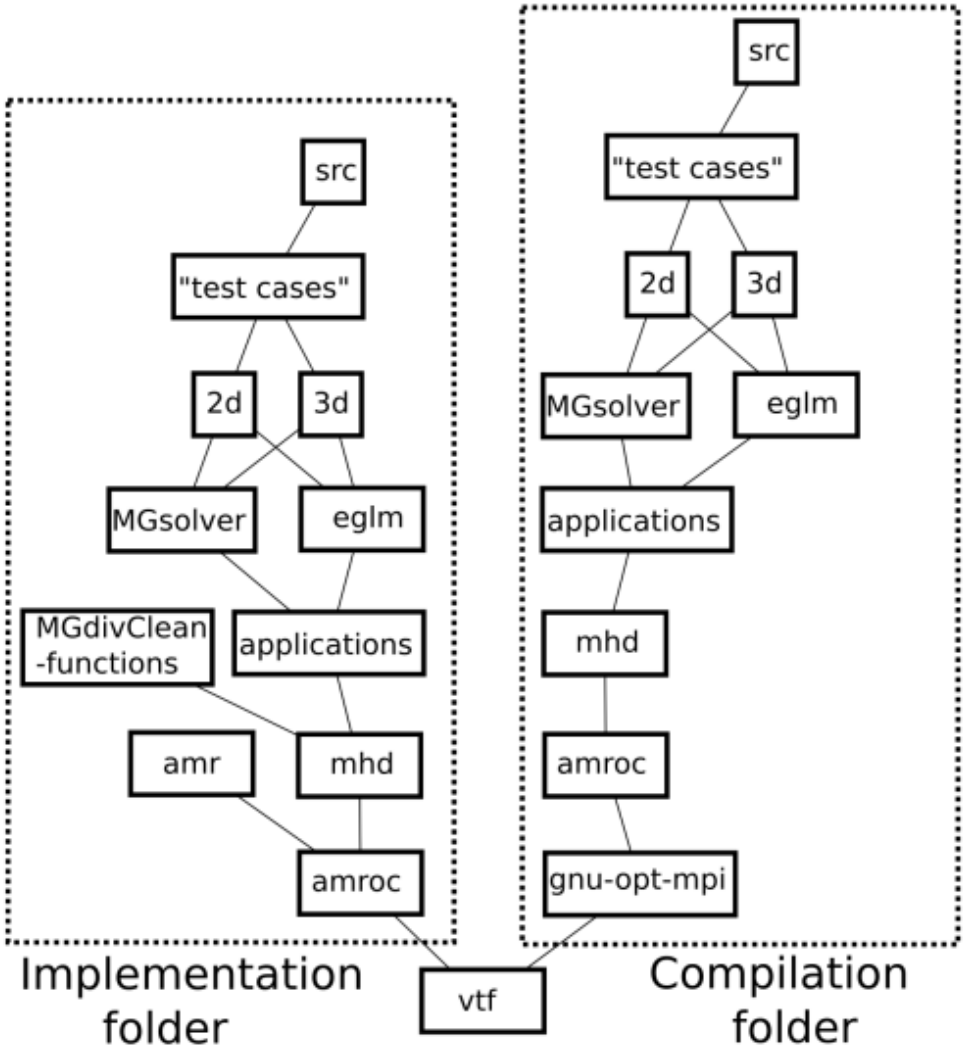

SOURCE: Moreira Lopez (2019).

In particular, the *mhd* folder contains the functions that integrate the MHD equations in the generic SAMR solver. Furthermore, almost at the end of the sequence of subfolders following the folder *applications*, the *"test cases"* folders contains the definition of the simulation parameters, such as the choice of numerical schemes, final time, boundary conditions, grid refinement, etc. The final folder *src* contains the initial conditions and, if existent, some physical particularities of the problem, such as the extra source terms for the magnetosphere simulation.

The path from the folder *applications* to the *"test cases"*, aims to divide the problems

by divergence cleaning approach and the number of dimensions. For instance, the folders *MGsolver* and *eglm* contain problems to be solved with the triple correction from Moreira Lopez (2019) and the EGLM formulation respectively. This Diagram omits the *glm* and *iglm* folders that follow the same logic. These folders divide the implemented test cases into sub-folders for the two and three-dimensional problems. The magnetosphere simulation explained in the next section is one of these implemented cases.

During the installation, the Compilation folder is built in order to mimic the same hierarchy of folder of each module, so that the *makefile* scripts to compile each problem are located inside its correspondent *"test cases"* folder. Furthermore, at the same level as the modules, the compilation folder has the *bin* folder (omitted in the diagram) which stores the executables and other useful scripts.

Besides the AMROC, the literature presents further MHD codes capable of solving these equations with high performance. To allow characteristics comparisons, survey results of other magnetohydrodynamics frameworks are available in *Appendix A*.

Additional information could be obtained in Feng (2019). To facilitate the AMROC-MHD contextualization, Table 4.1 shows a summary of the main MHD code characteristics based on the purpose similarities, i.e. code for studies on Space plasma phenomena.

In the current efforts, the computational simulations have been obtained from a machine presenting the following characteristics:

- GNU/Linux Mint 20 Operation System.
- Storage of 1 TB and 24 GB of RAM.
- 0.8 GHz with 4 cores per socket which is in total 8 available cores.

For future usages, the simulations required by this project will evolve and be performed using the HPC-CEA[1], located at the Embrace, CEA-II building, in the 1st. floor. Their characteristics are:

- Two processors Intel Xeon, $E5-2660v2$ model, 10 cores of processors, 2.20 GHz with 220 available cores for a simulation.

[1]Information on the HPC can be found at: http://mtc-m21c.sid.inpe.br/col/sid.inpe.br/mtc-m21c/2020/01.13.16.49/doc/publicacao.pdf

Table 4.1 - Summary of the MHD codes.

Code	**Physics**	**Divergence cleaning**	**Optimization**	**Application**
AMROC	Ideal MHD, resistive MHD	GLM	Parallelization with MPI, AMR and MR adaptivity	Magnetosphere, Ionosphere, shocks
RAMSES	Ideal MHD, radiative transfer	Constrained Transport	Parallelization with MPI, AMR	cosmological simulations, star formation and supernovae-driven winds
ATHENA	Ideal MHD, relativistic hydrodynamics, Self-gravity, and a static gravitational potential	Constrained Transport	Parallelization with MPI	MHD clouds, binaries wind
BATS-R-US	Ideal MHD, semi-relativistic and Hall MHD	Constrained Transport, projection, parabolic-hyperbolic cleaning	Parallelization with MPI	Alfvén wave turbulence, ring current, magnetosphere
GAMERA	Ideal MHD, resistive MHD	Constrained Transport	Parallelization with MPI	Magnetosphere, Ionosphere, ring current and inner heliosphere

- 768 GB of RAM and 18666 GHz per node.
- Storage of 75.6 TB and 1.2TB per SAS disk.
- Each GPU has 2496 CUDA cores, 5 GB of RAM GDDR5, and a bandwidth of 208 GB.

4.3 Magnetosphere simulation

This Section is dedicated to describing the magnetosphere numerical experiment that serves as a foundation for the discussions proposed in this work. In particular, this experiment will be discussed in its 2D configuration alongside its initial setup, boundary conditions, and internal boundary conditions to approximate the

ionosphere-magnetosphere dynamics, the normalization, and the solar wind.

4.3.1 Magnetosphere simulation in 2D

To allow appropriate code learning and, at the same time, contribute to the development of new resources (probes) in the AMROC, a bi-dimensional magnetosphere simulation will be performed.

With that purpose, this work utilizes the initial and boundary conditions proposed in Ogino et al. (1992) where consider the Earth as a sphere with constant density and pressure in time, besides that, contains a magnetic dipole that will be compressed or stretched by the solar wind. Due to the interaction of the solar wind being simulated the magnetic reconnection considers IMF to be northward or southward.

The model proposed by Ogino et al. (1992) requires new parameters, for example, the acceleration term $\mathbf{a}$ that includes an external gravity field.

$$\mathbf{a} = \frac{q_\alpha}{m_\alpha}(\mathbf{E} + \mathbf{v} \times \mathbf{B}) + \mathbf{g} \tag{4.11}$$

and Ampere's law is rewritten as:

$$\mathbf{J} = \nabla \times (\mathbf{B} - \mathbf{B_d}), \tag{4.12}$$

where $\mathbf{B_d}$ is the intrinsic dipole magnetic field of the Earth. The reason for subtracting the dipole field from Ampere's law is to allow the electric current to be generated in the frontier between the two mediums (interplanetary space and the outer terrestrial region).

Moreover, Ogino (1986) introduces a viscosity term $\Phi = 10^{-5}\nabla^2\mathbf{u}$ and an artificial diffusion over ρ and p to the model. These effects are included in order to reduce the MHD fluctuations which come from unbalanced forces at the initial state. That is, the numerical oscillations on the scale of the mesh size decrease in front of the bow shock when it includes the viscosity and diffusion terms (OGINO, 1986). In this work, the MHD is presented in the primitive formulation.

Finally, in Moreira Lopez (2019), this modeling is adapted and implemented in the AMROC framework by the system of equations in a semi-conservative formulation:

$$\frac{\partial \rho}{\partial t} + \nabla \cdot (\rho \mathbf{u}) = D\nabla^2\rho \tag{4.13}$$

$$\frac{\partial(\rho\mathbf{u})}{\partial t} + \nabla\cdot\left[\rho\mathbf{u}\mathbf{u} + \left(p + \frac{\mathbf{B}.\mathbf{B}}{2}\right)\mathbf{I} - \mathbf{B}\mathbf{B}\right] = \rho\mathbf{g} + \mathbf{B}\times(\nabla\times\mathbf{B_d}) + \Phi + \mathbf{u}D\nabla^2\rho \tag{4.14}$$

$$\begin{aligned}\frac{\partial\mathcal{E}}{\partial t} + \nabla\cdot\left[\left(\mathcal{E} + p + \frac{\mathbf{B}.\mathbf{B}}{2}\right)\mathbf{u} - (\mathbf{u}.\mathbf{B})\mathbf{B} + (\eta\nabla\times\mathbf{B})\times\mathbf{B}\right] \\ = \rho\mathbf{u}\cdot\mathbf{g} + \eta||\nabla\times\mathbf{B_d}||^2 + (\nabla\times\mathbf{B_d})\cdot(\mathbf{u}\times\mathbf{B} - \eta\nabla\times\mathbf{B}) \\ + \frac{D_p\nabla^2 p}{\gamma - 1} + \frac{||u||^2}{2}D\nabla^2\rho + \mathbf{u}\cdot\Phi\end{aligned} \tag{4.15}$$

$$\frac{\partial\mathbf{B}}{\partial t} + \nabla\cdot[\mathbf{u}\mathbf{B} - \mathbf{B}\mathbf{u} + \eta((\nabla\mathbf{B})^T - \nabla\mathbf{B} - (\nabla\mathbf{B_d})^T + \nabla\mathbf{B_d})] = 0\,, \tag{4.16}$$

where the terms in red are deduced from the gravity term included in the particle acceleration $\mathbf{a}$ and the dipole $\mathbf{B_d}$ from the Ampere's law, besides that, the terms written in blue correspond to the viscosity and artificial diffusion as introduced by Ogino (1986). The diffusion terms use the constants $D = D_p = 0.002$.

In this experiment, the physical quantities are normalized so that the unit of distance corresponds to $1r_E$ (6.37×10^6m), the unit of magnetic induction corresponds to the Earth's magnetic field at the equator (3.12×10^{-5}T) and the time unit corresponds to the Alfvén transit time (0.937s), defined as the time required by the Alfvén wave to go through the equivalent of the Earth radius.

Based on these quantities, the pressure unit corresponds to $7.75\times10^{-4}N/m^2$, the velocity unit corresponds to $6.80\times10^6 m/s$, the acceleration unit corresponds to $7.26\times10^6 m/s^2$ and the current density unit corresponds to $3.90\times10^{-6}A/m^2$.

The initial configuration of some of the physical quantities included in the model is proportional to the distance to Earth, depicted by ξ. Assuming the Earth located in the xy plane origin, the distance ξ is defined as:

$$\xi = \sqrt{x^2 + y^2}\,. \tag{4.17}$$

Thus, the external gravity $\mathbf{g}$, defined by the vector field:

$$\mathbf{g}(x,y) = -\frac{g_0}{\xi^2}\begin{bmatrix}x\\y\\0\end{bmatrix}\,, \tag{4.18}$$

where $g_0 = 1.35\times10^{-6}$, corresponding to $9.8m/s^2$ in the discussed normalization,

and the line dipole magnetic field $\mathbf{B_d}$ is given by:

$$\mathbf{B_d}(x,y) = \begin{bmatrix} B_{d_x} \\ B_{d_y} \\ B_{d_z} \end{bmatrix} = \begin{bmatrix} -2xy\xi^{-4} \\ \xi^{-4}(x^2 - y^2) \\ 0 \end{bmatrix}, \tag{4.19}$$

which corresponds to a dipole magnetic field with the magnitude 1 in its equator, therefore already compatible with the proposed normalization.

The resistivity term η is defined as:

$$\eta(x,y) = \eta_0 \left(\frac{T}{T_0}\right)^{-\frac{3}{2}}, \tag{4.20}$$

with $\eta_0 = 10^{-2}$, $T = \frac{p}{\rho}$ and $T_0 = 5.4 \times 10^{-7}$ in its normalised values.

Initial Conditions

The initial configuration for this problem consists in a steady-state ionosphere which describes the plasma in the Earth's neighborhood. This ionosphere is constructed so that its pressure and density are proportional to ξ, while the initial magnetic field is the dipole presented in Equation 4.19 (OGINO, 1986). Thus, the ionosphere's initial condition is given by:

$$\mathbf{q}^0(x,y) = \begin{bmatrix} \rho \\ p \\ u_x \\ u_y \\ u_z \\ B_x \\ B_y \\ B_z \end{bmatrix} = \begin{bmatrix} max(\xi^{-2}, 10^{-4}) \\ max(p_{00}\xi^{-1}, 3.56 \times 10^{-8}) \\ 0 \\ 0 \\ 0 \\ B_{d_x} \\ B_{d_y} \\ B_{d_z} \end{bmatrix} \tag{4.21}$$

where $p_{00} = \frac{(\gamma-1)g_0}{\gamma} = 5.4 \times 10^{-7}$ for $\gamma = 2$. This configuration describes a decaying value for ρ and p from the Earth until a threshold value that represents the initial value of the interplanetary region.

Boundary Conditions

This problem is simulated inside the physical domain $[-150, 450] \times [-150, 150]$, which is complemented with Neumann boundary conditions so that the derivative of the

physical quantities are zero at the boundaries $x_e = 450$, $y_s = -150$ and $y_e = 150$. The boundary at $x_s = -150$ inputs the solar wind parameters.

Furthermore, the physical domain also presents an internal boundary corresponding to the near-Earth region. Considering the Earth positioned at the origin, this internal boundary removes the points which $\xi < 16$ from the computational domain (OGINO et al., 1992). In order to damp out all perturbations near the ionosphere, the near-Earth neighborhood is smoothed in relation to the initial condition after every time step by the operation:

$$\mathbf{q}^{n+1} = f\mathbf{q}_*^{n+1} + (1-f)\mathbf{q}^0\,, \tag{4.22}$$

where $\mathbf{q}_*^{n+1}$ is the solution obtained after the time evolution and $\mathbf{q}^0$ is the ionospheric initial condition. The weight value f is computed as:

$$\bar{f} = 100\left(max\left[\left(\frac{\xi}{16}\right)^2 - 1, 0\right]\right)^2 \tag{4.23}$$

$$f = \frac{\bar{f}^2}{\bar{f}^2 + 1} \tag{4.24}$$

Solar wind setup

Defined the initial state of the ionosphere and the near-Earth boundary condition, the magnetosphere is configured by introducing the solar wind as the boundary condition in $x_s = -150$. In this work, the configuration of the magnetosphere is performed in two steps.

The first step sets the solar wind boundary condition using typical normalized values. For instance, considering that the solar wind dataset to be studied starts with a north-oriented magnetic field, the value B_y in the solar wind is initialized as positive. On the other hand, negative values for this B_y are assumed for datasets that initialize with south-oriented magnetic fields.

This procedure is done until a predefined setup time t_{set} using the following param-

eters:

$$\mathbf{q}(x_s, y, t < t_{set}) = \begin{bmatrix} \rho \\ p \\ u_x \\ u_y \\ u_z \\ B_x \\ B_y \\ B_z \end{bmatrix} = \begin{bmatrix} 5 \times 10^{-4} \\ 3.56 \times 10^{-8} \\ 4.41 \times 10^{-2} \\ 0 \\ 0 \\ 0 \\ 1.5 \times 10^{-4} \\ 0 \end{bmatrix}, \tag{4.25}$$

where $t_{set} = 138313.5$ corresponds to the one-and-a-half day in the normalized time. This step is expected to balance the magnetic and hydrodynamic components of the magnetosphere until a semi-steady state.

The second step corresponds to the interval between this first setup and the instant in which the dataset is actually included, i.e. $t_{mag} = 184418$, corresponding to two days in the normalized time. In this step, the solar wind parameters are updated each time step with a linear interpolation between the presented typical values and the first entries of the dataset to be studied. This is done in order to continually create a magnetosphere setup to receive the solar wind data in its correct magnitude, avoiding the creation of artificial shockwaves due to the change of values in the solar wind.

The mentioned datasets used as solar winds are collected via satellite and acquired in the Omni-NASA service (`https://omniweb.gsfc.nasa.gov/html/omni_source.html`). These datasets are filtered using Hermite interpolation (which guarantees a smoothed first derivative) to fill the gaps and a discrete wavelet with six frequency-band components to smooth the data, as seen in Section 6.1.

Configured the semi-steady state of the magnetosphere, the magnetosphere simulation starts using the filtered dataset as boundary conditions at x_s.

5 SIMULATION PROBES: IMPLEMENTATION AND VERIFICATION

This chapter presents the implementation of a tool, developed in this work, for the AMROC framework, with the purpose of generating complementary information for the analysis of the simulations, especially the magnetosphere experiments

This tool consists of a computational resource for probing the numerical solutions in both 2D and 3D simulations to get information in regions of interest, for example, considering magnetosphere simulations, alongside the magnetopause, plasmasheet, in the X-region of the magnetotail when a magnetic reconnection is happening, or even over the polar cap to get information about the R1 and R2 regions of the FAC.

The usage of this probe will allow the extraction of temporal profiles, for every physical quantity, in the regions of interest without compromising the simulation time with unnecessary full grid outputs and post-processing.

5.1 Probe tool implementation

Currently, the probe developed is implemented in the files **Probe2D.h** and **Probe3D.h** inside the directory **mhd** as shown in Figure 4.1, as a library of functions that are included in the **Solver** class, which controls the generic SAMR algorithm, according to the number of dimensions of the problem. In general, the basic algorithm of probe sampling is defined by the following instructions:

- The **Trajectory** function is responsible to return the cartesian coordinates of the probe given any current time instant. These coordinates can be calculated via some predefined parametric equations; via the interpolation of a dataset with the probe coordinates over time; or by searching a physical property, such as the Bow shock in Magnetosphere simulations.
- With the probe current coordinates, the **TrackProbe** function locates the Probe inside the SAMR data structure and stores the solution at the desired position.
- In adaptive simulations, in order to extract the solution with the highest refinement possible, the probe searches the solution from the finest grids to the coarsest grids.
- This search is performed by using a macro that traverses all the subgrids starting with the finest ones. For each subgrid, the position of the limits of

its physical boundaries is checked in order to verify if the Probe coordinates is positioned inside it.

- Once the patch that contains the probe is found, a set of loops is applied to search the exact cell where the Probe is contained.
- As long as the Probe is found, the **qfinal** variable receives the solution in the current subgrid, then the macro is ended and the solution is shared with the other MPI processes.
- In order to avoid repeated values in the output file, MPI modification was done to ensure that just process **0** is capable of printing the collected values.

The probe implementation depends on several user-defined keys that are inserted in the file **solver.in**, which contains the simulation parameters and numerical schemes to be applied, and it is read during the run time.

These keys are set to control the following instances:

- Activation / Deactivation of the probe sampling during this simulation.
- Configuration of how the probe trajectory is obtained, by a parametric equation, by interpolating a dataset, or by locating a physical property. Currently, the only physical property implemented is the nose of the Bow shock in the magnetosphere and shock-cloud experiments.
- If the previous key is set for the bow shock nose, a key is also defined to choose the positioning of the Probe in relation to the physical property, *i.e.*, three cells to the right, three cells to the left, or in the center of the bow shock.
- Select if the sampling will be performed after every predefined time interval, or if this time interval is calculated specifically to force the final output dataset to have a predefined number of samples.

In order to perform the initial verification tests developed first by Dedner et al. (2002) and adapted by Moreira Lopez (2019) in the AMROC framework, a battery of tests was prepared for the current two-dimensional probe implementation. In these

tests, the probe traverses a solution with expected behaviors in order to verify if it collects a dataset that matches the expected results.

These batteries of tests were performed using an initial condition also described in Dedner et al. (2002) that configures a Kelvin-Helmholtz instability (KHI). The configuration described in that work occurs in single continuous fluids with a velocity shear.

The simulations are performed inside the computational domain $[0, 1] \times [-1, 1]$ with periodic boundaries and an initial condition given according to the adiabatic constant $\gamma = 1.6$ as:

$$\mathbf{q}^0(x, y) = \begin{bmatrix} \rho \\ p \\ u_x \\ u_y \\ u_z \\ B_x \\ B_y \\ B_z \end{bmatrix} = \begin{bmatrix} 1 \\ 50 \\ 5\left[\tanh\left[20(y+0.5)\right] - \tanh\left(20(y-0.5)\right) - 1\right] \\ 0.25\sin\left(2\pi x\right)\left(e^{-100(y+0.5)^2} - e^{-100(y-0.5)^2}\right) \\ 0 \\ 1 \\ 0 \\ 0 \end{bmatrix} \tag{5.1}$$

until the final time $t = 0.5$.

For these tests, the following simulation parameters were applied: HLLD Riemann solver Miyoshi and Kusano (2005) combined with an MC limiter. The parabolic-hyperbolic correction uses the factor $\alpha_p = 0.5$. The Courant number (CFL) is set $\sigma = 0.4$.

5.1.1 Test 1: sampling from a fixed solution

In this test, the initial condition from the KHI problem is fixed over time, while the probe traverses the solution following the circular trajectory defined by:

$$x(t) = 0.5 + 0.2cos\left(\frac{2\pi t}{0.1}\right) \tag{5.2}$$

$$y(t) = 0.5 + 0.2sin\left(\frac{2\pi t}{0.1}\right) \tag{5.3}$$

As the orbit period is set as 0.1, the probe will perform five cycles during the simulation.

Defining this orbit as parametric equations, Figure 5.1 presents the dataset collected

by the probe for the variable u_x. Alongside this plot, for comparison, this figure presents another plot with the expected solution to be collected. The fact that these plots are identical indicates that the probe properly collected the solution.

Figure 5.2 presents the same output. However, the probe trajectory is defined by the interpolation of a dataset containing the probe coordinates in time. This approach managed to recreate the expected output with a little distortion that arose from the interpolation error in the order of 10^{-5} in the probe location. These distortions became more evident when plots are zoomed in, as presented in Figure 5.3, which shows the u_x profile until the instant $t = 0.005$.

Figure 5.1 - Fixed solution: Temporal profile for u_x collected by the probe tracked using parametric equations versus reference solution.

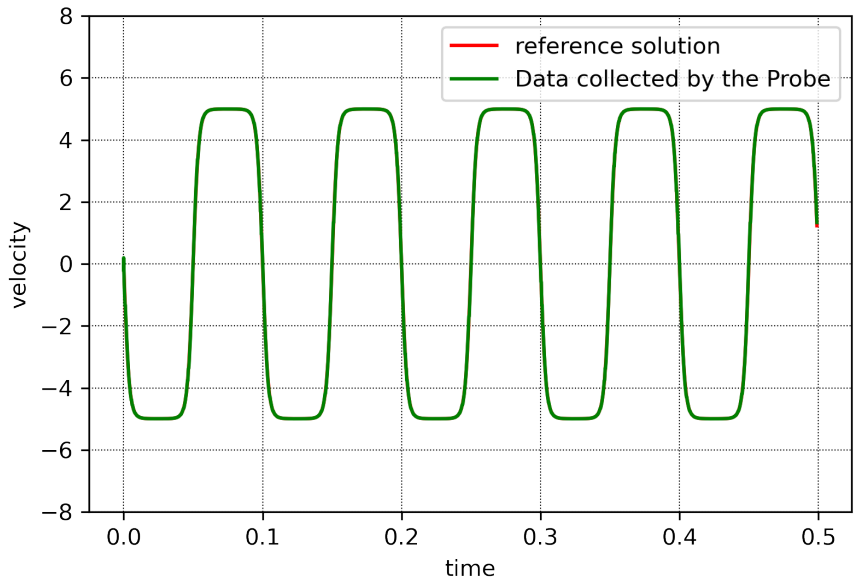

SOURCE: Author's production.

Figure 5.2 - Fixed solution: Temporal profile for u_x collected by the probe tracked using a dataset of cartesian coordinates in time versus reference solution.

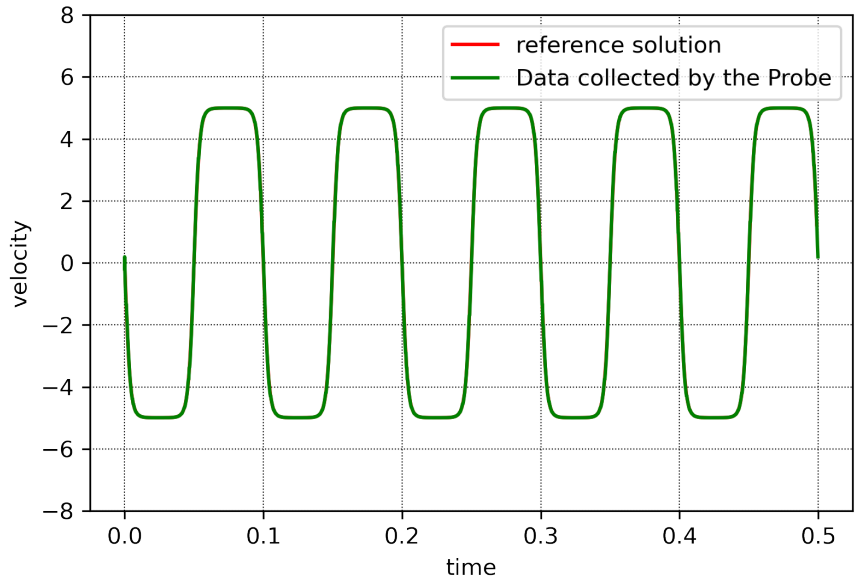

SOURCE: Author's production.

5.1.2 Test 2: sampling from an evolving solution

In the second test, the Kelvin-Helmholtz instability evolved overtime while the probe samples the solution following the orbit:

$$x(t) = 0.5 + 0.4cos\left(\frac{2\pi t}{0.1}\right) \tag{5.4}$$

$$y(t) = 0.5 + 0.4sin\left(\frac{2\pi t}{0.1}\right) \tag{5.5}$$

By performing this orbit, the probe is expected to circle around one of the vortices five times during the simulation, while crossing the cat's eye structures that are being formed after every 0.05 time unit.

Figure 5.4 presents the density profile collected by the probe during the simulation, besides that, Figure 5.5 shows the formation of two cat's eyes KH instability in opposite directions for times from $t = 0.0$ up to $t = 0.5$, this is owing to two velocities shear in opposite direction. These figures also present a circle that contains the trajectory of the Probe around the cat's eye, as defined in the circular orbit given

Figure 5.3 - Fixed solution: Temporal profile, for u_x collected by the probe tracked using dataset of cartesian coordinates in time versus reference solution.

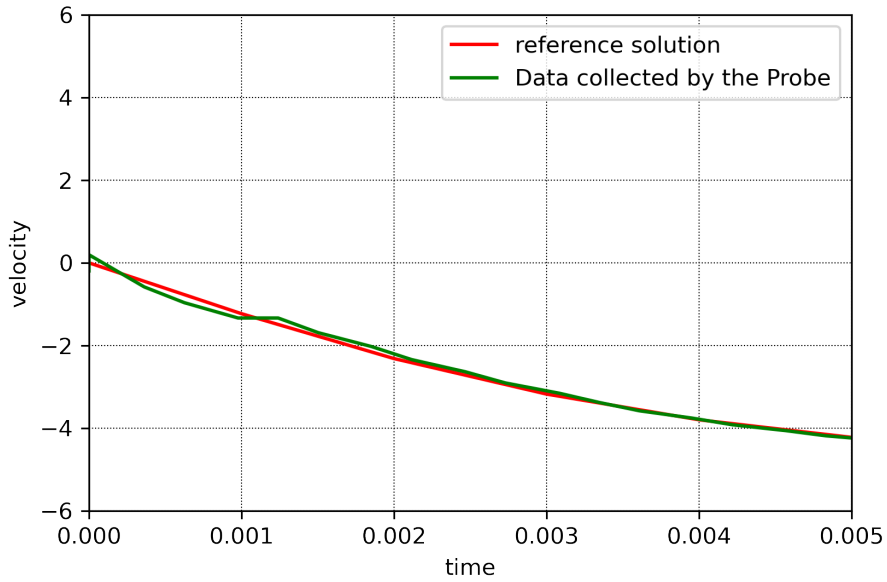

SOURCE: Author's production.

by Equation 5.3.

The parametric equations of the orbit indicate that the probe should cross the cat's eye structures slightly after the instants 0.0, 0.1, 0.2, 0.3, 0.4, and 0.5 on the right side and after the instants 0.05, 0.15, 0.25, 0.35 and 0.45 on the left side. These structures should appear in the density profile as a sudden and momentary drop that occurs in a region of maximum. Indeed, the combination of Figures 5.4 and 5.5 shows that the probe managed to detect the formation of the cat's eye structure with the tiny drop near the maximum around the instant $t = 0.2$. Then, this pattern is repeated with greater intensity after every 0.05 time instants, which is the time the probe takes to traverse from one arm of the cat's eye structure to another.

Figure 5.4 - Evolutive density measure from the cat's eye.

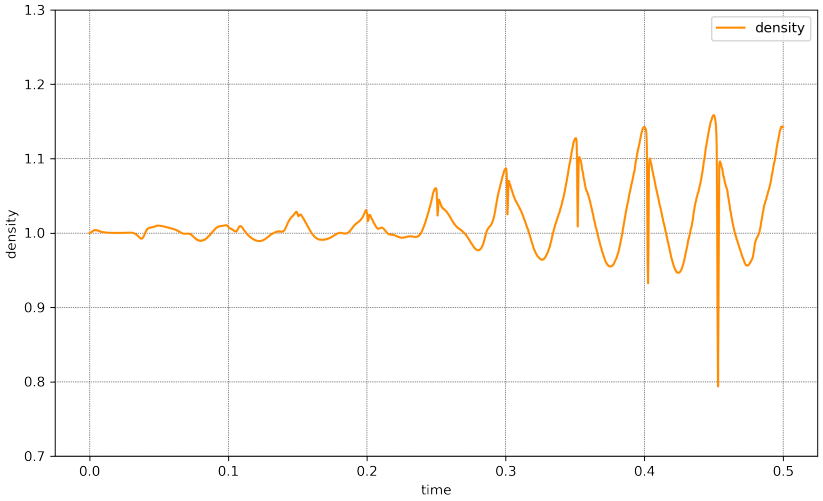

SOURCE: Author's production.

Figure 5.5 - Results for density in multiple time instants.

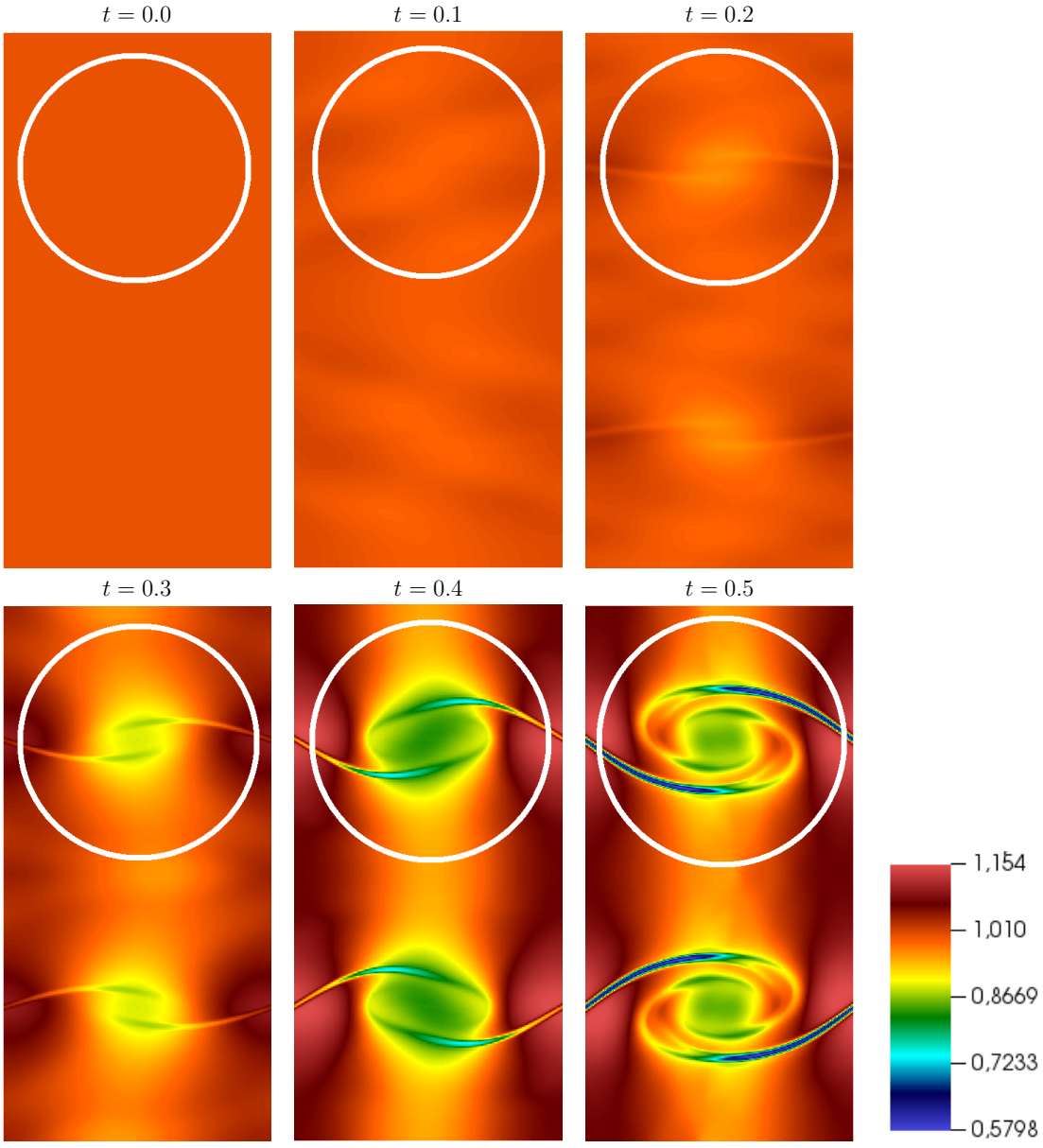

SOURCE: Author's production.

5.1.3 Test 3: sampling-based on physical property

This third test is performed using an experiment described in Tóth et al. (2012) that configures a Shock-Cloud Iteration (SCI). The configuration described the disruption of a high-density magnetic cloud by a strong shock wave. The idea is to verify the proposed methodology to locate the nose of a bow shock structure in three-dimensional simulations, which will be applied in studies of the magnetosphere. The SCI experiment is chosen for this verification test due to also producing a bow shock while being a less complex phenomenon.

The proposed strategy for the probe locating the bow shock structure uses some empirical knowledge from the modelling, such as the direction of the shock wave and a rough approximation of the interval inside the domain that the nose of the structure should oscillate. With that, the algorithm searches for the steepest density gradient in the direction in which the shock wave is moving.

The simulations were performed inside the computational domain $[0, 1]^3$ with outlet boundaries and an initial condition given according to the adiabatic constant $\gamma = 1.6$ as: The initial state of the shock wave, defined by $x < 0.05$, as:

$$q^0(x < 0.05, y, z) = \begin{bmatrix} \rho \\ p \\ u_x \\ u_y \\ u_z \\ B_x \\ B_y \\ B_z \end{bmatrix} = \begin{bmatrix} 3.86859 \\ 167.345 \\ 11.2536 \\ 0 \\ 0 \\ 0 \\ 2.1826182 \\ -2.1826182 \end{bmatrix} \tag{5.6}$$

The stationary state, defined by $x > 0.05$, as:

$$q^0(x > 0.05, y, z) = \begin{bmatrix} \rho \\ p \\ u_x \\ u_y \\ u_z \\ B_x \\ B_y \\ B_z \end{bmatrix} = \begin{bmatrix} \rho^0 \\ 1 \\ 0 \\ 0 \\ 0 \\ 0 \\ 0.56418958 \\ 0.56418958 \end{bmatrix} \tag{5.7}$$

where ρ^0 is defined according if the point (x, y, z) is contained in the high-density cloud with the center in $(0.25, 0.5, 0.5)$ and radius 0.15:

$$\rho^0 = \begin{cases} 10, & \text{if } (x-0.25)^2 + (y-0.5)^2 + (z-0.5)^2 < 0.15^2 \text{ (High density cloud)} \\ 1, & \text{Elsewhere} \end{cases} \tag{5.8}$$

until the final time $t = 0.6$.

For these tests, the following simulation parameters were applied: HLLD Riemann solver Miyoshi and Kusano (2005) combined with an MC limiter. The parabolic-hyperbolic correction uses the factor $\alpha_p = 0.4$. The Courant number (CFL) is set $\sigma = 0.4$.

To verify the data collected in this experiment, Figure 5.6 contains the pressure solution in four instants of the SCI phenomena, while Figure 5.7 contains a temporal profile of the pressure solution at the bow shock.

The behavior of the pressure collected by the Probe agrees with the simulation as observed in Figure 5.7 during time $t = 0.012$ where found the peak, and also for times $t = 0.03$, $t = 0.048$, and $t = 0.06$ where values are decreasing gradually. Finally, the Probe managed to record successfully the pressure during the Shock-Cloud Iteration at each time after its formation around $t = 0.006$.

Another verification test performed with this experiment is the evolution in time of the probe positioning in order to follow the bow shock nose. In general, the movement of the Probe must be variable because of the movement of the blast wave at each time.

The purpose of having a toll that is capable of positioning itself both inside or outside the bow shock is capable of collecting data from both regimes in the magnetospheric simulations.

Figure 5.8 presents probe positioning over time considering three different strategies: over the Bow shock, right or left of it. During the analysis of the phenomena, was observed empirically that the bow shock nose position never exceeded $x = 0.15$, which agrees with the collected positioning from the probe. Also, as expected, is observed that, for the cases collecting data outside or inside the bow shock, there is a displacement in the probe positioning to the right (red) and to the left (green), with the predefined size of 3 grid cells each.

Figure 5.6 - SCI: pressure solution for several time instants.

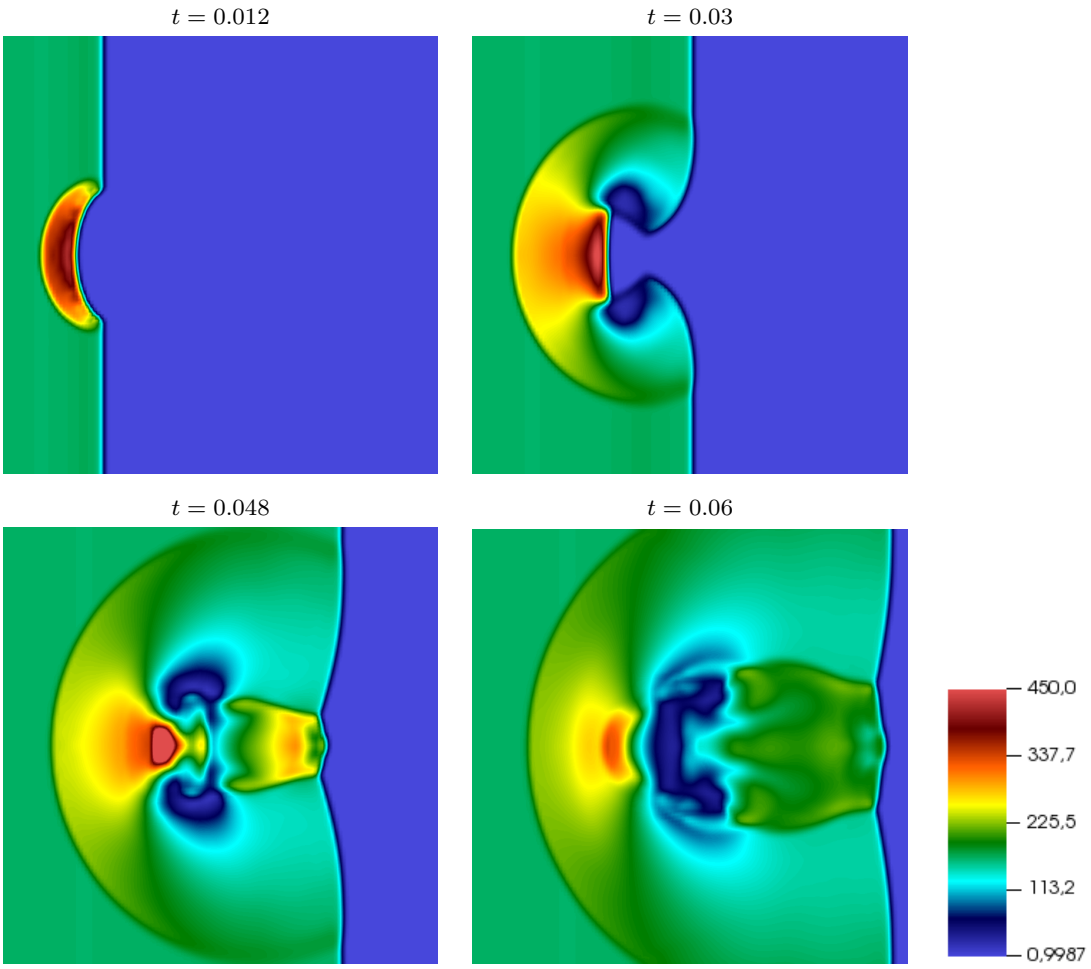

SOURCE: Author's production.

Figure 5.7 - SCI: temporal profile for pressure at the nose of the bow shock.

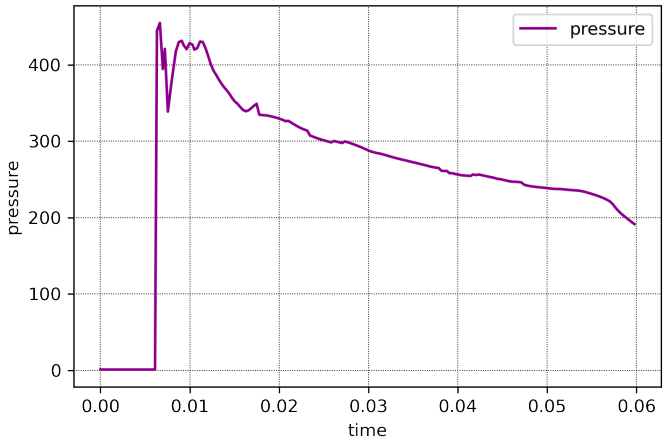

SOURCE: Author's production.

Figure 5.8 - Position collecting by the Probe between $x = 0$ up to $x = 0.15$.

Outside the bow shock

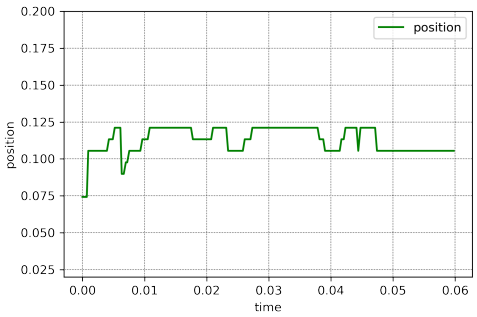

Inside the bow shock

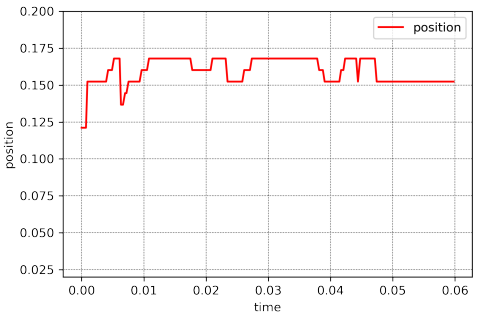

Bow shock nose

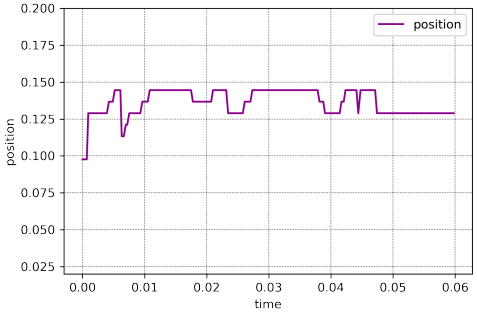

SOURCE: Author's production.

6 SIMULATION MAGNETOSPHERE: RESULTS

Datasets corresponding to High-Intensity Long Duration Continuous AE Activities (HILDCAAs) events were considered for the two dimension magnetosphere implemented before. These case studies are due to the challenging aspect of understanding such kinds of phenomena related to behaviour regimes of geomagnetic disturbances from moderate to weak and also because of their complicated processes.

6.1 Solar wind dataset

The dataset was downloaded from https://omniweb.gsfc.nasa.gov/form/dx1.html where get the magnetic field, density, temperature, and velocity of the solar wind with a high resolution of one minute each one. This dataset has some gaps and missing values that need to be corrected. For that, was used a Hermite interpolation to fill the gaps and a discrete wavelet with six frequency-band components to smooth the data. Finally, this updated, clean dataset was introduced as a boundary condition in AMROC to initiate the simulation.

To test the magnetosphere following the conceptual proposition of Ogino (1986) was considered a geomagnetic disturbance designated by HILDCAAs. Thus, four datasets were considered: HILDCAA occurring preceded by Interplanetary Coronal Mass Ejection (ICME), by Corotating Interaction Region (CIR), and a standard one practically understood as Non-storm. The Quiet period event was taken into account as a control case, which characterizes the background disturbance behaviour composing the second condition of the magnetohydrodynamics scenario.

For an event to be considered a HILDCAA, it must satisfy the following criteria (TSURUTANI; GONZALEZ, 1987):

- AE is expected to reach over 1000 nT at least once during the event.
- It should last at least two days.
- It should not occur AE values below 200 nT for periods longer than two hours at a time.
- It must occur outside the main phase of geomagnetic storms (see detail in Appendix E.1).

6.2 HILDCAA ICME

Usually, during the solar maximum phase, the main structures emanating from the sun are interplanetary remnants of coronal mass ejections (CME) (BURLAGA et al., 1981). Nevertheless, these phenomena may also occur during the other part of the solar cycle. When these structures reach the front of the magnetosphere, the first effect is dynamic, caused by the compression of the magnetosphere due to the relatively high density of the structure. This compression upon the magnetosphere leads to an intensification of the Chapman-Ferraro current, appearing as a positive Sudden Impulse in the Dst index (NISHIDA, 1978). Such impulses are called Storm Sudden Commencements (SSC) when preceding geomagnetic storms, which are caused by a frontal magnetic reconnection. Under this circumstance, there is an increase of solar wind particles penetrating the magnetosphere and enriching the ring current. The enhanced Dst period that follows the SSC is the storm's initial phase, which can last for a few hours (although this initial phase is not an obligatory feature of a storm).

The interval during which the Dst index decreases is the storm Main Phase, which can last for tens of hours. This phase is caused by a sustained southward interplanetary field reaching the magnetosphere. If the high amplitude B_z is maintained for a sufficiently long time, it produces large particle injections in the ring current and causes the decrease of the Dst (GONZALEZ et al., 1994). Figure 6.1 shows variables of the solar wind dataset where the grey color indicates the original dataset and the black color indicates the clean dataset after filling the missing and smoothing values in DOY time.

The third panel of Figure 6.1 shows a great velocity which reaches almost $1000\frac{km}{s}$, but this velocity decreased gradually in the next two days. Another parameter to analyze is the AE index because and agree with Tsurutani and Gonzalez (1987) the AE reaches 1000 nT more than once during the whole event, and also the AE is always greater than 200 nT for more than two consecutive hours. The other two criteria mentioned by Tsurutani and Gonzalez (1987) are found in Figure 6.2 where is shown the Dst during the whole event and also left, between, and right to the green line corresponds to the Initial, Main, and Recovery phase. Thus, the Dst decreases hundreds of nT, corresponding to an *intense regime* following the criteria written in *Appendix E*.

Finally, the HILDCAA event lasts more than two days and happens outside the main phase of the geomagnetic storm. It is convenient to clarify that letters A and B in the last panel of Figure 6.1 show instants of time chosen to illustrate effects present in the magnetosphere. While A refers to an interval preceding the HILDCAA, B concerns precisely a condition during this kind of phenomenon. Similar designations in other figures as follow in the text are intended to be interpreted with the same meaning.

Figure 6.1 - HILDCAA-ICME dataset from 14 to 19 May 2005.

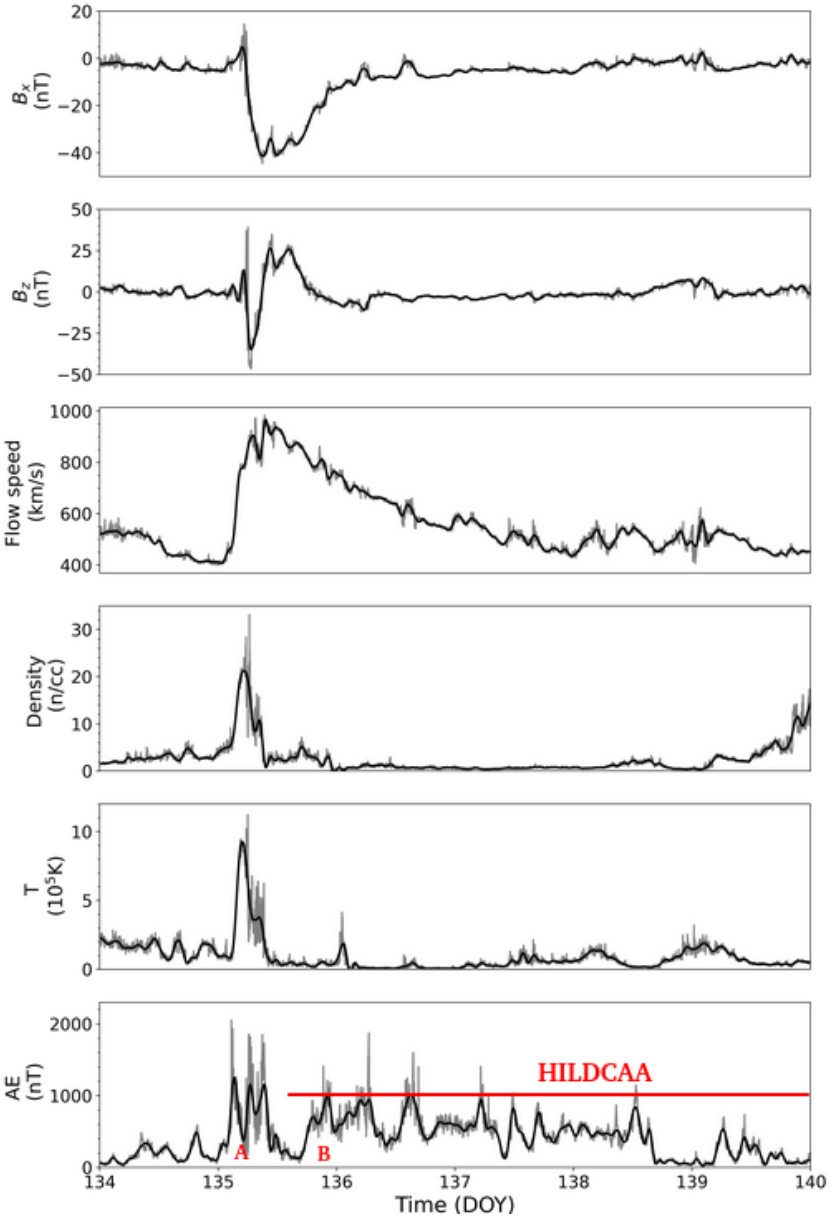

SOURCE: Author's production.

Figure 6.2 - Solar Maximum (ICME) Storm.

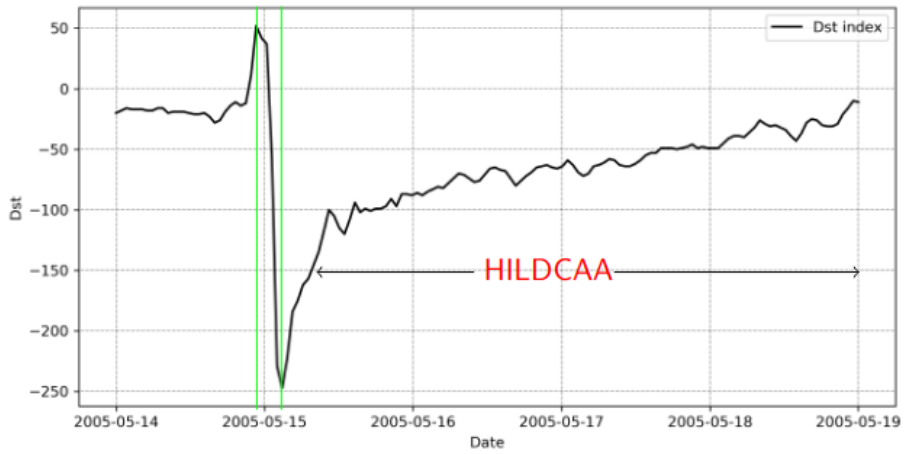

SOURCE: Author's production.

6.3 HILDCAA CIR

Usually, during the descending and minimum phases of solar cycles, the CME becomes less frequent, and another kind of solar structure occurs more often: coronal holes. Coronal holes, which appear as a dark region in x-ray images of the Sun, are confined to solar poles during the solar maximum phase, but in the descending phase, they expand in size and move toward the solar equator (HUNDHAUSEN., 1973).

These coronal holes are open magnetic field regions from where emanate high-speed solar wind streams (SHEELEY N. R. et al., 1976; SHEELEY; HARVEY, 1981). High-speed streams have velocities much higher than the typical velocities observed in the solar wind, forming an interface region between the slow and fast streams. At large heliocentric distances (typically larger than 1 AU), these stream interfaces/interaction regions are bounded by a pair of shocks (SMITH; WOLFE, 1976).

Since coronal holes are long-lived structures, they can persist for more than one solar rotation. The high-speed streams originating from the same region reappear at intervals of approximately 27 days (SMITH; WOLFE, 1976). This reappearance leads to the term "recurrent streams". The spiral-like structure formed by these streams, distorted due to the solar rotation and its interaction regions with slower streams, is known as CIR.

Another critical aspect of these fast streams is that they are embedded with Alfvén waves (BELCHER; JR., 1971). These kinds of waves are believed to be remnants of heating processes in the inner Sun (HOLLWEG, 1978). In the interplanetary data, these waves appear as large amplitude oscillations in magnetic field components, well correlated with the oscillations of the velocity components (in the same direction).

Generally, storms caused by CIR have initial, main, and recovery phases. The initial phase, characterized by an increase in the Dst index, is caused by the compressed region in front of the high-speed stream. This is a gradual initial phase, not a sudden commencement (TSURUTANI et al., 1995). The main phase of a CIR storm is caused by the southward component of Alfvén waves in the IMF. In this way, a short southward oriented (B_s) interval leads to an increase of the geomagnetic activity (decrease in Dst index). The recovery time until the next B_s interval is too short to allow a ring current recovery, and then the effect of the next B_s interval is superposed to the first one. When the oscillations diminish or the mean value of the B_z component becomes more positive, the storm starts its long recovery phase. Due to oscillations in the field, even after the main phase, the recovery phase may be significantly longer than the recovery phase of an ICME storm (Gonzalez et al., 1999).

Figure 6.3 shows variables of the solar wind dataset where the grey color indicates the original dataset and the black color indicates the clean dataset after filling the missing and smoothing values in DOY time. The third panel of Figure 6.3 shows velocity, which reaches almost $800\frac{km}{s}$ for 4 days in a row, which is very interesting because it explains why the recovery phase is the largest one. Moreover, the AE reaches $1000nT$ more than once and the AE is always greater than $200nT$ for 2 consecutive hours.The other two criteria mentioned by Tsurutani and Gonzalez (1987) are found in Figure 6.4 where is shown the Dst index during the whole event and also left, between and right to the green line corresponds to the Initial, Main, and Recovery phase. Thus the Dst decrease nearly to $-90nT$ which corresponds to a *moderate regime* following the criteria written in *Appendix E*. Moreover, the HILDCAA event lasts more than two days and happens outside the main phase of the geomagnetic storm.

Although the CIR storm has a weak or moderate regime, its duration can be much longer than those observed during ICME storms. Consequently, these events can also transfer large amounts of energy from the solar wind to the magnetosphere due to their long-duration main character.

Figure 6.3 - HILDCAA-CIR dataset from 10 to 18 February 2004.

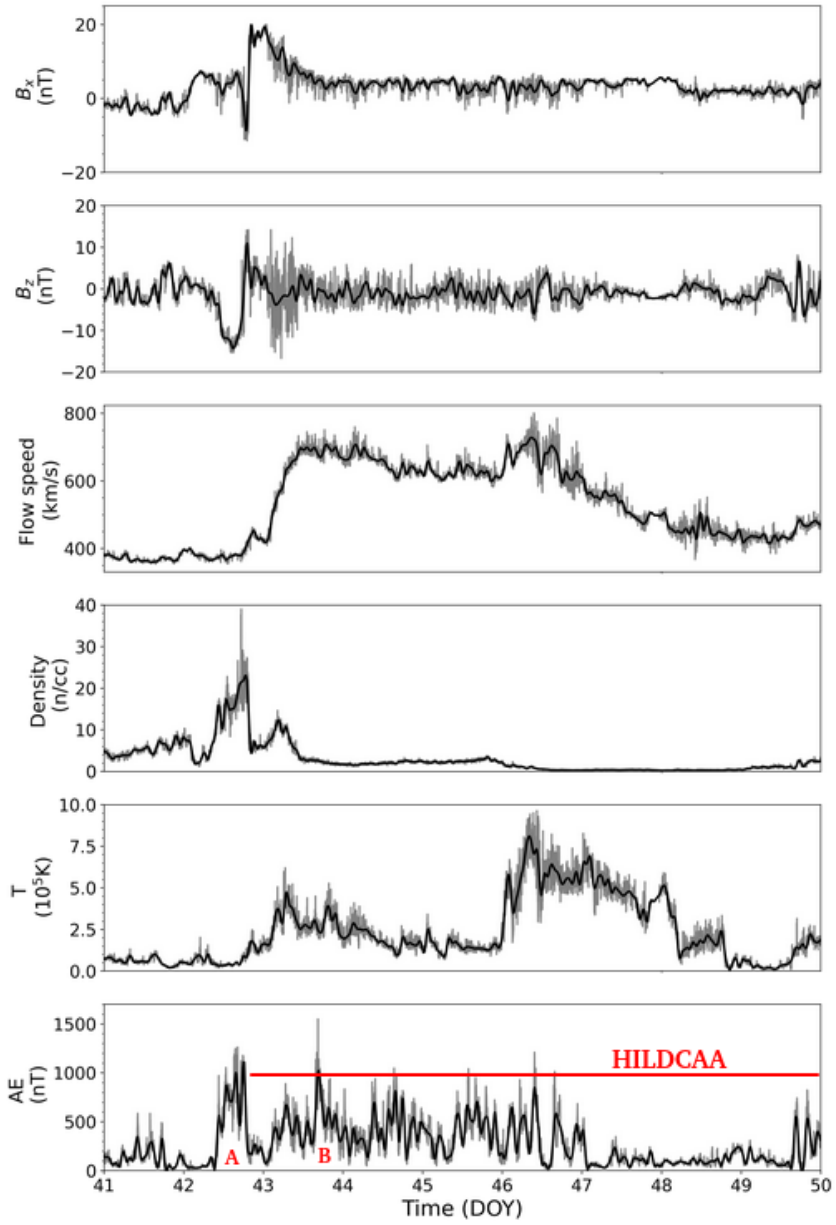

SOURCE: Author's production.

Figure 6.4 - Solar Minimum (CIR) Storm.

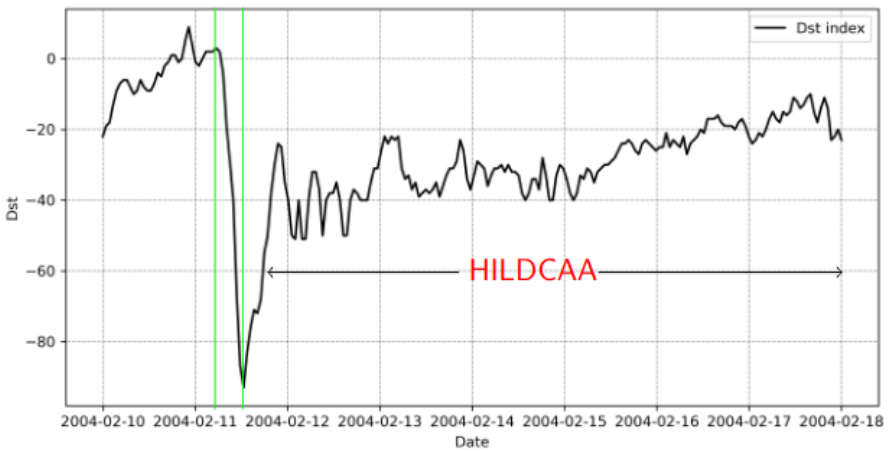

SOURCE: Author's production.

6.4 HILDCAA NonStorm

Hajra et al. (2013) studied one hundred thirty-three AE events satisfying the HILDCAA criteria suggested by Tsurutani and Gonzalez (1987) and found 94% were associated with CIR. The remaining 6% occurred after the passage of ICME.

Figure 6.5 shows variables of the solar wind dataset where the grey color indicates the original dataset and the black color indicates the clean dataset after filling the missing and smoothing values in DOY time.

The third panel of Figure 6.5 shows velocity which reaches $700\frac{km}{s}$ for more than two days in a row. Due to the event meets approximately the criteria proposed by Tsurutani and Gonzalez (1987), reaches roughly $1000nT$ during the whole event, and AE is greater than $200nT$ for more than two hours in a row. As this event is related to a non-storm period, no phase is identified in Dst. According to the criteria, the AE index characterizes the interval of the HILDCAA.

Nevertheless, it is feasible to identify a low latitude geomagnetic period where Dst decreases below the zero reference level ($Dst_{min} > -40$ nT), as shown in Figure 6.6. This behaviour allows noticing a kind of effect on low latitudes associated with the HILDCAA, in agreement with the study developed by Mendes and team (MENDES et al., 2022).

Figure 6.5 - HILDCAA-NonStorm dataset from 28 June to 03 July 2012.

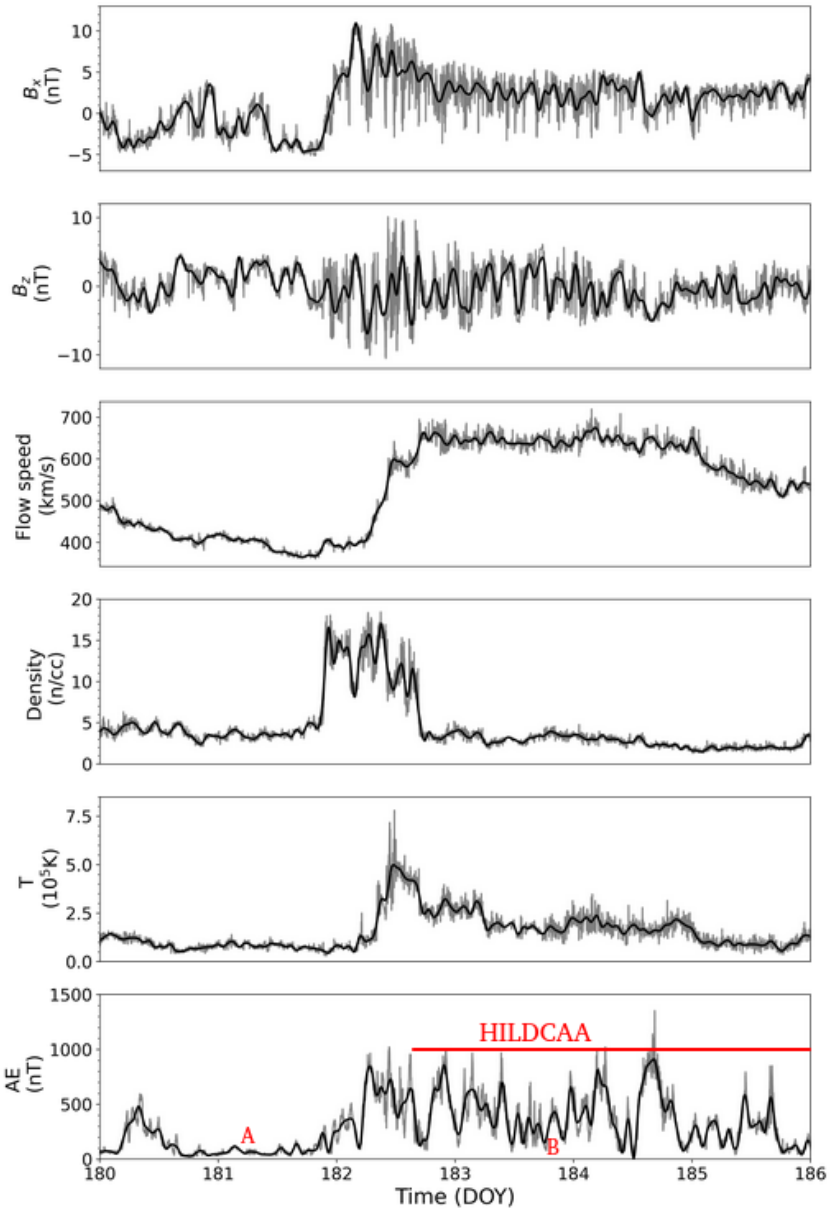

SOURCE: Author's production.

Figure 6.6 - Non-Storm event.

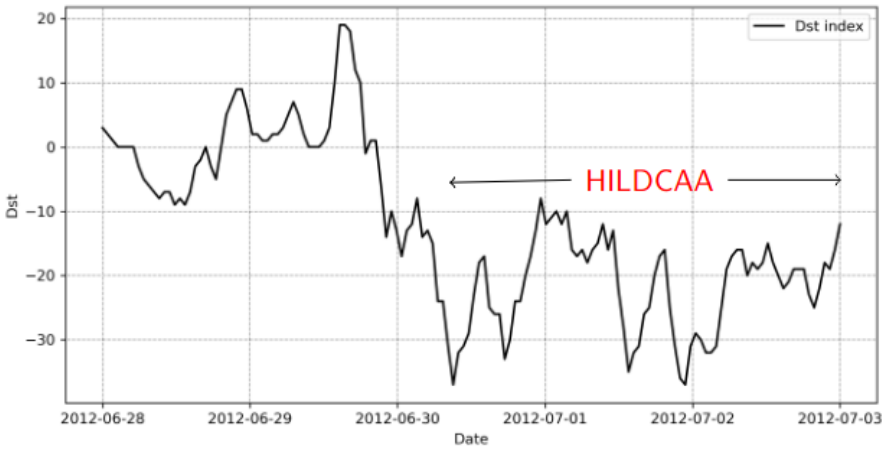

SOURCE: Author's production.

6.5 Quiet period

For quiet periods there were many datasets, but an appropriate one was chosen following the next assumptions: the Dst should be greater than $-30nT$, and the AE should be smaller than $300nT$. Thus, the dataset from 17 to 22 July 2006 was chosen. Also, this event is helpful as control concerning the other HILDCAA events.

Figure 6.7 shows variables of the solar wind dataset where the grey color indicates the original dataset and the black color indicates the clean dataset after filling the missing and smoothing values in DOY time.

The third panel of Figure 6.7 shows the velocity reaches values less than $400\frac{km}{s}$, and the AE has values less than $300nT$, which corresponds to the quiet period.

In this study case, Letters A and B refer to two arbitrary instants occurring in a quiescent interplanetary condition related to a geomagnetically quiet state on the Earth's surface. This case allows contraposition with the earlier events, which refer to HILDCAA, while here, a kind of space environment background regime is explored.

Figure 6.7 - Quiet period dataset from 17 to 22 July of 2006.

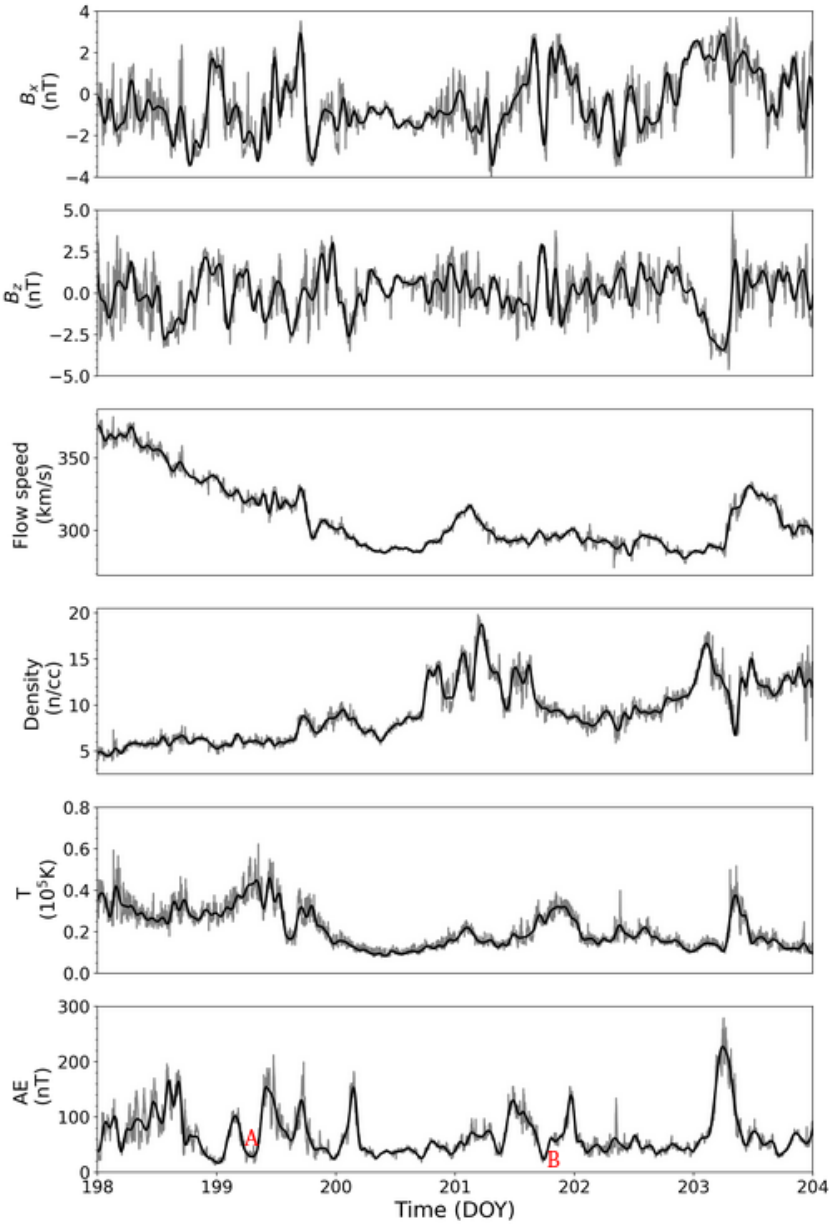

SOURCE: Author's production.

6.6 2D simulations for HILDCAAs and Quiet events

This section will display some simulations considering these four cases: HILDCAA preceded by ICME, CIR, and Non-Storm, and, complementary, a Quiet period.

Figure 6.8 shows the representation of density and magnetic field lines, which was simulated for four days, the first two of them refer still to the stabilization of the hydrodynamic and magnetic components of the magnetosphere, and the last two days refer to the solar wind dataset. Thus, each panel was labeled by letters A and B, concerning the frames collected on the days where the plots were taken as observed in Figure 6.1 and the left panel of Figure 6.12. Also, the solar wind is acting from the left during the whole simulation. The difference between the left (taken at 135 04 05 DOY time) and right (taken at 135 21 07 DOY time) panels of Figure 6.8 is approximately 17 hours. In the first frame, the magnetopause compression is noticeable, and it precedes the magnetic reconnection to be developed, as seen by the B_Z component southward incursion in Figure 6.1. It is essential to clarify that, outside the AMROC domain, the magnetic field lines in the figures are indeed constructed by visualization software (Paraview was chosen for that), which numerically integrates an ODE using the **B** vector. The user's skill can overcome arising numerical errors for this integration (such momentaneous inability can cause undesired artifacts in the lines).

Figure 6.8 - HILDCAA-ICME.

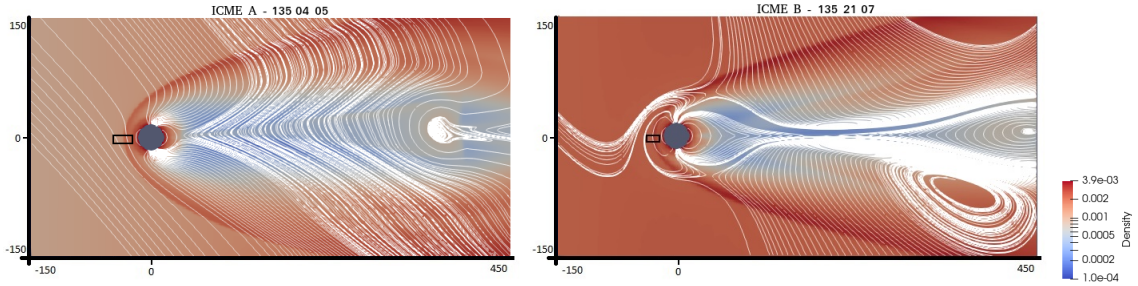

Note: Representation of the density and the magnetic field lines that were constructed by visualization software, which numerically integrates an ODE using the **B** vector.

SOURCE: Author's production.

Figure 6.9 - HILDCAA-CIR.

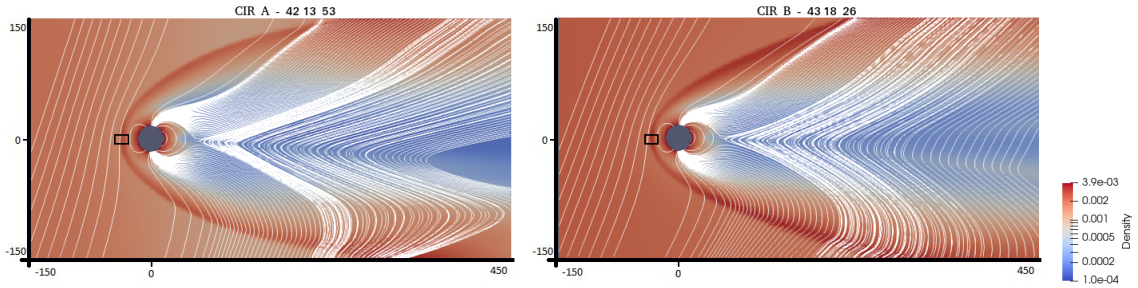

Note: Representation of the density and the magnetic field lines that were constructed by visualization software, which numerically integrates an ODE using the **B** vector.

SOURCE: Author's production.

Moreover, the frames (not shown here) show a magnetic reconnection event where the dynamic solar wind pressure produces a compression of the magnetosphere, as a consequence, the Chapman-Ferraro current will increase in magnitude making an increase in the horizontal component of the Earth's magnetic field, this process is called sudden impulse and also producing that Dst becomes positive, but after some hours this index is going to intensify dramatically (intense regime) as seen in Figure 6.2, that occurs because the reconnection is injecting a lot of particles to the ring current producing a high decrease in the Earth's magnetic field at low latitudes

Figure 6.10 - HILDCAA-NonStorm.

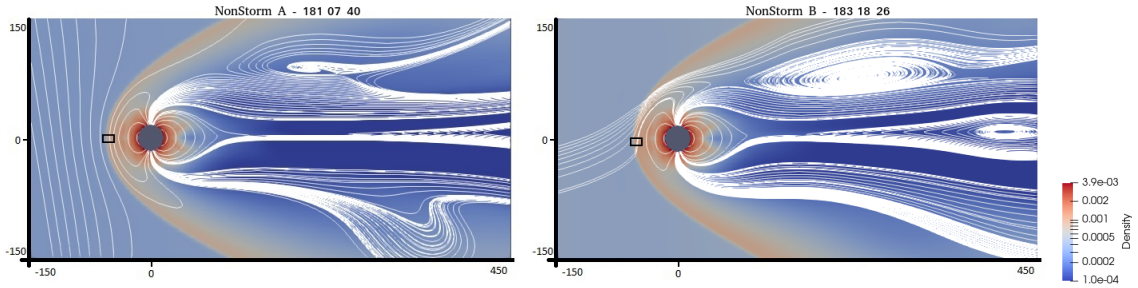

Note: Representation of the density and the magnetic field lines that were constructed by visualization software, which numerically integrates an ODE using the **B** vector.

SOURCE: Author's production.

Figure 6.11 - Quiet period.

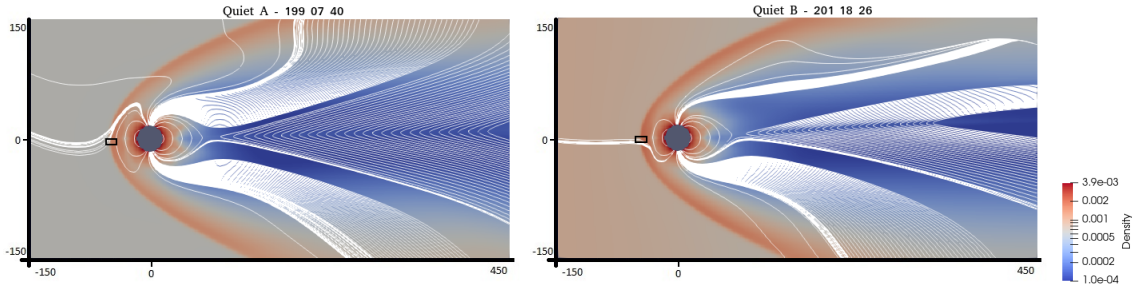

Note: Representation of the density and the magnetic field lines that were constructed by visualization software, which numerically integrates an ODE using the **B** vector.

SOURCE: Author's production.

on the surface.

Besides that, the left panel of Figure 6.8 shows a bubble of plasma disrupting and going towards the interplanetary medium; differently, the right panel of Figure 6.8 forms another configuration structure. Also, the right panel of the Figure 6.8 shows reconnection regions at flanks (top and bottom) concerning high latitude positions. The AMROC framework is able to simulate such a complex structure, the HILDCAA event, for a two-dimensional magnetosphere in an approach following the proposed by (OGINO, 1986).

Figure 6.9 shows the representation of density and magnetic field lines, which was simulated for six days, the first two of them refer to the stabilization of the hydrodynamic and magnetic components of the magnetosphere, and the last four days refer to the solar wind dataset. Thus, each panel was labeled by letters A and B, concerning the frames collected on the days where the plots were taken as observed in Figure 6.3 and the right panel of Figure 6.12. Also, the solar wind is acting from the left during the whole simulation.

The difference between the left (taken at 42 13 53 DOY time) and right (taken at 43 18 26 DOY time) panels of Figure 6.9 is approximately one day where is visible the bow shock and the compression of the magnetopause.

Thus, the left panel of Figure 6.9 shows a magnetic reconnection event where there is an increase in the horizontal component of the Earth's magnetic field, but the dynamic solar wind pressure does not produce this, instead is caused by the shock due to the very high velocity (about 700 km/s) which is spelled from the coronal holes of the Sun. Moreover, this high velocity which is called high-speed stream (HSS) carries some perturbations, Alfvén waves, so the southward component of these waves will produce a reconnection on the magnetopause producing an intensification of Dst (moderate regime) as seen in Figure 6.4, where particles are ejecting toward the ring current of the Earth.

Moreover, the left and right panels of Figure 6.9 allow interpreting the injection of particles toward the Earth through the reconnection mechanism in the tail.

Figure 6.10 shows the representation of density and magnetic field lines, which was simulated for six days, the first two of them refer to the stabilization of the hydrodynamic and magnetic components of the magnetosphere, and the last four days refer to the solar wind dataset. Thus, each panel was labeled by letters A and B, concerning the frames collected on the days where the plots were taken as observed in Figure 6.5 and the right panel of Figure 6.13. Also, the solar wind is acting from the left during the whole simulation.

The difference between the left (taken at 181 07 40 DOY time) and right (taken at 183 18 26 DOY time) panels of Figure 6.10 is approximately two days.

The interval concerning Figure 6.10 shows a slight intensification of the Dst (weak regime) as seen in Figure 6.6; however, practically, it follows the criteria written in *Appendix E*, because the effect does not correspond to a significant geomagnetic

disturbance. Consequently, one can interpret this occurrence as connected to a non-significant frontal reconnection in this event. In a certain way, the occurrence can be interpreted with the aid of the right panel of Figure 6.10.

From the earlier studied events, we verified that the AMROC framework can simulate the complex structures of the HILDCAA event for a two-dimensional magnetosphere, reaching and allowing improving the solar-terrestrial MHD investigations, as an example of motivation, the work proposed by (OGINO, 1986) can be cited. Thus, with this work, some highlights of the structures existing during periods of HILDCAA (mainly describing how they are affected or not by preceding other interplanetary phenomena) have been reached.

To complete the study, Figure 6.11 shows the representation of density and magnetic field lines that was simulated for six days. The first two of them refer to the stabilization of the hydrodynamic and magnetic components of the magnetosphere, and the last four days refer to the solar wind dataset. Thus, each panel was labeled by letters A and B, concerning the frames collected on the days where the plots were taken as observed in Figure 6.7 and the left panel of Figure 6.13. Also, the solar wind is acting from the left during the simulation.

The difference between the left (taken at 199 07 40 DOY time) and right (taken at 201 18 26 DOY time) panels of Figure 6.11 is approximately two days.

Figure 6.11 shows typical magnetosphere behaviours (at the bowshock, magnetopause, and the plasma sheet) occurring under quiescent interplanetary conditions. This simulation result, together with the others, allows in future someone to compare and consider geomagnetically quiet conditions as background to characterize magnetohydrodynamics characterization regimes.

6.7 Probe position on the Bow shock

During the simulation, the 2-dimensional Probe was activated. It was located in the nose of the bow shock using the **Trajectory** function and positioned in the center of it, as was explained in Section 5.1.

Figure 6.12 shows to the left ICME and to the right CIR events where the grey color indicates the original dataset collected by the Probe and the black color indicates the same dataset after smoothing it.

In a similar way, Figure 6.13 shows to the left Quiet and to the right Non-storm events where the grey color indicates the original dataset created by the Probe and the black color indicates the same dataset after smoothing it.

The probe was built to get conservative variables from the desired area, but the *Probe2D.h* file was modified to get primitive variables which are: magnetic field, density, velocity, and pressure. Also, the *Probe2D.h* file was adapted to get the position of the probe during the simulation that was depicted in the last panel of Figure 6.12 and Figure 6.13. Besides that, the probe is working in an area measured in Earth radii for each case, such that: from -70 to -30 for CIR and Non-storm cases, from -90 to -25 for ICME case, and from -70 to -40 for the Quiet case. These areas are depicted in *black* rectangle in Figure 6.8, Figure 6.9, Figure 6.10 and Figure 6.11.

The letters A and B in red shown in the last panel of Figure 6.12 indicate the moment where Figure 6.8 and Figure 6.9 were taken. Thus, these representations were considered the last two days for the ICME and the last three days for the CIR. To see the complete times series, see *Appendix D*.

The letters A and B in red shown in the last panel of Figure 6.13 indicate the moment where Figure 6.10 and Figure 6.11 were taken. Thus, these representations were considered the last three days for each one. To see the complete times series, see *Appendix D*.

The density shown in the fourth panel of Figure 6.12 agrees with the simulation depicted in Figure 6.8 and Figure 6.9. In the same way, the density shown in the fourth panel of Figure 6.13 agrees with the simulation depicted in Figure 6.11 and Figure 6.10.

Finally, the Probe in two dimensions was able to identify the position and the physics

process records in the bowshock providing a valuable tool for records collecting in magnetosphere magnetohydrodynamics simulations using the AMROC framework.

Figure 6.12 - Probe 2D time series.

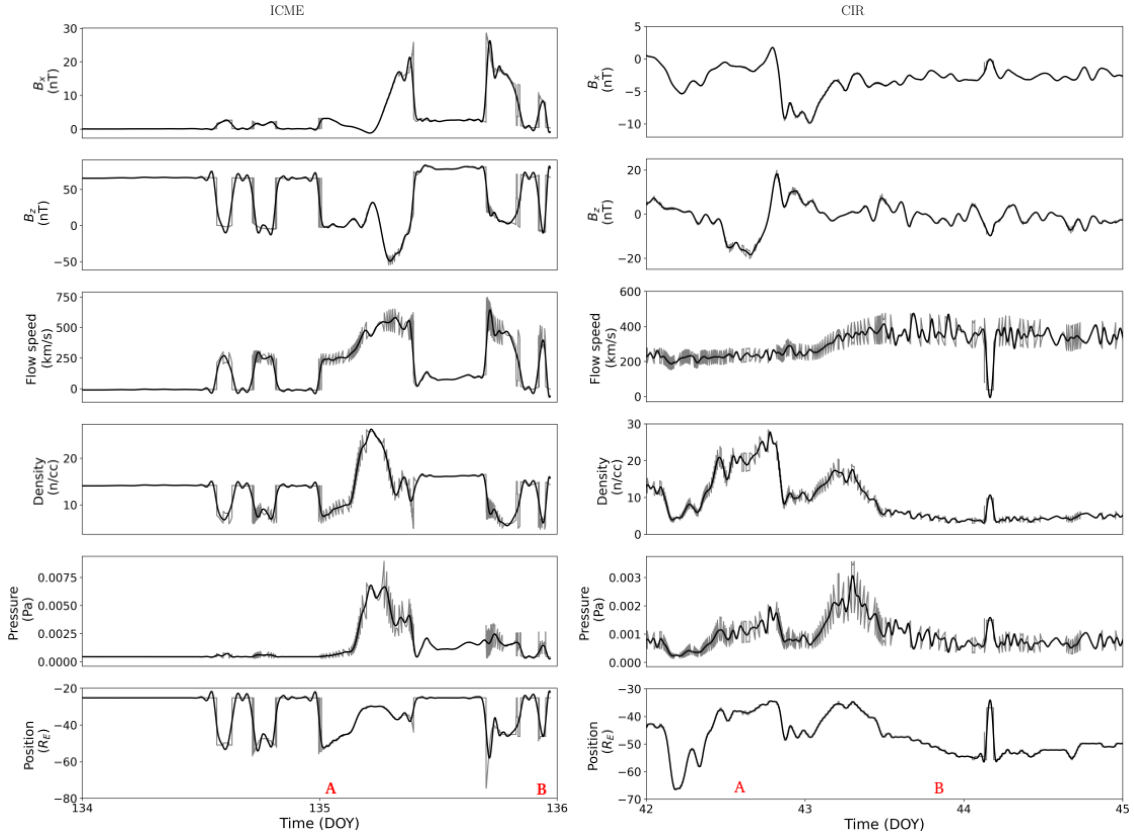

SOURCE: Author's production.

Figure 6.13 - Probe 2D time series.

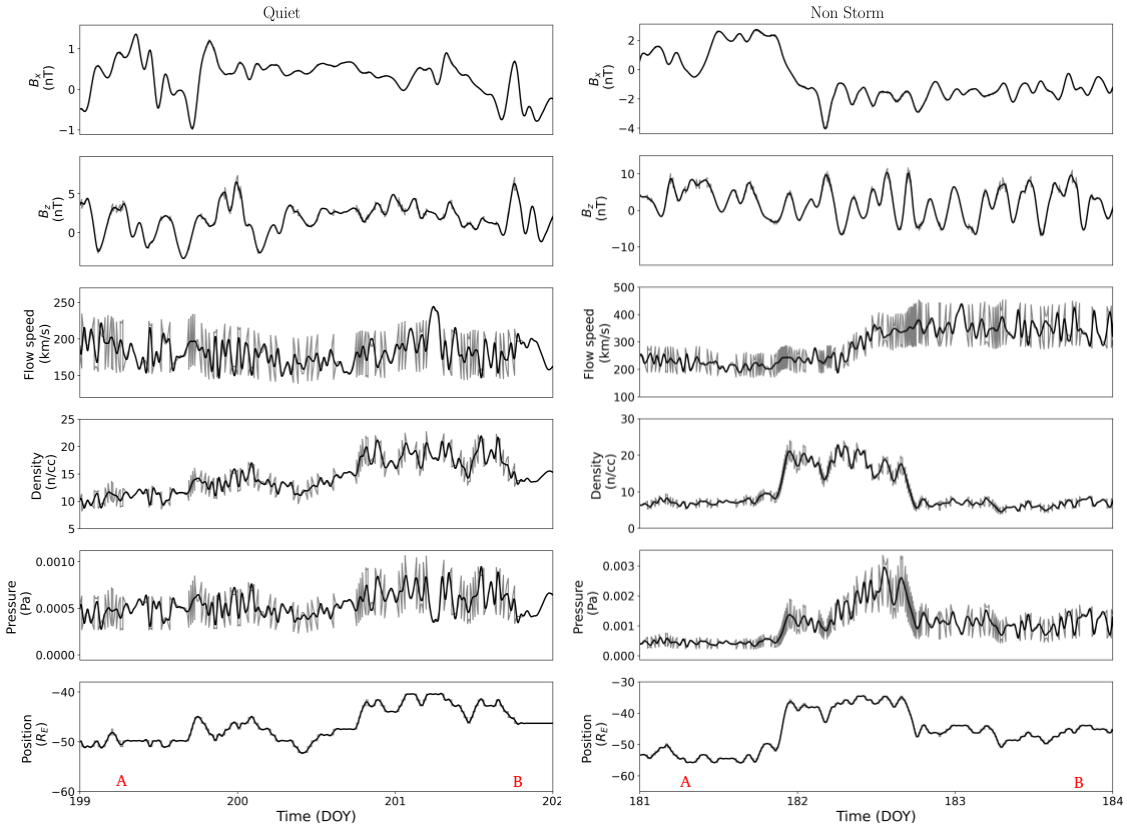

SOURCE: Author's production.

7 CONCLUSIONS

Motivated by the increasing needs of space environment science, scientific computation deals with mathematical-numerical methodologies to implement innovative computational codes. The National Institute for Space Research, INPE, has taken part in this kind of contribution to develop an efficient magnetohydrodynamic (MHD) simulation code aiming at future space plasma investigations and space weather forecasting.

This work developed probes to be executed in the AMROC-MHD code to get conservative variables. The resource was prepared to deal with the 2D and 3D representations.

The Probes were combined with MPI to accelerate the creation of the dataset that it generates and also to force only one process to track the Probe to avoid redundancy in the dataset.

Additionally, some cases of a fascinating electrodynamical phenomenon involving the magnetosphere environment were considered. Although under the same general processes (HILDCAAs), the results obtained have unravelled a very complex development. Their representations deserve future investigations taking into account parametrizations for comprehensive descriptions.

The original contribution of this work is:

- Build a Probe resource in two dimensions and use Kelvin-Helmholtz Instability (KHI) to test it.
- Build a Probe resource in three dimensions and use the Shock-Cloud Iteration (SCI) to test it.
- Create an algorithm to clean and smooth the solar wind dataset using Hermite interpolation and a discrete wavelet with six frequency-band component levels.
- Apply the tools to investigate the general aspects of HILDCAAs produced by ICME, CIR, and Non-Storm and compare them to a background quiescent interplanetary condition.

The perspective of work to be developed as a consequence of this Dissertation:

- Use the three-dimensional magnetosphere model for similar analysis in a more complete physical model.
- Addition of the Ionosphere-Magnetosphere coupling model proposed by (GOODMAN, 1995) as internal boundary conditions for the three-dimensional Magnetosphere model proposed by (TANAKA, 1995) and testing it using HILDCAAs produced by CIR. Initial advances for this end have been done and are described in B.1 and C.1.
- Applications of Probes capable of tracking more physical processes in the magnetosphere.
- Adjustments of the MHD code for other planetary magnetosphere scenarios.
- Investigations of plasma instabilities that arise in the MHD modelling near the Earth because of the Alfvén waves.

REFERENCES

AHRENS, J.; GEVECI, B.; LAW, C. Paraview: an end-user tool for large data visualization. **Visualization Handbook**, 01 2005. 32

AKASOFU, S.-T. The growth of the storm-time radiation belt and the magnetospheric substorm. **Geophysical Journal of the Royal Astronomical Society**, v. 15, n. 1-2, p. 7–21, 1968. 20

AMM, O.; GOODMAN, M. L. Comment on: a three-dimensional, iterative mapping procedure for the implementation of an ionosphere-magnetosphere anisotropic ohm's law boundary condition in global magnetohydrodynamic simulations. author's reply. **Annales Geophysicae**, v. 14, p. 773–775, 1996. 95, 97

ARRARáS, A.; GASPAR, F.; PORTERO, L.; RODRIGO, C. Domain decomposition multigrid methods for nonlinear reaction–diffusion problems. **Communications in Nonlinear Science and Numerical Simulation**, v. 20, p. 699–710, 2015. 97

BAUMJOHANN, W.; TREUMANN, R. **Basic space plasma physics**. [S.l.: s.n.], 1996. 2, 8, 9, 10, 11, 17, 18, 19, 24, 25, 26, 27, 29, 30, 98

BELCHER, J. W.; JR., L. D. Large-amplitude alfvén waves in the interplanetary medium, 2. **Journal of Geophysical Research**, v. 76, n. 16, p. 3534–3563, 1971. 60

BERGER, M. J.; COLELLA, P. Local adaptive mesh refinement for shock hydrodynamics. **Journal of Computational Physics**, v. 82, p. 64–84, 1989. 31

BISKAMP, D. Magnetic reconnection. **Physics Reports**, v. 237, 1994. 15

BRACKBILL, J. U.; BARNES, D. C. The effect of nonzero $\nabla \cdot B$ on the numerical solution of the magnetohydrodynamic equations. **Journal of Computational Physics**, v. 35, n. 3, p. 426–430, 1980. 33

BRIGGS, W.; HENSON, V.; MCCORMICK, S. **A multigrid tutorial**. 2. ed. [S.l.: s.n.], 2000. 97

BURLAGA, L.; SITTLER, E.; MARIANI, F.; SCHWENN, R. Magnetic loop behind an interplanetary shock: Voyager, helios, and imp 8 observations. **Journal of Geophysical Research: Space Physics**, v. 86, n. A8, p. 6673–6684, 1981. 56

CHILDS, H.; BRUGGER, E.; WHITLOCK, B.; MEREDITH, J.; AHERN, S.; PUGMIRE, D.; BIAGAS, K.; MILLER, M.; HARRISON, C.; WEBER, G.; KRISHNAN, H.; FOGAL, T.; SANDERSON, A.; GARTH, C.; BETHEL, E. W.; CAMP, D.; RUBEL, O.; DURANT, M.; FAVRE, J.; NAVRATIL, P. Visit: an end-user tool for visualizing and analyzing very large data. In: **High Performance Visualization-Enabling Extreme-Scale Scientific Insight**. [S.l.: s.n.], 2012. p. 357–372. 32

DEDNER, A.; KEMM, F.; KRONER, D.; MUNZ, C.; SCHNITZER, T.; WESENBERG, M. Hyperbolic divergence cleaning for the mhd equations. **Journal of Computational Physics**, v. 175, n. 2, p. 645–673, 2002. 33, 44, 45

DEITERDING, R.; DOMINGUES, M. O. Evaluation of multiresolution mesh adaptation criteria in the amroc framework. In: IVANYI, P.; TOPPING, B. H. V.; VARADY, G. (Ed.). **Proceedings of the Fifth International Conference on Parallel, Distributed, Grid and Cloud Computing for Engineering**. [S.l.]: Civil-Comp, 2017. 3

DEITERDING, R.; DOMINGUES, M. O.; GOMES, S. M.; SCHNEIDER, K. Comparison of adaptive multiresolution and adaptive mesh refinement applied to simulations of the compressible euler equations. **SIAM Journal on Scientific Computing**, v. 38, n. 5, p. S173–S193, 2016. 3, 31, 32

DERIGS, D.; WINTERS, A. R. Ideal GLM-MHD: about the entropy consistent nine-wave magnetic field divergence diminishing ideal magnetohydrodynamics equations. **Journal of Computational Physics**, v. 364, p. 420–467, 2018. 33

DOMINGUES, M. O.; DEITERDING, R.; LOPES, M. M.; GOMES, A. K. F.; MENDES, O.; SCHNEIDER, K. Wavelet-based parallel dynamic mesh adaptation for magnetohydrodynamics in the amroc framework. **Computers & Fluids**, v. 190, p. 374–381, 2019. 32

DOMINGUES, M. O.; DEITERDING, R.; Moreira Lopes, M.; Fontes Gomes, A. K.; MENDES, O.; SCHNEIDER, K. Wavelet-based parallel dynamic mesh adaptation for magnetohydrodynamics in the amroc framework. **Computers and Fluids**, v. 190, p. 374–381, 2019. 32

DUNGEY, J. W. Interplanetary magnetic field and the auroral zones. **Physical Review Letters**, v. 6, 1961. 15

EASTMAN, T. E.; FRANK, L. A.; HUANG, C. Y. The boundary layers as the primary transport regions of the earth's magnetotail. **Journal of Geophysical Research**, v. 90, 1985. 10

FENG, X. **Magnetohydrodynamic modeling of the solar corona and heliosphere**. [S.l.: s.n.], 2019. 33, 35

FROMANG, S.; HENNEBELLE, P.; TEYSSIER, R. A high order godunov scheme with constrained transport and adaptive mesh refinement for astrophysical magnetohydrodynamics. **Astronomy and Astrophysics**, v. 457, n. 2, p. 371–384, 2006. 3

GLOCER, A.; FOK, M.; MENG, X.; TOTH, G.; BUZULUKOVA, N.; CHEN, S.; LIN, K. Crcm + bats-r-us two-way coupling. **Journal of Geophysical Research: Space Physics**, v. 118, 04 2013. 87

GONZALEZ, W. D.; JOSELYN, J. A.; KAMIDE, Y.; KROEHL, H. W.; ROSTOKER, G.; TSURUTANI, B. T.; VASYLIUNAS, V. M. What is a geomagnetic storm? **Journal of Geophysical Research: Space Physics**, v. 99, n. A4, p. 5771–5792, 1994. 56

Gonzalez, W. D.; Tsurutani, B. T.; Clúa de Gonzalez, A. L. Interplanetary origin of geomagnetic storms. **Journal of Geophysical Research: Space Physics**, v. 88, p. 529–562, apr. 1999. 60

GOODMAN, M. A three-dimensional, iterative mapping procedure for the implementation of an ionosphere-magnetosphere anisotropic ohm's law boundary condition in global magnetohydrodynamic simulations. **Annales Geophysicae**, v. 13, p. 843–853, 08 1995. 5, 76, 93, 96, 97, 98

HAJRA, R.; ECHER, E.; TSURUTANI, B. T.; GONZALEZ, W. D. Solar cycle dependence of high-intensity long-duration continuous ae activity (hildcaa) events, relativistic electron predictors? **Journal of Geophysical Research: Space Physics**, v. 118, n. 9, p. 5626–5638, 2013. 62

HARTEN, A. Adaptive multiresolution schemes for shock computations. **Journal of Computational Physics**, n. 115, p. 319–338, 1994. 3, 32

HOLLWEG, J. V. Some physical processes in the solar wind. **Reviews of Geophysics**, v. 16, n. 4, p. 689–720, 1978. 60

HOPKINS, P. F. A constrained-gradient method to control divergence errors in numerical mhd. **Monthly Notices of the Royal Astronomical Society**, v. 462, n. 1, p. 576–587, 2016. 33

HUNDHAUSEN., A. J. Coronal expansion and solar wind. **Journal of Fluid Mechanics**, v. 58, n. 4, p. 819–820, 1973. 59

IIJIMA, T.; POTEMRA, T. A.; ZANETTI, L. J.; BYTHROW, P. F. Large-scale Birkeland currents in the dayside polar region during strongly northward IMF: a new Birkeland current system. **Journal of Geophysical Research: Space Physics**, v. 89, n. A9, p. 7441–7452, 1984. 2

IIJIMA, T.; SHIBAJI, T. Global characteristics of northward imf-associated (nbz) field-aligned currents. **Journal of Geophysical Research: Space Physics**, v. 92, n. A3, p. 2408–2424, 1987. 3

KARNIADAKIS, G. E.; KIRBY, R. M. **Parallel scientific computing in C and MPI: a seamless approach to parallel algorithms and their implementation**. Cambridge: Cambridge University Press, 2003. 97

KENNEL, C. F. Shock structure in classical magnetohydrodynamics. **Journal of Geophysical Research**, v. 93, 1988. 9

KIVELSON, M. G.; RUSSELL, C. T. **Introduction to space physics**. Cambridge: Cambridge University Press, 1995. 588 p. 1, 2, 8, 10, 11, 12, 13, 14, 15, 16, 17, 19, 20, 21, 22, 23

LEBOEUF, J.; TAJIMA, T.; KENNEL, C.; DAWSON, J. Global simulation of the time-dependent magnetosphere. **Geophysical Research Letter**, v. 5, n. 7, p. 609–612, jul. 1978. 2

MAYAUD, P. N. **What is a geomagnetic index**. [S.l.]: American Geophysical Union (AGU), 1980. 2-4 p. 19

MCPHERRON, R.; MANKA, R. Dynamics of the 1054 ut march 22, 1979, substorm event - cdaw 6. **Journal of Geophysical Research Atmospheres**, v. 90, 1985. 22

MCPHERRON, R. L. Growth phase of magnetospheric substorms. **Journal of Geophysical Research**, v. 75, n. 28, p. 5592–5599, 1970. 20

MENDES, O.; ADHIKARI, B.; DOMINGUES, M. O.; ECHER, E.; TAKESHI, R. S. Interrelationships of similar magnetic effects at low and high latitudes during

high-intensity long-duration auroral activity events: case studies. **Brazilian Journal of Physics**, v. 52, p. 156–175, 2022. 62

MIYOSHI, T.; KUSANO, K. A multi-state hll approximate riemann solver for ideal magnetohydrodynamics. **Journal of Computational Physics**, v. 208, p. 315–344, sep. 2005. 33, 45, 52

MOEN, J.; BREKKE, A. The solar flux influence on quiet time conductances in the auroral ionosphere. **Geophysical Research Letters**, v. 20, n. 10, p. 971–974, 1993. 94

MOLDWIN, M. **An introduction to space weather**. [S.l.]: Cambridge University Press, 2008. 1-142 p. 7

Moreira Lopez, M. **Numerical methods applied to space magnetohydrodynamics for high performance computing**. 203 p. (INPE-10394-TDI/920). Thesis (Doctorate in Applied Computing) — Instituto Nacional de Pesquisas Espaciais (INPE), São José dos Campos, 2019. Available from: <http://urlib.net/8JMKD3MGP3W34R/3T3K8C2>. Access in: 2021. 29, 32, 33, 34, 35, 37, 44

MUNZ, C.-D.; OMNES, P.; SCHNEIDER, R.; SONNENDRüCKER, E. Divergence correction techniques for maxwell solvers based on a hyperbolic model. **Journal of Computational Physics**, v. 161, n. 2, p. 484–511, 2000. 33

NISHIDA, A. **Geomagnetic diagnosis of the magnetosphere**. United States: Springer-Verlag, 1978. 256 p. 56

OGINO, T. A three-dimensional mhd simulation of the interaction of the solar wind with the earth's magnetosphere - the generation of field-aligned currents. **Journal of Geophysical Research**, v. 91, p. 6791–6806, 1986. 37, 38, 39, 55, 68, 70, 98

OGINO, T.; WALKER, R.; ASHOUR-ABDALLA, M. A global magnetohydrodynamic simulation of the magnetosheath and magnetosphere when the interplanetary magnetic field is northward. **IEEE Transactions on Plasma Science**, v. 20, n. 6, p. 817–828, 1992. 2, 37, 40

PALACIOS, J.; GUERRERO, A.; CID, C.; SAIZ, E.; CERRATO, Y. Defining scale thresholds for geomagnetic storms through statistics. **Natural Hazards and Earth System Sciences Discussions**, v. 2018, p. 1–17, 2018. 105

PÉRON, S.; RENAUD, T.; BENOIT, C.; MARY, I. **Cartesian CFD methods for complex applications: ICIAM 2019 SEMA SIMAI Springer Series 3**. [S.l.: s.n.], 2021. 32

PETSCHECK, H. **Magnetic field annihilation**. [S.l.: s.n.], 1964. 425 p. 17

POTEMRA, T. A. **Birkeland currents: present understanding and some remaining questions**. Boston, MA: Springer US, 1983. 335–353 p. 26

POWELL, K.; ROE, P.; LINDE, T.; GOMBOSI, T.; ZEEUW, D. L. D. A solution-adaptive upwind scheme for ideal magnetohydrodynamics. **Journal of Computational Physics**, v. 154, p. 284–309, 1999. 33

RIDLEY, A. J.; GOMBOSI, T. I.; DEZEEUW, D. L. Ionospheric control of the magnetosphere: conductance. **Annales Geophysicae**, v. 22, n. 2, p. 567–584, 2004. 95

ROBINSON, R. M.; VONDRAK, R. R. Measurements of E region ionization and conductivity produced by solar illumination at high latitudes. **Journal of Geophysical Research: Space Physics**, v. 89, n. A6, p. 3951–3956, jun. 1984. 94

ROBINSON, R. M.; VONDRAK, R. R.; MILLER, K.; DABBS, T.; HARDY, D. On calculating ionospheric conductances from the flux and energy of precipitating electrons. **Journal of Geophysical Research: Space Physics**, v. 92, n. A3, p. 2565–2569, 1987. 94

ROSTOKER, G. Geomagnetic indices. **Reviews of Geophysics**, v. 10, n. 4, p. 935–950, 1972. 20

RUSSELL, C. T.; LUHMANN, J. G. **Earth magnetic field and magnetosphere**. [S.l.]: Springer Netherlands, 1997. 208-211 p. 12

SHEELEY, N. R.; HARVEY, J. W. Coronal holes, solar wind streams, and geomagnetic disturbances during 1978 and 1979. **Solar Physics**, v. 70, p. 237–249, 1981. 59

SHEELEY N. R., J.; HARVEY, J. W.; FELDMAN, W. C. Coronal holes, solar wind streams, and recurrent geomagnetic disturbances: 1973 1976. **Geophysical Research Letters**, v. 49, n. 2, p. 271–278, aug. 1976. 59

SMITH, E. J.; WOLFE, J. H. Observations of interaction regions and corotating shocks between one and five AU: pioneers 10 and 11. **Geophysical Research Letters**, v. 3, n. 3, p. 137–140, 1976. 59

SPIRO, R. W.; REIFF, P. H.; MAHER L. J., J. Precipitating electron energy flux and auroral zone conductances-an empirical model. **Journal of Geophysical Research: Space Physics**, v. 87, n. A10, p. 8215–8227, oct. 1982. 94

SPREITER, J. R.; SUMMERS, A. L.; ALKSNE, A. Y. Hydromagnetic flow around the magnetosphere. **Planetary and Space Science**, v. 14, n. 3, p. 223–253, 1966. 8, 9

STONE, J. M.; GARDINER, T. A.; TEUBEN, P.; HAWLEY, J. F.; SIMON, J. B. Athena: a new code for astrophysical MHD. **The Astrophysical Journal Supplement Series**, v. 178, n. 1, p. 137–177, sep 2008. 3, 86

TANAKA, T. Generation mechanisms for magnetosphere-ionosphere current systems deduced from a three-dimensional mhd simulation of the solar wind-magnetosphere-ionosphere coupling processes. **Journal Of Geophysical Research, Space Physics**, 1995. 3, 76, 93, 96, 99

TEYSSIER, R. Cosmological hydrodynamics with adaptive mesh refinement: a new high resolution code called ramses. **Astronomy and Astrophysics**, 2001. 85

TSURUTANI, B. T.; GONZALEZ, W. D. The cause of high-intensity long-duration continuous AE activity (HILDCAAs): interplanetary Alfvén wave trains. **Planetary and Space Science**, v. 35, n. 4, p. 405–412, 1987. 55, 56, 60, 62, 105

TSURUTANI, B. T.; GONZALEZ, W. D.; GONZALEZ, A. L. C.; TANG, F.; ARBALLO, J. K.; OKADA, M. Interplanetary origin of geomagnetic activity in the declining phase of the solar cycle. **Journal of Geophysical Research: Space Physics**, v. 100, n. A11, p. 21717–21733, 1995. 60

TóTH, G.; HOLST, B. van der; SOKOLOV, I.; ZEEUW, D.; GOMBOSI, T.; FANG, F.; MANCHESTER, W.; MENG, X.; NAJIB, D.; POWELL, K.; STOUT, Q.; GLOCER, A.; MA, Y.; OPHER, M. Adaptive numerical algorithms in space weather modeling. **Journal of Computational Physics**, v. 231, p. 870–903, 03 2012. 51

YAVNEH, I. Why multigrid methods are so efficient. **Computing in Science and Engineering**, v. 8, p. 12–22, 12 2006. 97

ZHANG, B.; SORATHIA, K. A.; LYON, J. G.; MERKIN, V. G.; GARRETSON, J. S.; WILTBERGER, M. GAMERA: A three-dimensional finite-volume MHD solver for non-orthogonal curvilinear geometries. **The Astrophysical Journal Supplement Series**, v. 244, p. 20, sep 2019. 88, 89

APPENDIX A - RELATED-MHD RESOURCES FOR SPACE APPLICATIONS

A.1 The RAMSES code

The RAMSES code, available in the webpage https://www.ics.uzh.ch/~teyssier/ramses/RAMSES.html, was introduced in Teyssier (2001) as an N-body and hydrodynamical code. This code, written in the Fortran 90 language, makes extensive use of the MPI library. Its original purpose is to apply high spatial resolution in the study of structure formations in the universe.

The hydrodynamical solver uses an Adaptive Mesh Refinement (AMR) technique to produce adaptive grids based on the tree-based data structure that allows recursive grid refinements. This approach differs from the AMROC framework by the refinement on a cell-by-cell basis, instead of the patch-by-patch refinement used in the AMROC.

In regards to numerical schemes, the RAMSES code uses a second-order Godunov method capable of capturing shocks and computing accurately the thermal history of the fluid component. For the MHD simulations, this code uses the Constrained Transport (CT) method to deal with the divergence in the magnetic field that arises during the simulation.

Main features

- Cartesian AMR grids in 1D, 2D or 3D.
- Solving the Poisson equation with a Multigrid and a Conjugate Gradient solver.
- Using various Riemann solvers (Lax-Friedrich, HLLC, exact) for adiabatic gas dynamic.
- Computing collisionless particles (dark matter and stars) dynamic using a PM code.
- Computing the cooling and heating of a metal-rich plasma due to atomic physics processes and a homogeneous UV background.
- Implementing a model of star formation based on a standard Schmidt law with the traditional set of parameters.

- Implementing a model of supernovae-driven winds based on local Sedov blast wave solution.

All these features can be used and parametrized using the RAMSES parameter file, based on the Fortran *namelist* format.

A.2 The ATHENA framework

The ATHENA framework introduced in Stone et al. (2008) and available in `https://princetonuniversity.github.io/Athena-Cversion/`, is designed to be extensible for the use of both static and adaptive mesh refinement. The static mesh refinement procedure differs by using an adaptive grid that is maintained unchanged during the entire simulation, which often leads to better performance due to avoiding grid adaptation routines. However, this approach may lose the formation of structures that arises from unrefined regions.

As the RAMSES code, the ATHENA framework combines higher-order Godunov methods with the CT technique to enforce the divergence-free constraint on the magnetic field.

Main features

ATHENA implements algorithms for the following physics:

- Compressible hydrodynamics and MHD in 1D, 2D, and 3D.
- Special relativistic hydrodynamics and MHD.
- Ideal gas equation of state with arbitrary γ.
- An arbitrary number of passive scalars advected with the flow.
- Self-gravity, and a static gravitational potential.
- Ohm resistivity, ambipolar diffusion, and the Hall effect.
- Both Navier-Stokes and anisotropic (Branginskii) viscosity.
- Both isotropic and anisotropic thermal conduction

In addition, ATHENA allows for the following grid parallelization options:

- Cartesian or cylindrical coordinates.
- Static (fixed) mesh refinement.
- Shearing-box source terms, and an orbital advection algorithm for MHD.
- Parallelization using domain decomposition and MPI. A variety of choices are also available for the numerical algorithms, such as different Riemann solvers and spatial reconstruction methods.

A.3 BATS-R-US code

The Block-Adaptive-Tree Solar-Wind Roe-Type Upwind Scheme (BATS-R-US) is a widely used code, implemented in the Fortran90 language with MPI libraries, developed by the former Computational Magnetohydrodynamics (MHD) Group at the University of Michigan (now Center for Space Environment Modeling (CSEM)). This code is considered a part of the Space Weather Modeling Framework (SWMF) (GLOCER et al., 2013), which integrates the physics of various regions between the Sun and Earth. Furthermore, it was designed to be executed on a massively parallel computer system.

Regarding numerical schemes, similarly to the AMROC, the BATS-R-US solves 3D MHD equations using the finite volumes method alongside with Roe type Approximate Riemann Solver. Furthermore, this code uses an adaptive grid composed of rectangular blocks arranged in varying degrees of spatial refinement levels.

The magnetospheric module of the BATS-R-US includes an ionospheric potential solver that provides electric potentials and conductances in the ionosphere from magnetospheric field-aligned currents in order to produce more physically consistent results due to the proper ionosphere-magnetosphere coupling.

However, contrary to the mentioned codes, the BATS-R-US is not freely available. Instead, it requires the potential users to send a simulation request, then collect the outputs without access to the source code.

Main features

BATS-R-US implements algorithms for the following physics:

- Classical, semi-relativistic, and Hall MHD.

- Multispecies, multifluid, anisotropic ion pressure.
- (Anisotropic) heat conduction, Alfvén wave turbulence.
- Radiation hydrodynamics with grey/multigroup diffusion
- Multimaterial, non-ideal equation of state.

In addition, BATS-R-US allows for the following numeric options:

- Conservative finite-volume discretization.
- Parallel block-adaptive grid.
- Cartesian and generalized coordinates.
- Splitting the magnetic field into $B_0 + B_1$.
- Divergence B control: 8 waves, CT, projection, parabolic/hyperbolic cleaning.
- Shock-capturing TVD schemes: Rusanov, HLLE, Roe, HLLD.
- Explicit, point-implicit, semi-implicit, fully implicit time stepping.

Applications

- Sun, Heliosphere, magnetosphere, unmagnetized planets, moons, comets.

Finally, this code has more than 100000 lines of Fortran90 with MPI parallelization.

A.4 GAMERA framework

The Grid Agnostic MHD for Extended Research Applications (GAMERA) code implements multidimensional MHD simulations in arbitrary non-orthogonal curvilinear geometries on modern supercomputer architectures. This allows the simulation of plasmas in various contexts involving the use of meshes that conform to the intrinsic geometry of the system under conservation. For that, this code combines geometry flexibility with high-order spatial reconstruction and the CT method to maintain the magnetic field without divergence components (ZHANG et al., 2019).

Among the numerical methodologies for reconstructions, the GAMERA code can perform accurate grid metric calculations using high-order Gaussian quadrature techniques, high-order upwind reconstruction, non-clipping options for interface values, and improved treatment of axis singularities. Furthermore, this code is designed to use data structures and memory access patterns conducive to aligned vector operations and the implementation of hybrid parallelism, using MPI (ZHANG et al., 2019).

Main features

- Applications for Magnetosphere-Ionosphere-thermosphere coupling, radiation belts, ring current, and inner heliosphere.
- Conservative and semi-conservative energy equation treatment (total and plasma energy formulations).
- Constrained transport (magnetic flux is defined at cell faces, while the electric field is defined at cell edges) keeps the magnetic field divergenceless to round-off error.
- This allows adapting the grid to the geometry of the problem (e.g., packing more grid cells around the magnetopause in magnetospheric calculations) and overall high resolving power with a relatively small total number of grid cells.
- For magnetospheric applications was rewritten the ionospheric solver was from a legacy code (Lyon Fedder Mobarry (LFM) code) and integrated the new FORTRAN code with GAMERA. The new solver incorporates the standard LFM ionospheric conductivity model, including ionization by solar irradiance and magnetospheric electron precipitation.

APPENDIX B - DISCRETIZATION OF THE IONOSPHERIC POTENTIAL

B.1 Derivative of the conductances

Derivatives of the conductances of the Equation C.11 produces the following result:

$$\begin{aligned}
\frac{\partial(\Sigma_{\phi\phi})}{\partial\phi} &= \frac{\Sigma_0\Sigma_P(8\Sigma_0\cos\phi\sin\phi - 2\Sigma_P\sin\phi\cos\phi - 6\Sigma_P\cos^3\phi\sin\phi - 6\Sigma_P\sin^3\phi\cos\phi)}{(4\Sigma_0\cos^2\phi + \Sigma_P\sin^2\phi)^2} \\
\frac{\partial(\Sigma_{\theta\phi})}{\partial\theta} &= 0 \\
\frac{\partial}{\partial\phi}\left(\frac{\Sigma_{\theta\phi}}{\sin\phi}\right) &= \\
\frac{(-8\Sigma_0^2\Sigma_H\sin^2\phi\cos^2\phi) + (8\Sigma_0^2\cos^4\phi\Sigma_H) + (24\Sigma_0^2\Sigma_H\cos^6\phi) + (12\Sigma_0\Sigma_H\Sigma_P\sin^4\phi\cos^2\phi) + (2\Sigma_0\Sigma_H\Sigma_P\sin^4\phi)}{(4\Sigma_0\cos^2\phi\sin\phi + \Sigma_P\sin^3\phi)^2\sqrt{1+3\cos^2\phi}} & \\
+\frac{(6\Sigma_0\Sigma_H\Sigma_P\sin^2\phi\cos^2\phi) + (18\Sigma_0\Sigma_P\Sigma_H\cos^4\phi\sin^2\phi)}{(4\Sigma_0\cos^2\phi\sin\phi + \Sigma_P\sin^3\phi)^2\sqrt{1+3\cos^2\phi}} & \\
\frac{\partial}{\partial\theta}(\Sigma_{\theta\theta}) &= 0
\end{aligned} \tag{B.1}$$

B.2 Finite difference method

Definition of the finite difference method for the second and first order partial differential equation.

$$\begin{aligned}
\frac{\partial^2\psi_{r,\theta,\phi}}{\partial\phi^2} &= \frac{\psi_{r,\theta,\phi+1} - 2\psi_{r,\theta,\phi} + \psi_{r,\theta,\phi-1}}{\triangle\phi} \\
\frac{\partial^2\psi_{r,\theta,\phi}}{\partial\theta^2} &= \frac{\psi_{r,\theta+1,\phi} - 2\psi_{r,\theta,\phi} + \psi_{r,\theta-1,\phi}}{\triangle\theta} \\
\frac{\partial\psi_{r,\theta,\phi}}{\partial\phi} &= \frac{\psi_{r,\theta,\phi+1} - \psi_{r,\theta,\phi-1}}{2\triangle\phi} \\
\frac{\partial\psi_{r,\theta,\phi}}{\partial\theta} &= \frac{\psi_{r,\theta+1,\phi} - \psi_{r,\theta-1,\phi}}{2\triangle\theta}
\end{aligned} \tag{B.2}$$

B.3 Discretization of the ionospheric potential using finite difference

Discretization of Equation C.11 using finite difference method.

$$\begin{aligned}\Bigg(&\frac{\Sigma_{\phi\phi}\psi_{r,\theta,\phi+1}}{\triangle\phi} - \frac{2\Sigma_{\phi\phi}\psi_{r,\theta,\phi}}{\triangle\phi} + \frac{\Sigma_{\phi\phi}\psi_{r,\theta,\phi-1}}{\triangle\phi} + \frac{\Sigma_{\theta\theta}}{\sin^2\phi}\frac{\psi_{r,\theta+1,\phi}}{\triangle\theta} - \frac{2\Sigma_{\theta\theta}}{\sin^2\phi}\frac{\psi_{r,\theta,\phi}}{\triangle\theta}\\ &+\frac{\Sigma_{\theta\theta}}{\sin^2\phi}\frac{\psi_{r,\theta-1,\phi}}{\triangle\theta} + \frac{\partial}{\partial\phi}\Sigma_{\phi\phi}\frac{\psi_{r,\theta,\phi+1}}{2\triangle\phi} - \frac{\partial}{\partial\phi}\Sigma_{\phi\phi}\frac{\psi_{r,\theta,\phi-1}}{2\triangle\phi} + \frac{\cos\phi}{\sin\phi}\Sigma_{\phi\phi}\frac{\psi_{r,\theta,\phi+1}}{2\triangle\phi}\\ &-\frac{\cos\phi}{\sin\phi}\Sigma_{\phi\phi}\frac{\psi_{r,\theta,\phi-1}}{2\triangle\phi}\frac{1}{\sin\phi}\frac{\partial\Sigma_{\theta\phi}}{\partial\theta}\frac{\psi_{r,\theta,\phi+1}}{2\triangle\phi} - \frac{1}{\sin\phi}\frac{\partial\Sigma_{\theta\phi}}{\partial\theta}\frac{\psi_{r,\theta,\phi-1}}{2\triangle\phi}\\ &-\frac{\partial}{\partial\phi}\frac{\Sigma_{\theta\phi}}{\sin\phi}\frac{\psi_{r,\theta+1,\phi}}{2\triangle\theta} + \frac{\partial}{\partial\phi}\frac{\Sigma_{\theta\phi}}{\sin\phi}\frac{\psi_{r,\theta-1,\phi}}{2\triangle\theta} + \frac{1}{\sin^2\phi}\frac{\partial}{\partial\theta}\Sigma_{\theta\theta}\frac{\psi_{r,\theta+1,\phi}}{2\triangle\theta}\\ &-\frac{1}{\sin^2\phi}\frac{\partial}{\partial\theta}\Sigma_{\theta\theta}\frac{\psi_{r,\theta-1,\phi}}{2\triangle\theta} - \frac{\Sigma_{\theta\phi}\cos\phi}{\sin^2\phi}\frac{\psi_{r,\theta+1,\phi}}{2\triangle\theta}\\ &+\frac{\Sigma_{\theta\phi}\cos\phi}{\sin^2\phi}\frac{\psi_{r,\theta-1,\phi}}{2\triangle\theta}\Bigg) = r_1^2 j_R\end{aligned} \tag{B.3}$$

To use the Red/Black Gauss-Seidel method, the fixed point iteration for the elliptic partial differential equation for three dimensions, using the r, θ, ϕ mapping, became:

$$\psi_{r,\theta,\phi} = \frac{r_1^2 j_R - ()}{\frac{-2\Sigma_{\phi\phi}}{\triangle\phi} - \frac{2\Sigma_{\theta\theta}}{\sin^2\phi\triangle\theta}} \tag{B.4}$$

where () is refers to the previous equation without $\psi_{r,\theta,\phi}$.

APPENDIX C - THE INTERNAL BOUNDARY

C.1 Derivative of the conductances

The implementation of an internal boundary inside the magnetosphere, which calls the Ionosphere. It consists of rebuilt plasma velocity through the computation of conductances, current densities, ionospheric potential, electric field, and magnetic field considering two boundaries as shown in Figure C.1, one of them the internal boundary at $r_1 = 1R_E$ refers to Ionosphere, and then another one the external boundary at $r_2 = 3.5R_E$, which refers to Plasmasphere where R_E is the radius of the Earth.

The Ionosphere proposed by Goodman (1995) was developed in spherical coordinates as an internal boundary of a previous magnetosphere defined by Tanaka (1995).

The usage of this implementation is working under the assumption that global MHD simulations of the Earth's magnetosphere must be coupled with a dynamical Ionosphere module in order to get a more realistic result.

Figure C.1 - Representation of the internal and external boundaries.

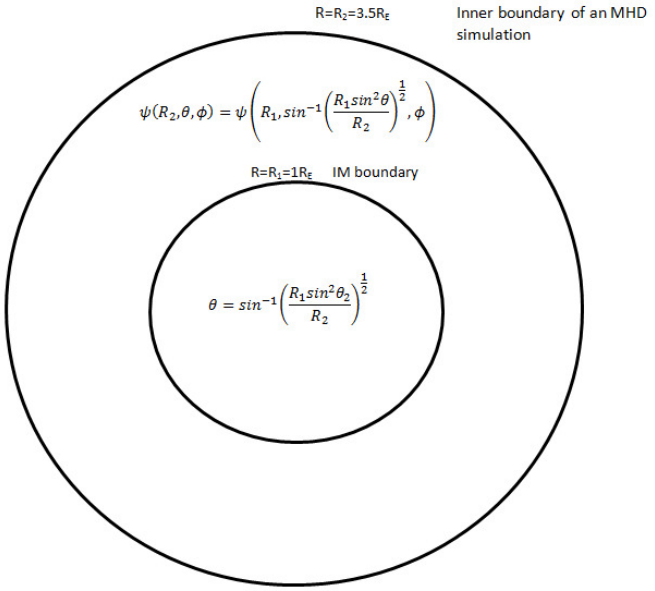

SOURCE: Author's production.

C.2 Implementation of the internal boundary

This section explains the contribution of solar radiation and electron precipitation to conductances considering empirical equations to get the matrix of conductances.

C.2.1 Contribution to the conductances from electron precipitation

To include conductances affected by electron precipitation in the ionosphere, global maps of conductances were developed by SPIRO et al. (1982), for this work was used equations define by Robinson et al. (1987), as follows:

$$\Sigma_P = \frac{40\,E_0}{16 + E_0^2}\,\sqrt{I_E} \tag{C.1}$$

$$\Sigma_H = 0.45\,E_0^{0.85}\,\Sigma_P \tag{C.2}$$

$$E_0 = \frac{\int_{E_{min}}^{E_{max}} E\;F(E)\;\mathrm{d}E}{\int_{E_{min}}^{E_{max}} F(E)\;\mathrm{d}E} \tag{C.3}$$

where the average electron energy E_0 is given in $\langle \mathrm{keV} \rangle$, the electron flux distribution function $F(E)$ is given in $\left\langle \mathrm{cm^{-2}s^{-1}keV^{-1}} \right\rangle$, and the electron energy flux I_E is given in $\langle \mathrm{ergs\,cm^{-2}s^{-1}} \rangle$. The minimum and maximum values of the energy distribution function are expressed by E_{min} and E_{max}.

On the nightside, where the solar flux is negligible and the conductivity is due to field-aligned electron precipitation, Robinson et al. (1987) proposed $4.9\,\langle \mathrm{keV} \rangle$ and $1.9\,\langle \mathrm{ergs\,cm^{-2}s^{-1}} \rangle$ for average electron energy and electron energy flux respectively, producing $\mathbf{6.8}\,\langle \mathrm{mhos} \rangle$ and $\mathbf{11.6}\,\langle \mathrm{mhos} \rangle$ for Pedersen and Hall conductances respectively. These conductances keep constant in each cell during the whole simulation.

C.2.2 Contribution to the conductances from solar radiation

To include conductances affected by solar radiation in the ionosphere, some empirical equations using radar measurements of electron profiles and standard models of the thermosphere were developed by ROBINSON and VONDRAK (1984), Moen and Brekke (1993), for this work used the empirical equation proposed by Moen and Brekke (1993), as follows:

$$\Sigma_P = S_a^{0.49}\left(0.34\cos(\chi) + 0.93\sqrt{\cos(\chi)}\right) \tag{C.4}$$

$$\Sigma_H = S_a^{0.53}\left(0.81\cos(\chi) + 0.54\sqrt{\cos(\chi)}\right) \tag{C.5}$$

where S_a is the solar radio flux index observed in 10.7cm and adjusted to 1 AU in $\left\langle 10^{-22}\mathrm{Wm}^{-2}\mathrm{Hz}^{-1}\right\rangle$ units; the angle χ is the solar zenith angle where $0 \leq \chi \leq \frac{\pi}{2}$.

On the dayside, electron precipitation and ionization due to solar radiation determine the Pedersen and Hall conductances. Also, the contribution from the Extreme Ultraviolet (EUV) and X-ray components of solar radiation may dominate the contributions from electrons. Besides that, and due to the variation of the zenith angle, these Pedersen and Hall conductances vary in each cell during the whole simulation.

The approximate variation of S_a[1] is from 60 at solar minimum to 240 at solar maximum, the collection of these values depends on the number of days of the dataset of the Sun that was being simulated.

C.2.3 Conductance matrix in spherical coordinates

In the previous section was computed Pedersen and Hall's conductances affected by electron precipitation and solar radiation, as a consequence, the final Pedersen and Hall conductances are the sum of these both contributions. In fact, these final conductances were put on a matrix which is called conductance matrix Amm and Goodman (1996), which was defined as follows:

$$\Sigma_{R,\theta,\phi} = \begin{pmatrix} 0 & 0 & 0 \\ 0 & \frac{\Sigma_0\Sigma_P}{C} & \frac{-\Sigma_0\Sigma_H\cos\epsilon}{C} \\ 0 & \frac{\Sigma_0\Sigma_H\cos\epsilon}{C} & \Sigma_P + \frac{\Sigma_H^2\sin^2\epsilon}{C} \end{pmatrix} \tag{C.6}$$

where $C = \Sigma_0\cos^2\epsilon + \Sigma_P\sin^2\epsilon$

$$\cos\epsilon = -\frac{2\cos\phi}{\sqrt{(1+3\cos^2\phi)^{\frac{1}{2}}}}, \quad \sin\epsilon = \frac{\sin\phi}{\sqrt{(1+3\cos^2\phi)^{\frac{1}{2}}}}, \tag{C.7}$$

where ϵ is the angle between the magnetic field B and the radial direction $\hat{R}$. Moreover, the parallel conductance was considered as 1000 mhos as mentioned in (RIDLEY et al., 2004).

Equation C.6 is valid for the northern and southern hemispheres (for $0 \leq \phi \leq \pi$). Each component of the conductance matrix was computed for each cell and was useful to compute the ionospheric potential.

[1]The values of S_a can be found at https://omniweb.gsfc.nasa.gov/form/dx1.html

C.3 Computation of the parallel current density

This section explained how to compute current density using the magnetic field which comes from the magnetosphere previously defined in this work.

From the primitive variables obtained in the magnetosphere proposed by Tanaka (1995), was consider the magnetic field to compute current density and use this variable in the ionosphere proposed by (GOODMAN, 1995). Thus, the equation is as follows:

$$J_{\parallel} = \nabla \times B \tag{C.8}$$

Equation C.8 is the parallel current density over the external boundary, this current serves as a condition to compute the parallel current density over the internal boundary as defined:

$$J_{\parallel}(r_1, \theta_1, \phi_1) = \left(\frac{r_2}{r_1}\right)^3 \sqrt{\left(\frac{1 + 3\cos^2\phi_1}{1 + 3\cos^2\phi_2}\right)} J_{\parallel}(r_2, \theta_2, \phi_2) \tag{C.9}$$

$$j_R = -\frac{2\, J_{||}(r_1, \theta_1, \phi_1)\ \cos\phi}{\sqrt{(1 + 3\,(\cos^2\phi)}} \tag{C.10}$$

Also, the parallel current density over the internal boundary served as a condition to compute the **source term** (J_R) which is useful to compute the ionospheric potential.

(GOODMAN, 1995) The magnetic field lines that cross the surface $r_2 = 3.5R_E$ are all continuous of field lines that cross $r_1 = 1R_E$ in the regions $\phi \leq 32.31°$ and $\pi - 32.31° \leq \phi \leq \pi$.

Under the fact mentioned before the computation of the source term and the ionospheric potential was done inside these areas, outside it the field lines are not continuous and have an unknown shape, as a consequence, the source term and the ionospheric potential are zero.

C.4 Computation of the ionospheric potential

This section used the Ionospheric potential proposed by Amm and Goodman (1996) that was computed under the assumptions that it varies slowly along the magnetic field lines and the parallel conductance is much greater than Pedersen and Hall conductances (GOODMAN, 1995).

$$\begin{aligned}
&\left[\frac{\Sigma_0\,\Sigma_p}{C}\right]\frac{\partial^2\psi}{\partial\phi^2} \\
&+\left[\frac{1}{(\sin\phi)^2}\left(\Sigma_p+\frac{(\Sigma_h\sin\epsilon)^2}{C}\right)\right]\frac{\partial^2\psi}{\partial\theta^2} \\
&+\left[\frac{\partial}{\partial\phi}\left(\frac{\Sigma_0\Sigma_p}{C}\right)+\cot\phi\frac{\Sigma_0\Sigma_p}{C}+\frac{1}{\sin\phi}\frac{\partial}{\partial\theta}\left(\frac{\Sigma_0\Sigma_h\cos\epsilon}{C}\right)\right]\frac{\partial\psi}{\partial\phi} \\
&-\left[\frac{\partial}{\partial\phi}\left(\frac{\Sigma_0\,\Sigma_h\,\cos(\epsilon)}{C\sin\phi}\right)-\frac{1}{(\sin\phi)^2}\frac{\partial}{\partial\theta}\left(\Sigma_p+\frac{(\Sigma_h\sin\epsilon)^2}{C}\right)+\frac{\Sigma_0\Sigma_h\cos\epsilon\cot\phi}{C\sin\phi}\right]\frac{\partial\psi}{\partial\theta} \\
&=r_1^2\,j_R
\end{aligned} \tag{C.11}$$

Equation C.11 is a linear and elliptic partial differential equation, so to get a solution to it, was develop a solver in AMROC based on Red/Black Gauss-Seidel method Karniadakis and Kirby (2003), Briggs et al. (2000) that was complete with the multigrid (MG) methods Yavneh (2006), Arrarás et al. (2015) in order to accelerate the convergence.

Equation C.11 shows the ionospheric potential over the internal boundary which contains four derivatives of conductances that are computed in Appendix B.1. After that, was used a finite difference method as mentioned in Appendix B.2 to discretize it which becomes in the equation shown in Appendix B.3. Finally, Equation C.11 has the structure to use it in the solver, as shown in Appendix B.4.

For the ionospheric potential over the external boundary was done an interpolation between these boundaries using the equation proposed by Goodman (1995), as follows:

$$\psi(r_2,\theta,\phi)=\psi\left(r_1,\theta,\arcsin\left(\frac{r_1\sin^2\phi_2}{r_2}\right)^{\frac{1}{2}}\right) \tag{C.12}$$

The ionospheric potential computed in Equation C.11 and Equation C.12 served as a condition to get the electric field over the external boundary.

C.5 Computation of the electric field

This section used the ionospheric potentials computed in Section C.4 to get the convection electric field proposed by Goodman (1995) over the external boundary.

$$\begin{aligned} E_r(r_2,\theta_2,\phi_2) &= \frac{\tan\phi_1}{2r_2}\frac{\partial\psi(r_1,\theta_1,\phi_1)}{\partial\phi_1} \\ E_\theta(r_2,\theta_2,\phi_2) &= -\frac{1}{r_2\sin\phi_2}\frac{\partial\psi(r_2,\theta_2,\phi_2)}{\partial\theta_2} \\ E_\phi(r_2,\theta_2,\phi_2) &= -\frac{1}{r_2}\frac{\partial\psi(r_2,\theta_2,\phi_2)}{\partial\phi_2} \end{aligned} \tag{C.13}$$

Equation C.13 serves as a condition to compute plasma velocity.

C.6 Computation of the plasma velocity

This section computed plasma velocity proposed by Goodman (1995) using the dipole magnetic field proposed by (OGINO, 1986).

$$\mathbf{V}_c(r_2,\theta_2,\phi_2) = \frac{C(\mathbf{E}_c\times\mathbf{B})}{B^2} \tag{C.14}$$

where C is the speed of light, E_c is the convection electric field and V_c is the plasma velocity due to convection electric field.

In general, the plasma velocity is affected by the convection Electric field and by the corotation Electric field due to the existence of plasma near the Earth. In this work was computed plasma velocity considering the sum of these both contributions.

So, the corotation electric field was defined by Baumjohann and Treumann (1996) as follows:

$$E_{cr} = B\times(\Omega_E\times r) \tag{C.15}$$

where E_{cr} is the corotation electric field and, $\Omega_E = 7.27.10^{-5}\frac{rad}{s}$ is the angular velocity of the Earth's rotation.

The plasma velocity considering corotation electric field was defined by Baumjohann and Treumann (1996) as follows:

$$V_{cr}(r_2,\theta_2,\phi_2) = \frac{E_{cr}\times B}{B^2} \tag{C.16}$$

where V_c is the plasma velocity due to the corotation electric field.

Finally, the plasma velocity is the sum of these both contributions.

$$V(r_2, \theta_2, \phi_2) = V_c + V_{cr} \tag{C.17}$$

The electric potential from the ionosphere affects plasma velocity in the magnetosphere, more specifically, affects velocity in the plasmasheet. To see these changes is necessary to update velocity in the primitive variables computed previously in the three-dimensional magnetosphere proposed by (TANAKA, 1995).

APPENDIX D - PROBE DATASET

D.1 Probe dataset

The AMROC-MHD is used to obtain the simulations concerning the conditions chosen for the studies. The outputs obtained for the events in this work are shown as follows. Figure D.1 and Figure D.2 show the complete dataset that the Probe 2D got from the bow shock during the simulation.

The left side of Figure D.1 shows four days of simulations for HILDCAA produced by ICME. The horizontal line at the beginning represents the running interval to reach the stationary condition for the Earth's magnetosphere. It is followed by a short interval corresponding to a linear interpolation from the initial magnetosphere (created for typical values) till the magnetosphere under the first actual input (close to Day Of Year - DOY - 133 and a half). In principle, the magnetosphere will spend approximately one day balancing the coupling process. Due to this reason, concerning the ICME event, the period for simulation analysis starts from DOY 135 (15 May 2005). Under a similar characterization, the right side of Figure D.1 shows six days of simulations for HILDCAA produced by CIR. During DOY 41, the coupling balance is reached. Concerning CIR, the period for simulation analysis starts from DOY 42 (11 February 2004).

In Figure D.2, the left side shows six days of simulations for the quiet period. During DOY 198, the coupling balance is reached. Concerning the Quiet time event, the period for simulation analysis starts from DOY 199 (18 July 2006). At last, the right side of Figure D.2 shows six days of simulations for HILDCAA not preceded by a storm (Non-storm event). During DOY 180, the coupling balance is reached. Concerning the Non-Storm event, the period for simulation analysis starts from DOY 181 (29 June 2012).

Figure D.1 - Probe 2D time series.

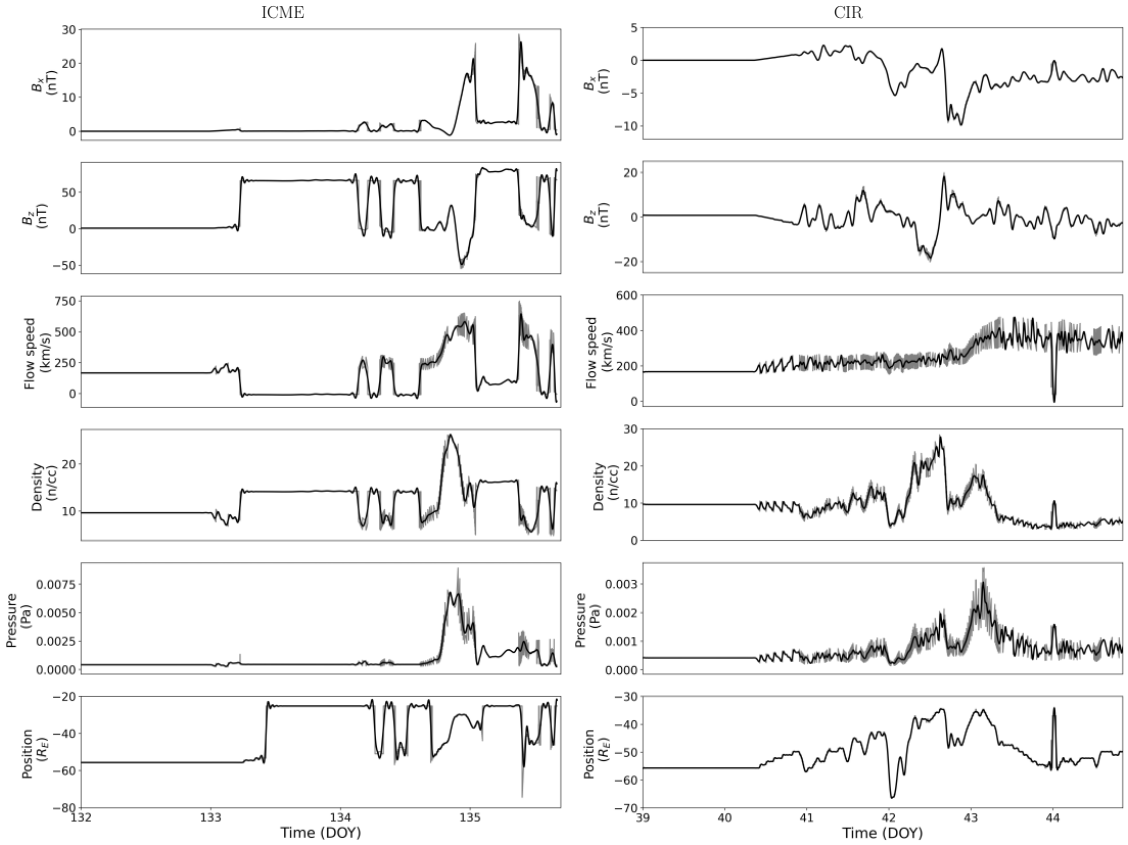

SOURCE: Author's production.

Figure D.2 - Probe 2D time series.

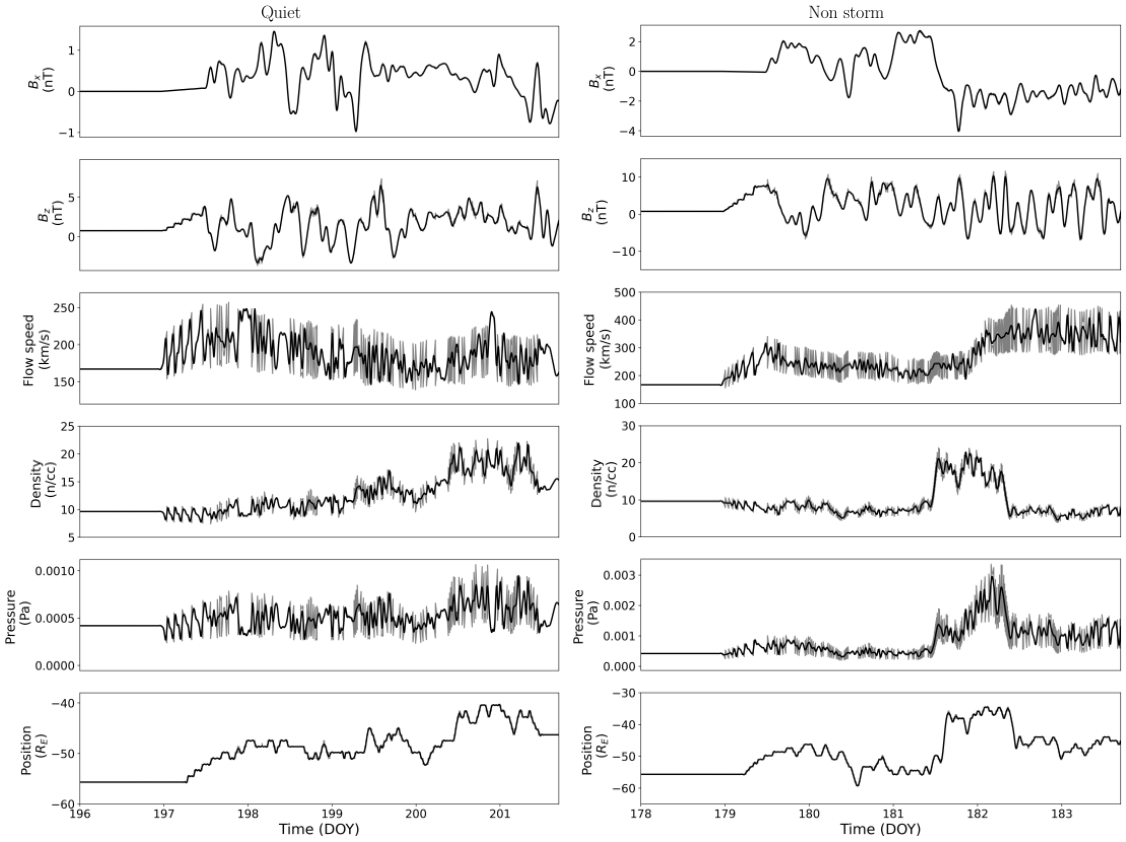

SOURCE: Author's production.

APPENDIX E - THE GEOMAGNETIC DISTURBANCE REGIMES

E.1 Geomagnetic disturbance regimes

High-Intensity Long Duration Continuous Auroral Activities, known as HILDCAAs, are phenomena associated with geomagnetic disturbances in the interior of the terrestrial environment. The criteria for their characterizations are supported by the geomagnetic auroral index AE, discussed in detail in Tsurutani and Gonzalez (1987).

To clarify the use of other significant disturbances on the terrestrial surface, the equatorial geomagnetic disturbance, which interferes with the definition of the HILDCAA interval, Table E.1 for regime characterization, including also the probable occurrence, is presented below, according to Palacios et al. (2018):

Regimes	**Dst**	**Frequency**
no geomagnetic disturbance	$Dst > -30$ nT	
weak geomagnetic regime	$-30 \geq Dst \geq -50$ nT	
moderate geomagnetic regime	$-50 > Dst \geq -100$ nT	every month
intense geomagnetic regime	$-100 > Dst \geq -300$ nT	several times per year
Super intense regime	$Dst < -300$ nT	few times in solar cycle

where **Dst** is the Disturbance storm time index.